Exploiting the SCF Complex to Identify Novel Therapeutic Targets in High-Grade Serous Ovarian Cancer

by

Ally C. Farrell

A Thesis submitted to the Faculty of Graduate Studies of
The University of Manitoba
in partial fulfillment of the requirements of the degree of

MASTER OF SCIENCE

Department of Biochemistry and Medical Genetics
University of Manitoba
Winnipeg

Copyright © 2023 by Ally Catherina Farrell

ABSTRACT

An overarching, yet elusive goal for cancer researchers is to develop novel therapeutic strategies by identifying drug targets that will improve the lives and outcomes of cancer patients. High-grade serous ovarian cancer (HGSOC) remains the most lethal gynecological malignancy, with an estimated ~3,100 Canadians diagnosed and ~1950 succumbing to their disease each year. Unfortunately, >70% of HGSOC patients are diagnosed at stages III or IV and will eventually succumb with drug resistant disease. Therefore, new, more effective drug targets are urgently needed to address the poor morbidity and mortality associated with HGSOC. Recent genetic studies have determined that reduced expression of *SKP1*, *CUL1* or *RBX1* induces chromosome instability (CIN), or ongoing changes in chromosome complements, that is suspected to contribute to HGSOC pathogenesis. As copy-number losses of these genes occur in ~87% HGSOCs, the current study seeks to exploit these alterations using a synthetic lethal (SL) paradigm. Synthetic lethality is an innovative therapeutic strategy and is defined as the rare/lethal combination of two independently viable mutations/deletions. Accordingly, identifying SL interactors of the SCF complex (*i.e.*, novel drug targets) would allow us to selectively exploit the aberrant genetics suspected to contribute to HGSOC pathogenesis.

To identify 228 putative SL interactors of *SKP1*, *CUL1* and *RBX1*, *in silico* and siRNA-based approaches were employed within FT secretory epithelial cellular contexts. Of these, *CDK2* and *PARP1* were prioritized for validation within $RBX1^{+/-}$ clones. To validate SL interactors, siRNAs and small-molecule inhibitors targeting *PARP1* or *CDK2* were combined with single-cell quantitative imaging microscopy (QuantIM) to assess SL phenotypes within $RBX1^{+/-}$ and NT-Control clones. QuantIM results reveal decreases in the number of $RBX1^{+/-}$ clones following silencing or inhibition of *PARP1* or *CDK2* relative to NT-Control clones, that corresponds with increases in γ-H2AX abundance, a marker of DNA DSBs. Collectively, the work presented in this thesis supports that *PARP1* is a novel SL interactor of *RBX1* and that *CDK2* is an evolutionarily conserved SL interactor of the SCF complex. Furthermore, these findings highlight the potential clinical utility of utilizing Olaparib and/or SNS-032 for the treatment of HGSOCs exhibiting diminished expression of *RBX1*.

ACKNOWLEDGEMENTS

To my supervisor, Dr. Kirk McManus, thank you for taking a chance and recognizing the potential of a very green, albeit very enthusiastic undergraduate student, and for continuously accepting my persistence to linger in the lab. Thank you for providing me with a space that fosters scientific curiosity and for allowing me the flexibility to explore my project in a manner that kept me motivated and energized, especially on days that science was uncooperative. Thank you for showing me that a healthy balance of professionalism, success and sarcasm is not only achievable, but maintainable and encouraged with the right people. Your steadfast mentorship and support have shaped me into the researcher and person that I am today, and for that I will always be incredibly grateful. Thank you to my committee member, Dr. Susan Logue, for the kind reminders that we can be passionate about our research, while remaining objective about the results during times of seemingly endless troubleshooting. Your words of encouragement and critical insights have helped me to consider the broader implications of my research and kept me inspired throughout my program. To Dr. Mark Nachtigal, thank you for being my committee member and "bonus supervisor" these past 4 years. Thank you for being my unsuspecting and inclusive conference guide and for always making time to lend an ear and encourage big ideas. Thank you for all the informative anecdotes and impromptu visits, and for showing me that everything I need to know I learned in grad school, in no small part to your continued support and reminders to take science (and life) one day at a time.

There are not enough words to appropriately express my gratitude to members of the McManus laboratory, past and present. Thank you, Claire Morden, for giving me such a warm and enthusiastic welcome into the lab. Your mentorship and friendship set the stage for what has become a life-changing experience for me and I'm so grateful that it began with you. To Mirka Sliwowski, thank you for sharing in my passion in patient-centered ovarian cancer research and for always taking the time to show me interesting samples and tissue culture techniques. Thank you, Dr. Lucile Jeusset, for your care and patience while training me as I developed the technical skills that I very much needed for my MSc Program. Thank you for the ice cream trips, board game nights, and for being a phenomenal mentor, friend, and recipe sharer. To Zelda Lichtensztejn, you are undoubtedly the "lab mom" that I didn't know I needed. Thank you for taking such care with each of us, for putting out any/all metaphorical fires with a smile, and for being such an inclusive and consistent support to me both inside and outside the lab.

To Chloe Lepage, thank you for filling the first several months of my MSc program with so much laughter and for sharing in my contempt over the DDR screen. Your help was instrumental in getting my project off of the ground and I am so grateful to have had so much fun while doing it, especially on the days we were eating dinner in the lab at midnight. To Rubi Campos Gudiño, thank you for sharing in all the milestones of our MSc program. Our communal sense of dread has really helped keep me going through courses and thesis writing, and I am happy to have gone through this alongside you. To Tyler Anderson, thank you for teaching (ahem, forcing) me to go with the flow and for all the Wednesday coffee meetings. Thank you for making work a fun place to be and for the much needed reminders to not take life so seriously. To Lukas Lam, thank you for working so incredibly hard to help me get this project over the finish line these last two summers. Your impressive sarcasm, fresh ideas and continued tolerance of my antics are always incredibly appreciated. To Nicole Neudorf and Kailee Rutherford, thank you for being the Bubbles and Blossom to my Buttercup and for always being up for a spontaneous wine or movie night. Your friendship is one that I am incredibly thankful for, especially on the days that science made us want to collectively scream into the void. Thank you for keeping me laughing even on days I didn't want to and for being far more supportive than "colleagues" ever need to be. I am so proud to have worked alongside you and I know you'll both accomplish great things as you move beyond this steppingstone that we have all been reluctant to leave. To Michaela Schellenberg, thank you for being so welcoming and for not (outwardly) hesitating at all when I told you I was going to be your new neighbour. Thank you for late night study dates, single-item grocery runs and for your effortless ability to make the mundane things feel less mundane. My life is a million times better with you in it.

To my family outside of the lab, chosen or otherwise, thank you for being a soft place to land and for reminding me that there is life outside of graduate studies. Your love and support have kept me afloat on days where my sanity was merely an idea. Finally, this research would not have been possible without the financial support of Research Manitoba, CancerCare Manitoba Foundation, Ovarian Cancer Canada, and the University of Manitoba. I would also like to thank the generous donors who provided funding for the Caroline A. Cope Award for Oncology Research and the Mindel Rady Olenick Fellowship in Human Genetics.

TABLE OF CONTENTS

LIST OF TABLES

LIST OF FIGURES

LIST OF ABBREVIATIONS

>	Greater than
≥	Greater than or equal to
<	Less than
%	Percent
~	Approximately
2D	Two-dimensional
3D	Three-dimensional
aa	Amino acid
AJCC	American Joint Committee on Cancer
ATM	Ataxia-telangiectasia mutated
BRAF	B-Raf
BRCA1/2	Breast cancer 1/2
CA125	Cancer Antigen 125
Cas9	CRISPR associated protein 9
CCNE1	Cyclin E1
CDK	Cyclin dependant kinase
CDK1	Cyclin dependant kinase 1
CDK2	Cyclin dependant kinase 2
CDK4	Cyclin dependant kinase 4
CDK7	Cyclin dependant kinase 7
CDK9	Cyclin dependant kinase 9
^{o}C	Degrees Celsius
CHEK2	Checkpoint kinase 2
CIN	Chromosome instability
cm	Centimeter(s) (size)
CNAs	Copy number alterations
CRISPR	Clustered regularly interspaced short palindromic repeats
CTD1	Chromatin licensing and DNA replication factor 1
C-terminal	Carboxy-terminal
CUL1	Cullin 1
CUL1$^{+/-}$	Heterozygous *CUL1* knockout
CUL3	Cullin 3
CUL4A/B	Cullin 4A/4B
CUL5	Cullin 5
CUL7	Cullin 7
DAPI	4',6-Diamidino-2-Phenylindole
DDB2	Damage Specific DNA Binding Protein 2
DDR	DNA damage repair
DMEM	Dulbecco's modified Eagle medium
DMSO	Dimethyl sulfoxide

DNA	Deoxyribonucleic acid
Drosophila melanogaster	D. melanogaster
E1	Ubiquitin-activating enzyme
E2	Ubiquitin-conjugating enzyme
E3	Ubiquitin ligase
EDTA	Ethylenediaminetetraacetic acid
EOC	Epithelial ovarian cancer
FANCD2	Fanconi anemia group D2 protein
FANCI	FA Complementation Group I
FDA	Food and Drug Administration
FIGO	Federation of Gynecology and Obstetrics
FT	Fallopian tube
g	gram(s)
HER2	Human epidermal growth factor receptor 2
HGSOC	High-grade serous ovarian cancer
HRP	Horseradish peroxidase
HRR	Homologous recombination repair
IRIF	Irradiation Induced Foci
K	Potassium
kDa	Kilodalton(s)
KEAP1	Kelch Like ECH Associated Protein 1
KRAS	Kirsten Rat Sarcoma Viral Proto-Oncogene
KS	Kolmogorov-Smirnov
min	minute(s)
mL	millilitre
mRNA	messenger RNA
NAD+	Nicotinamide adenine dinucleotide
n	Number of technical replicates
N	Number of experimental replicates
N-CIN	Numerical CIN
NER	Nucleotide excision repair
NHEJ	Nonhomologous end joining
NRF2	Nuclear factor erythroid 2-related factor 2
NRG	OD-Rag1null IL2rgnull
N-terminal	Amino-terminal
shRNA	short-hairpin RNA
PALB2	Partner and Localizer of BRCA2
PBS	Phosphate buffered saline
PAR	Poly(ADP-Ribose)
PARP1	Poly(ADP-Ribose) Polymerase 1
PARG	Poly(ADP-Ribose) Glycohydrolase
PLK1	Polo-like kinase 1

PTEN	Phosphatase and tensin homolog
P-value	Probability value
RAD51C	RAD51 Paralog C
RAD54B	RAD54 Homolog B
RIPA	Radioimmunoprecipitation assay
Rb	Retinoblastoma protein
R	Arginine
RBX1	RING box protein 1
$RBX1^{+/-}$	Heterozygous RBX1 knockout
RBX2	RING box protein 2
RT	Room temperature
S. cerevisiae	Saccromyces cerevisiae
SCF	SKP1-CUL1-FBOX
S-CIN	Structural CIN
SFM	Serum-free media
siRNA	Short-interfering RNA
SKP1	S-phase kinase-associated protein 1
$SKP1^{+/-}$	Heterozygous SKP1 knockout
SL	Synthetic lethal
SOD1	Superoxide dismutase type 1
S-phase	Synthesis Phase
SSB	Single-stand break(s)
STICs	Serous tubal intraepithelial carcinomas
SV40-Tag	Simian Vacuolating Virus 40 TAg
TCGA	The Cancer Genome Atlas
TERT	Telomerase reverse transcriptase
TP53	Tumor Protein P53
µg	Microgram(s) (weight)
µL	Microliter(s) (volume)
µm	Micron(s) (size)
µM	Micromolar (concentration)
UV	Ultraviolet
V	Volts
VEGF	Vascular endothelial growth factor
W	Tryptophan
XPC	Xeroderma Pigmentosum Group C Protein
γ-H2AX	Histone variant H2AX - Ser139

USED WITH PERMISSION AND CONTRIBUTION OF AUTHOR

PREFACE

This thesis contains material, images, and/or ideas from one article published in the peer-reviewed *International Journal of Molecular Sciences*, of which Ally C. Farrell was co-first author. This journal applies the Creative Commons Attribution (CC BY) license to articles and other works, such that articles can be reused in whole or in part for any purpose.

CONTRIBUTION OF AUTHOR

CHAPTER 1:

Campos Gudino, R., **Farrell, A.C.**, Neudorf, N.M. & McManus, K.J. A Comprehensive Assessment of Genetic and Epigenetic Alterations Identifies Frequent Variations Impacting Six Prototypic SCF Complex Members. *IJMS.* **84**, (2022).

Contribution: Ally C. Farrell contributed to original draft preparation (30%), editing (30%), and figure preparation (33%).

CHAPTER 1. INTRODUCTION

1.1 OVARIAN CANCER OVERVIEW

Cancer is the leading cause of death in Canada, and it is estimated that 1 in 2 Canadians will develop cancer in their lifetime, where half of all patients (*i.e.*, 1 in 4 Canadians) are predicted to eventually succumb to their disease[1]. Ovarian cancer is the 8th most common cancer in females, accounting for ~2.8% of all cancer diagnoses (~3,100 Canadians) and is predicted that 1 in 75 women will develop the disease in their lifetime[1]. Strikingly, ovarian cancer is the 5th leading cause of death in women, accounting for ~5% of all cancer-related deaths annually (~1950 Canadians)[1]. Epithelial ovarian cancer (EOC) accounts for the vast majority of ovarian cancer diagnoses (~90%) and encompasses a heterogeneous array of diseases, each associated with distinct genetic characteristics and prognoses[2]. High-grade serous ovarian cancer (HGSOC) is the most commonly diagnosed and lethal histotype of EOC, where patients are often diagnosed at late stages (III or IV) and chemotherapy is typically employed to treat residual disease following cytoreductive surgery[3,4]. Unfortunately, standard-of-care chemotherapeutics are associated with off-target effects, and despite responding to initial chemotherapy treatments, many HGSOC patients experience tumor recurrence and succumb to drug resistant disease[5,6]. As such, identifying novel drug targets for precision medicine strategies is key to improving HGSOC patient lives and outcomes. The current study explores how the aberrant genetics suspected to contribute to HGSOC pathogenesis can be therapeutically targeted using a synthetic lethal paradigm.

1.1.1 Epithelial Ovarian Cancer (EOC) Overview

There are five major histotypes of EOC, including high-grade serous, low-grade serous, endometrioid, clear cell and mucinous carcinomas, each associated with various incidence rates, biological characteristics and survival outcomes. As described above, HGSOC is the most common histotype, accounting for ~70% of all EOC diagnoses, whereas low-grade serous, endometrioid, clear cell and mucinous carcinomas are less common, accounting for ~6%, ~10%, ~10% and ~4% of EOCs, respectively[7,8]. Each histotype is further characterized by tumor "Type" based on their biological characteristics and disease pathogenesis. In general, Type I tumors retain wild-type *Tumor Protein P53* (*TP53*), present at early stages, are slow-growing, and harbour mutations in key genes such as *B-Raf* (*BRAF*) and *Kirsten Rat Sarcoma Viral Proto-Oncogene* (*KRAS*), including clear cell, mucinous, low-grade endometrioid and low-grade serous

carcinomas[2,9]. Type II tumors include undifferentiated carcinomas and HGSOCs[10], which are genetically unstable, characterized by a wide range of copy number alterations (CNAs) and genetic mutations, and are typically diagnosed at stage III or IV[4,9,11].

Initially, the ovarian surface epithelium was proposed as the cell of origin and primary site of EOC pathogenesis[11], however, research studies now suggest that the ovarian surface epithelium is more likely to be a secondary site in disease pathogenesis[7]. Indeed, more recent clinical evidence shows that EOC precursor cells vary by histotype and likely originate from other non-ovarian tissue types. For example, clear cell and endometrioid carcinomas are suspected to arise from displaced endometrial tissue, whereas mucinous carcinomas are suspected to originate within the tubal-peritoneal junction[2,7,12]. In a different manner, high-grade and low-grade serous carcinomas likely arise from the secretory epithelial cells within the distal fallopian tube (FT) mucosa (discussed further in ***Section 1.1.2***)[2,9,13,14].

Cancer stage at diagnosis also varies by EOC histotype and can greatly impact treatment options and survival outcomes. For example, ~58-64% of clear cell, mucinous and endometrioid carcinomas are diagnosed at stage I, with associated 5-year survival rates of ~71%, ~66%, and ~82%, respectively[10]. In contrast, >80% HGSOCs are diagnosed at stage III (51% of cases) or IV (29% of cases), with associated 5-year survival rates of ~42% and ~26%, respectively[10]. While the reduced survival rates associated with HGSOC can be somewhat accounted for by the large number of late-stage diagnoses, the eventual acquisition of multi-drug resistance by >70% of patients also contributes significantly to the high morbidity and mortality rates associated with the disease[6]. Accordingly, identifying new and improved therapeutic strategies are required to better combat HGSOC.

1.1.2 Risk Factors and Etiology of High-Grade Serous Ovarian Cancer (HGSOC)

The average lifetime risk of ovarian cancer is ~1.3%, although it is well-established that the acquisition of germline and/or somatic alterations in key genes can significantly increase an individual's predisposition to develop cancer[1]. Genomic characterization of HGSOC patient samples through genetic studies such as The Cancer Genome Atlas (TCGA) have revealed extensive somatic gene CNAs that are suspected to contribute to disease pathogenesis[15,16]. For example, genomic alterations such as *Cyclin E1* (*CCNE1*) amplification occurs in ~20% of HGSOCs and is suspected to contribute to HGSOC pathogenesis by promoting cell cycle-progression and genomic instability[15-17]. In addition, somatic defects in DNA homologous

recombination (HRR) genes occur in ~50% of HGSOCs[15,18,19], and can largely be accounted for by mutations in *Breast Cancer Type 1 Susceptibility Protein* (*BRCA1*; ~12%) or *Breast Cancer Type 2 Susceptibility Protein* (*BRCA2*; ~11%), although alterations within other HRR genes (*e.g.*, *Ataxia Telangiectasia Mutated* [*ATM*], *RAD51 Paralog C* [*RAD51C*], *Phosphatase And Tensin Homolog* [*PTEN*] and *Partner And Localizer Of BRCA2* [*PALB2*]) also occur[15]. Germline mutations can also dramatically increase an individual's risk of developing ovarian cancer. In HGSOC, germline mutations in *BRCA1* or *BRCA2* occur in ~13-17% of cases[15,20], conferring lifetime risks of hereditary ovarian cancer as high as ~54% and ~23%, respectively[21]. As a result, many individuals identified as carriers will elect to undergo risk-reducing, prophylactic surgical removal of both FTs and ovaries (*i.e.*, bi-lateral salpingo-oophorectomy)[22]. Interestingly, prophylactic collection of these biological samples has helped elucidate many of the mechanisms underlying HGSOC initiation and development, including the discovery that FT secretory epithelial cells are a likely precursor cell for HGSOC (***Figure 1-1***)[23]. The FTs are comprised of four major tissue layers, including the serosa, muscularis, submucosa, and mucosa[3,11]. The inner epithelium of the mucosal layer is comprised of both ciliated and secretory cells, where the latter is the proposed site and cell of origin for HGSOC initiation[2,11].

As described above, HGSOCs typically exhibit a myriad of low-frequency genetic alterations, with the exception of *TP53*, which harbours nonsense or missense mutations in virtually ~100% of HGSOCs[24-26]. Importantly, *TP53* mutations are suspected to be one of the earliest events in HGSOC pathogenesis and can be detected within FT precursor lesions using immunohistochemistry[14,27], referred to as a "TP53 signature"[13,23,28]. It has been determined that over time, "TP53 signatures" can progress into dysplastic precursor lesions at the FT fimbriae, termed serous tubal intraepithelial carcinomas (STICs)[2,3]. As the mean age of HGSOC diagnosis is ~64 years of age[10], it is thought that progression from a STIC lesion to an ovarian carcinoma may take years or even decades and is followed by rapid metastatic spread upon the acquisition of genetic alterations in additional key genes[2,9,11]. While STICs are not present in all HGSOC patients, many STICs harbour the same *TP53* mutations and copy-number alterations as their matched primary tumors, providing further evidence for the FT secretory epithelial cell as a precursor cell for HGSOC[14,27]. In contrast, the "precursor escape model" has been proposed as an alternative means of disease pathogenesis that may partially explain why STICs are not observed in all HGSOCs, despite the premise that they should be reported at similar incidence rates[29].

Briefly, the precursor escape model suggests that HGSOCs may develop from cells that shed from precursor lesions to the ovary or peritoneal cavity, rather than the commonly accepted STIC to ovarian carcinoma pathway, also known as the "dualistic model"[29]. However, the precursor escape model is still somewhat controversial, and additional research is required before the etiological events underlying HGSOC are entirely understood.

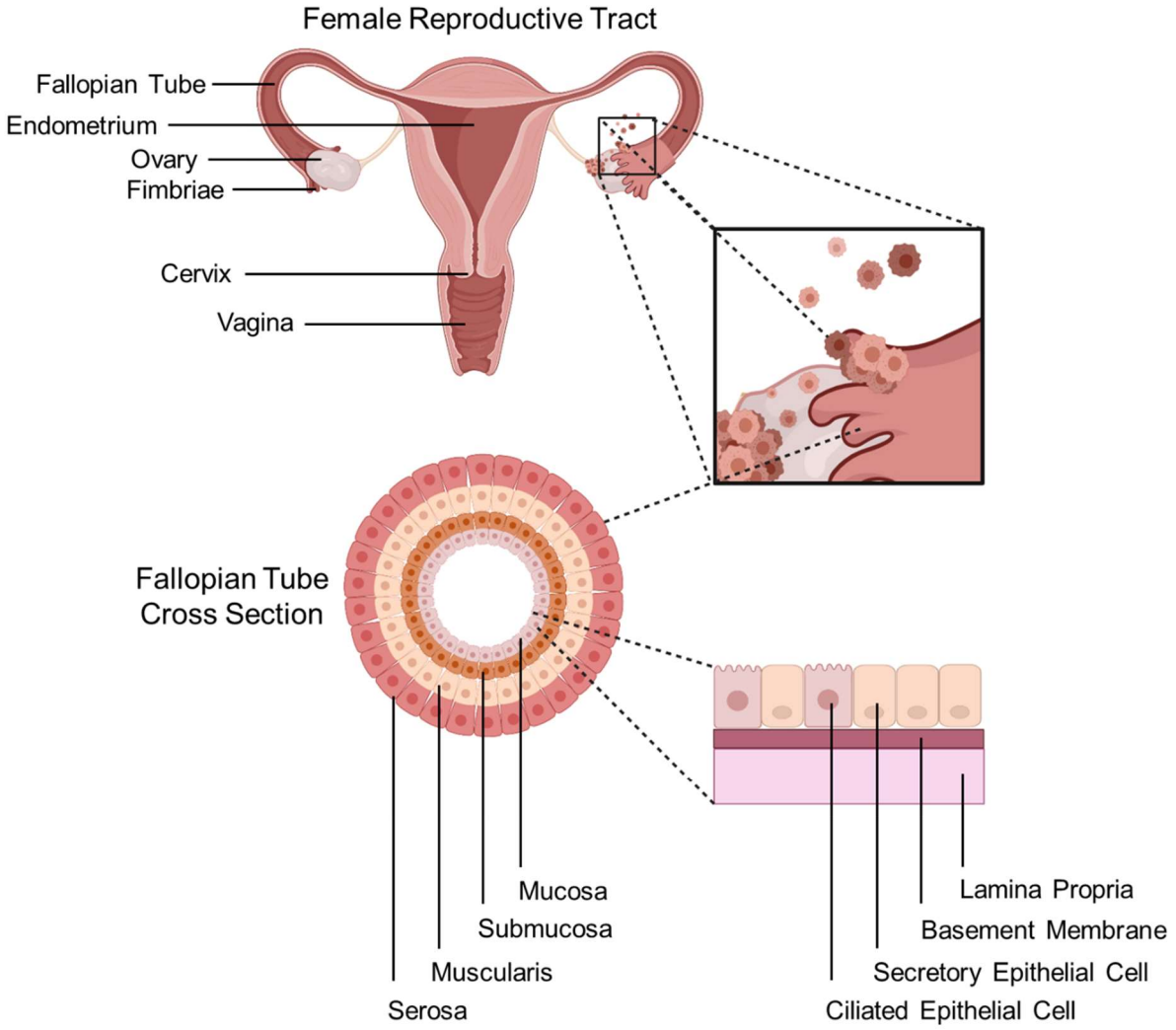

Figure 1-1. FT Secretory Epithelial Cells are a Precursor Cell of HGSOC.
Schematic depicting the organs, tissues, and cells involved in HGSOC development. According to the dualistic model[29], HGSOCs originate from dysplastic precursor lesions from the FT fimbriae, which can spread to nearby ovarian surface epithelium to form an ovarian tumor. A cross-sectional view of the FT displays the four major tissue layers, including the innermost mucosal layer comprised of secretory and ciliated epithelial cells, where it is the secretory epithelial cells that are a proposed cell of origin for HGSOC.

1.1.3 HGSOC Detection and Diagnosis

Accurate cancer detection and diagnosis is critical to patient well-being, as it guides treatment options and can offer valuable prognostic information[30]. In this regard, identifying cancers at early stages (I and II) is frequently associated with better treatment options and outcomes than cancers identified at later stages (III and IV)[9]. Unfortunately, there are currently no early detection methods available for HGSOC, and as a result, >80% of patients are diagnosed after the cancer has metastasized to other tissues[9,11]. Numerous clinical studies have sought to develop various screening modalities for HGSOC, including transvaginal ultrasounds and blood tests (*e.g.*, Cancer Antigen 125 [CA125])[9,31]. In an ovarian cancer context, transvaginal ultrasounds can be used to detect malignant lesions and ascites (*i.e.*, abdominal fluid build-up), whereas CA125 is a glycoprotein and serum marker that can be assessed at diagnosis but is primarily employed to predict disease progression and recurrance[32-34]. While these procedures can provide some insight into disease pathogenesis, they lack specificity and are largely employed to monitor individuals with increased risks of developing ovarian cancer, such as those harbouring germline *BRCA1/2* mutations[34]. As such, clinical research aimed at identifying reliable early-detection methods for HGSOC remains ongoing. For example, a study by Cohen *et al.*[35] assessed the specificity of a multi-analyte blood test that examines the prevalence of key mutations and proteins within circulating tumor deoxyribonucleic acid (DNA), aimed at detecting early-stage disease in a variety of cancer types, including ovarian cancer. They found that the "CancerSEEK" blood test was able to detect ovarian cancer with a sensitivity of ~78%, as well as provide insight into the location of the primary tumor with an accuracy of ~91%[35]. However, a major limitation of this study was the admitted inclusion of patients exhibiting symptoms that are associated with metastatic disease, despite not having been diagnosed with metastatic disease at the time of study entry, which may overestimate their ability to detect stage I cancers[35]. Therefore, additional research is required to determine the true clinical utility of early-detection methods such as these.

Prior to diagnosis, many HGSOC patients present with non-specific symptoms such as fatigue, pelvic and/or abdominal pain, bloating, nausea, constipation and acid reflux[5,30]. As such, HGSOC diagnosis, staging and grading is typically made during surgery. Tumor staging describes disease progression and is based on the 2014 International Federation of Gynecology and Obstetrics[36] (FIGO) or the American Joint Committee on Cancer[37] (AJCC), whereas tumor

grading provides valuable insight into disease malignancy and is based on cellular criteria including the number of cells in mitosis (*i.e.*, mitotic index) and nuclear pleomorphism scores (*i.e.*, irregular nuclear shape/size)[3,5,30]. In stage I HGSOC, the disease is confined to the FTs or ovaries, whereas stage II involves spread to other pelvic organs (*e.g.*, uterus, bladder)[5,7,38]. By stage III, the disease has spread to additional organs/tissues within the peritoneal cavity, or to the para-aortic or pelvic lymph nodes, while stage IV HGSOC typically describes metastasis beyond the peritoneal cavity, such as the extra-abdominal lymph nodes, lungs, spleen, or bone[5,7,38]. As described above, ~87% of HGSOC patients are diagnosed at stage III or IV, and typically only receive chemotherapy due to the challenges associated with identifying and surgically resecting all metastatic lesions[1,5] (detailed further in ***Section 1.1.4***). Of these patients, >70% will eventually experience disease recurrence and develop clinical resistance to their chemotherapy treatments[5,39] further highlighting the need for improved therapeutic strategies.

1.1.4 Clinical Management of HGSOC

When a patient is diagnosed with HGSOC, an assigned healthcare team will determine an appropriate treatment plan based on the patient's specific needs. Patients will typically undergo an initial cytoreductive, or debulking surgery[39], where the tumors that are removed can be assessed by a pathologist to confirm the disease diagnosis, stage and grade (detailed in Section ***1.1.3***)[30,39]. Debulking surgery is used to remove all macroscopic tumor masses within the peritoneal cavity[5], which may include a total hysterectomy (*i.e.*, removal of uterus), a bilateral salpingo-oophorectomy, and in some cases, the removal of the pelvic and abdominal lymph nodes[5,19,30,39]. In general, cytoreductive surgery is considered to be successful when there are no remaining macroscopic lesions[5] as these patients tend to have a lower risk of disease reccurence[30,39]. However, most HGSOC patients present with metastatic disease[5,11], which results in reduced operative success and limits the intended therapeutic impact of cytoreductive surgery[2,5]. As a result, these patients will typically undergo chemotherapeutic regimes to treat metastatic sites and combat residual disease[4,30,39].

The standard-of-care first-line chemotherapy regime for HGSOC patients is intravenous and/or intraperitoneal administration of paclitaxel and carboplatin[30,39]. Paclitaxel is a taxane agent that targets tubulin, whose mechanism of action involves hyper-stabilizing the microtubule structure to prevent its disassembly, leading to cell-cycle arrest in metaphase[40] (*i.e.*, it is a cell-cycle specific agent). This results in the prolonged activation of mitotic checkpoints, and

ultimately leads to cell death via apoptosis[40]. In a different manner, carboplatin is a platinum and alkylating agent that exerts its effects by cross-linking guanine bases at the N7 position in DNA[40]. Carboplatin can be employed to target both dividing and non-dividing cells and interferes with DNA transcription and replication by forming DNA intra- and inter-stand breaks, respectively[40]. In a cancer context, this leads to an accumulation of DNA damage, inducing a reduction in cell proliferation and/or cell death via apoptosis when DNA repair is not possible[40]. Unfortunately, paclitaxel and carboplatin lack specificity (*e.g.*, target rapidly dividing cells) and thus, are associated with numerous short- and long-term side effects[40]. Following chemotherapy treatments, HGSOC patients are at risk of developing an array of adverse effects ranging from hair loss, fatigue and nausea/vomiting to more severe long-term health issues including cognitive impairment, peripheral neuropathy and increased risk of secondary cancers[40-42].

If HGSOC patients are responsive to first-line treatments, maintenance therapies such as Bevacizumab[30] (Vascular endothelial growth factor [VEGF; angiogenesis inhibitor]) and/or Olaparib[39,43] (PARP1 [DNA repair] inhibitor; detailed further in ***Section 1.4.2***) may be administered with the objective of preventing disease recurrence[43]. However, despite many patients initially responding to first-line chemotherapeutic treatments, ~75% will relapse within 18 months[44], and are deemed resistant if relapse occurs within 6 months of treatment[4]. Should this occur, second-line chemotherapeutic agents such as topotecan (DNA topoisomerase inhibitor)[45], gemcitabine (nucleoside analog)[46], or pegylated liposomal doxorubicin (DNA intercalating agent)[47] may be prescribed in an attempt to prolong survival, though they are seldom curative[4]. As a result, alternative treatment strategies (*e.g.*, immune-based therapies) are currently being explored for the treatment of HGSOC patients. For example, immune-checkpoint inhibitors, such as pembrolizumab or nivolumab, aim to harness the body's natural immune response by inhibiting immune check-point proteins, which in turn facilitates immune cell recognition and attack on cancer cells that may have otherwise gone undetected[48]. However, additional preclinical studies are required to validate these findings, as the reported efficacy of these inhibitors varies for the treatment of HGSOC and are reportedly most effective when administered to cancer patients exhibiting certain biomarkers (*e.g.*, microsatellite instability)[48-50]. Given the extensive genetic heterogeneity associated with HGSOC, additional studies aimed at identifying alternative therapeutic strategies that exploit the inherent genetic instability to improve survival rates and quality of life for HGSOC patients is imperative.

1.2 CHROMOSOME INSTABILITY (CIN) IN CANCER

Genome instability is a characteristic of virtually all cancer types, characterized by increased mutations, CNAs and epigenetic changes[51,52]. Genome instability exhibits critical roles in disease initiation, progression, and drug resistance, and is classically categorized into at least three subtypes: 1) microsatellite instability; 2) CpG island methylator phenotype; and 3) chromosome instability (CIN)[51]. Microsatellite instability is characterized by a prevalence of defects in DNA mismatch repair genes, and as the name suggests, underlies the incorporation of DNA mismatches in addition to expansions and/or contractions of highly repetitive DNA sequences (*i.e.*, microsatellites)[53]. Contrastingly, CpG island methylator phenotype induces transcriptional silencing that occurs via extensive DNA methylation at CpG dinucleotides within gene promoters[52], whereas CIN is defined as an increased rate at which whole chromosomes or large parts thereof are gained or lost[6,17,54-60]. CIN drastically impairs genome stability by inducing ongoing changes in chromosome complements, and by extension, continuous CNAs in genes that are implicated in cancer pathogenesis[51,55-57,61,62]. Despite these associations, the molecular determinants (*i.e.*, aberrant genes, proteins and biological pathways) underlying CIN remain largely unknown. By expanding our understanding of the aberrant molecular events driving CIN, we hope to apply these findings to develop innovative treatment strategies to ultimately improve the lives and outcomes of patients diagnosed with HGSOC.

1.2.1 CIN in Cancer Pathogenesis

CIN is an enabling hallmark of cancer[52], defined as an increase in the rate at which whole chromosomes or large chromosomal fragments thereof are gained or lost[6,51,55-58,63]. Of the two types of CIN that occur, numerical CIN (N-CIN) is characterized by gains/losses of whole chromosomes, whereas structural CIN (S-CIN) is characterized by chromosomal rearrangements (*e.g.*, inversions and translocations)[62,64]. While both subtypes can occur independently, they are not mutually exclusive (*i.e.*, they can co-occur), leading to the emergence of dynamic and complex karyotypes that promote cancer evolution by increasing inter- and intratumoral heterogeneity and conferring novel survival capabilities[65,66]. In this regard, CIN is predicted to confer survival advantages to cells under certain selective pressures (*e.g.*, chemotherapy treatments), where those with a particular growth advantage (*e.g.*, drug resistance) may develop into an aggressive and/or drug-resistant tumor[67]. It is also important to note that CIN is an ongoing phenotype (*i.e.*, a rate, rather than a biological state), and is therefore suspected to

contribute to cancer pathogenesis by increasing the frequency at which key genes, such as tumor-suppressor genes, oncogenes and DNA repair genes, are gained, lost or altered[56-58]. Therefore, it is perhaps unsurprising that in many cancer types, tumors exhibiting high levels of CIN harbour genetic alterations that promote metastasis, disease recurrence and drug resistance[64,67,68], key features associated with HGSOC[5,11].

1.2.2 CIN in HGSOC

It is worth noting that while CIN is associated with the development and progression of both hematologic and solid cancers[52,62,63,65,66,68,69], its impact on HGSOC pathogenesis is only beginning to be elucidated. To address this, one biochemical study assessed the pervasiveness of CIN within tumor cells isolated from the ascites of HGSOC patients[70]. They determined that CIN is prevalent within these samples and that increases in CIN were generally associated with the acquisition of clinical resistance, highlighting its potential clinical utility as a prognostic biomarker. To expand beyond these findings, Morden *at al*.[6] characterized the prevalence of CIN in both tumor cells isolated from ascites and solid tumor samples and determined that CIN is prevalent and dynamic within ~95% of HGSOCs, with higher levels of CIN occurring in solid tumor cells relative to those from matched ascites[6]. They reasoned that these biological differences may be due to disease progression and/or treatment response and are reflective of the genetic and cell-to-cell heterogeneity that is typical of HGSOC patients[6]. In a different manner, research efforts aimed at identifying novel CIN genes (*i.e.*, genes whose aberrant expression induces CIN) and investigating their potential implication in early disease development are ongoing[55-58]. For example, the Nachtigal and McManus laboratories have identified key members of the S-phase Kinase associated Protein 1 (SKP1), Cullin 1 (CUL1), F-box protein (SCF) complex (See ***Section 1.3***) as novel CIN genes in multiple cancer contexts, including HGSOC[55-58]. Although the role of CIN in HGSOC pathogenesis has yet to be fully elucidated[2,5], identifying and characterizing the molecular determinants of CIN remains of great clinical importance as they may one day be used to guide treatment decisions and/or be exploited through the development of precision medicine strategies.

1.3 THE SCF COMPLEX

The ubiquitin-proteasome system represents a major mechanism in the regulation of protein abundance, where polyubiquitin chains are covalently attached to protein substrates through lysine 48 (K48) - glycine 76 (G76) isopeptide bonds via the activities of the E1 (ubiquitin activating), E2 (ubiquitin conjugating), and E3 (ubiquitin ligase) enzymes[17,59]. The transfer of ubiquitin and subsequent polyubiquitination of target substrates requires recognition and binding by the E3 ligase enzyme[71,72], and as such it is the E3 ligase that is largely responsible for conferring substrate specificity and proteasomal degradation via the 26S proteosome[73]. The SCF complex is a quaternary E3 ubiquitin ligase complex that is comprised of three invariable core subunits, SKP1, CUL1 and RING box protein 1 (RBX1), and 1 of 69 variable F-box proteins that confers substrate specificity (***Figure 1-2***)[17,56-60,72]. Importantly, the SCF complex comprises the largest group of E3 ubiquitin ligases[17] that encompasses a diverse array substrate specificities including cell cycle regulators (Cyclin E1)[55-57,74], transcription factors (N-Myc)[75] and regulators of DNA damage-response (DDR; RAD51)[76].

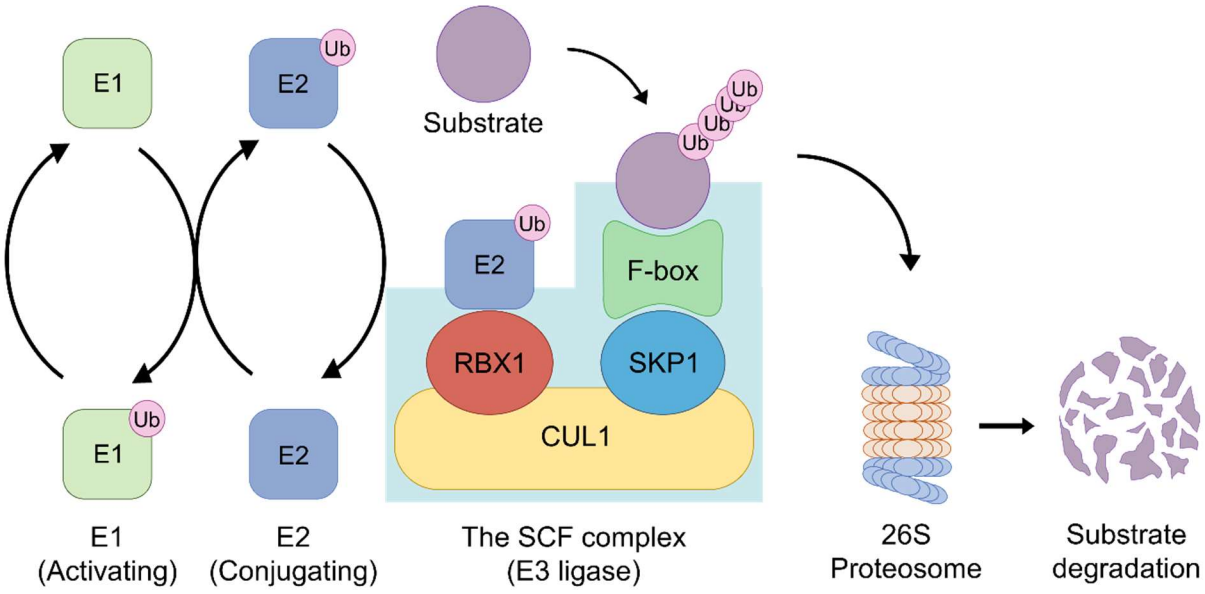

Figure 1-2. The SCF Complex and the Ubiquitin-Proteosome System.
Schematic illustrating E1 (an activating enzyme) and E2 (a conjugating enzyme) cycling of ubiquitin (Ub). E1/E2 cycling is followed by SCF complex-mediated poly-ubiquitination and subsequent proteasomal degradation of a substrate. The SCF complex is a quaternary structure comprised of three invariable core members (SKP1; CUL1; RBX1) and one of 69 variable F-box proteins that confer substrate specificity.

1.3.1 SKP1

Human *SKP1* maps to chromosome 5q31.1 and is comprised of five exons spanning ~28 kb of genomic DNA[77]. It encodes two distinct protein isoforms of 160 and 163 amino acids (aa), both with a mass of ~18 kilodaltons (kDa)[77]. Notably, the larger (163 aa) isoform has been established as the most functionally relevant as it includes a tryptophan residue (W159) that is indispensable for its *in vivo* activity[78]. SKP1 contains two protein domains, including a Carboxy terminal (C-terminal) Cullin-binding domain and an F-box protein binding domain[17]. In the context of the SCF complex, SKP1 is one of three invariable core members of the complex that serves an adapter protein that links one of 69 F-box proteins to CUL1[17,79]. Importantly, recent genetic studies have identified *SKP1* as a *bona fide* human CIN gene by showing that diminished expression of *SKP1* induces CIN and CIN-associated phenotypes (*e.g.*, changes in nuclear area, micronucleus formation) within HGSOC and colorectal cancer contexts that is suspected to contribute to disease pathogenesis[55,57].

1.3.2 CUL1

Human *CUL1* maps to 7q36.1, is comprised of 22 exons spanning ~103 kb of genomic DNA and encodes a single protein of 776 aa with a corresponding molecular mass of ~90 kDa[77]. Cullin proteins contain three major domains, including a variable amino terminal (N-terminal) region that interacts with an adapter protein to function as substrate binding site, a C-terminal cullin-homology domain that interacts with its respective RING finger protein (*i.e.*, where E2 enzyme binding occurs) and a neddylation domain[80]. Briefly, and to facilitate ubiquitin transfer, Cullin proteins (*e.g.*, Cullins 1, 2, 3, 4a, 4b, 5, 7, and 9) must be activated via post-translational modification by a small ubiquitin like molecule called NEDD8 (*i.e.*, neddylation)[81,82]. CUL1 is best characterized of the Cullin proteins and is a core component of the SCF complex, with SKP1 serving as its adapter protein and RBX1 as its associated RING finger protein[72]. As with *SKP1*, recent studies have determined that *CUL1* knock-down induces karyotypic heterogeneity, changes in nuclear area and micronucleus formation (*i.e.*, a hallmark of CIN) in HGSOC precursor cells, identifying *CUL1* as a novel CIN gene that is suspected to contribute to HGSOC development and progression[57].

1.3.3 RBX1

Human *RBX1* maps to 22q13.2 and is comprised of 5 exons, spanning ~11 kb of genomic DNA and encodes a protein of 108 aa with a corresponding molecular mass of ~12 kDa[83]. RBX1 contains an N-terminal domain for interaction with CUL1 (*i.e.*, scaffold binding site) in addition to a C-terminal RING-H2 zinc finger domain required for its ligase activity[84,85]. As the name suggests, the RING-H2 subunit contains histidine and cysteine residues to facilitate the coordination of two zinc ions to form a unique 'cross-brace' motif[17]. Within the SCF complex, RBX1 catalyzes the neddylation of CUL1[17,56,57,59], which stabilizes the interaction between CUL1 and the E2 enzyme[86] to catalyze the ubiquitination of protein substrate[17,56]. Interestingly, RBX1 can also form additional E3 ligases, including the KEAP1-CUL3-RBX1 E3 ligase[87], and can therefore polyubiquitinate proteins independent of the SCF complex[88,89]. For example, the KEAP1-CUL3-RBX1 E3 ligase plays an important role in HRR via the ubiquitination of PALB2[90]. In HRR, PALB2 serves an adaptor within a complex comprised of BRCA1, BRCA2 and RAD51 to facilitate DNA double-strand break (DSB) repair, where the ubiquitination of PALB2 is essential for complex formation[91,92]. As such, altered expression and function of *RBX1* may adversely impact essential biological processes such as DNA repair and genome stability. Indeed, *RBX1* has been identified a novel CIN gene in ovarian cancer contexts[56]. More specifically, decreased expression of *RBX1* induces increases in CIN and Cyclin E1 abundance, as well as promotes cellular transformation by enabling anchorage-independent growth and is therefore suspected to be an early event in HGSOC pathogenesis[56].

1.3.4 The SCF Complex is Frequently Altered in Cancers

Established SCF complex targets include transcription factors (*e.g.*, C-Myc), oncoproteins (*e.g.*, β-catenin) and tumor suppressors (*e.g.*, BRCA2) that modulate cell cycle activity and mitotic fidelity[17,55-60,72,93-95]. Accordingly, genetic alterations involving SCF complex member genes are expected to adversely impact target regulation and contribute to cancer development. In 2021, Campos Gudiño *et al.*[17] sought to assess the prevalence of genetic and epigenetic alterations of six prototypic SCF complex member genes, including *SKP1*, *CUL1* and *RBX1*, using patient data extracted from TCGA[15]. They determined that ~45% of observed missense mutations were predicted to adversely impact SCF complex structure and/or function and that the distribution of encoded alterations support the possibility that SCF complex member genes may exhibit tumor suppressor or oncogenic mutational profiles in a cancer type dependent

manner[17]. They also noted that the SCF complex genes exhibit frequent CNAs that correlate with significant changes in mRNA expression levels. For example, genes exhibiting copy number losses (*e.g.*, heterozygous loss) correlated with reduced mRNA expression relative to those with diploid copy numbers[17]. Importantly, *SKP1*, *CUL1* and *RBX1* harbour shallow deletions (*i.e.*, heterozygous loss) in ~42%, ~11%, ~81% of ovarian cancers, respectively[15,17,96] and are therefore of tremendous clinical interest (***Figure 1-3***). As copy number losses underlying their reduced expression induces CIN that is suspected to lead to the accumulation of oncoproteins, like Cyclin E1[55-57], they are suspected to be key pathogenic driver events in the development and progression of many cancer types[55-59,97], including HGSOC[56,57]. Accordingly, copy number losses of these genes may represent genetically exploitable targets, further highlighting their potential clinical relevance for the development of synthetic genetic strategies to develop new precision medicine approaches.

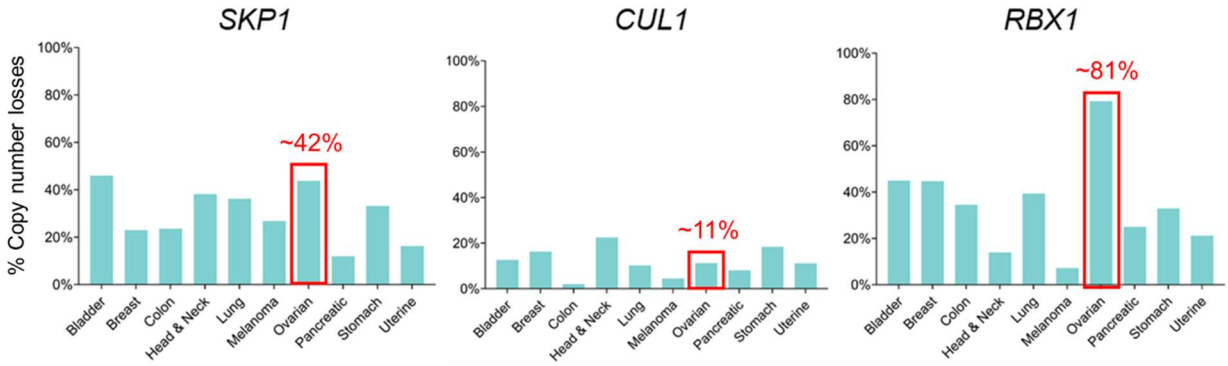

Figure 1-3. Core SCF Complex Members Exhbit Frequent Copy Number Losses in Cancer. Bar-graphs depicting the frequency of gene copy number losses (shallow deletions/heterozygous loss) of the core SCF complex members in 10 common cancer types. Frequencies of ovarian cancer patient samples are highlighted with a red bounding box.

1.4 SYNTHETIC GENETIC TARGETING IS A PROMISING THERAPEUTIC STRATEGY

Many standard-of-care chemotherapeutics (*e.g.*, platinum agents) are non-specific and target rapidly dividing cells, leading to a wide range of unwanted side effects[40]. To address this, therapeutic strategies with increased specificity are urgently needed to better combat HGSOC and improve patient quality of life. Synthetic genetic approaches aim to selectively target and kill cancer cells by exploiting the aberrant genetics (mutations, deletions and amplifications) suspected to underlie cancer development, while minimizing the off-target effects typically associated with common chemotherapeutic strategies. As such, synthetic genetic interactions,

including synthetic lethality and synthetic dosage lethality, are being explored for their therapeutic potential and clinical applicability in various cancer contexts[98-102]. Briefly, synthetic lethality exploits hypomorphic expression and/or function of tumor suppressor genes, whereas synthetic dosage lethality exploits hypermorphic expression and/or function associated with oncogenes[54,103]. While this thesis is focused primarily on synthetic lethality as a precision medicine strategy, both of these paradigms are detailed below.

1.4.1 Synthetic Lethality

In 1922, Calvin Bridges described genetic interactions analogous to synthetic lethality following manipulations of chromosome complements of fruit flies[104]. However, the term "synthetic lethality" was not actually coined until 1946, when it was used to describe a lethal recombination event between two independently viable homologous chromosomes in *Drosophila pseudoobscura* by the geneticist Theodosius Dobzhansky[105]. Synthetic lethality is now defined as the lethal combination of two independently viable mutations/deletions, where the genes involved are referred to as synthetic lethal (SL) interactors (***Figure 1-4***)[54]. Much of what is known about synthetic lethality has been uncovered using model organisms such as *Saccharomyces cerevisiae*, as they are highly amenable to high-throughput genetic approaches[106]. Indeed, cross-species research studies have revealed that SL interactions are rare in nature, occurring only between a small subset of gene pairs[107-109]. Large-scale mapping of SL gene pairs in model organisms have also helped identify the principal mechanisms underlying SL phenotypes[54,105], which typically occur via one of three biological pathways. For example, a lethal phenotype may occur following the ablation of two proteins contained within the same essential biological pathway/epistasis group, such that the pathway becomes non-functional[54]. Another mechanism through which synthetic lethality can occur is following the ablation of two proteins contained within essential parallel pathways, as seen with the prototypic SL interaction between *BRCA1/2* and *PARP1* (detailed further in ***Section 1.4.2***)[110,111]. Lastly, the ablation of two proteins within parallel pathways, such as HRR and non-homologous end joining (NHEJ), that together impinge on an essential biological pathway, namely DNA double-strand break repair, can also induce lethality[54].

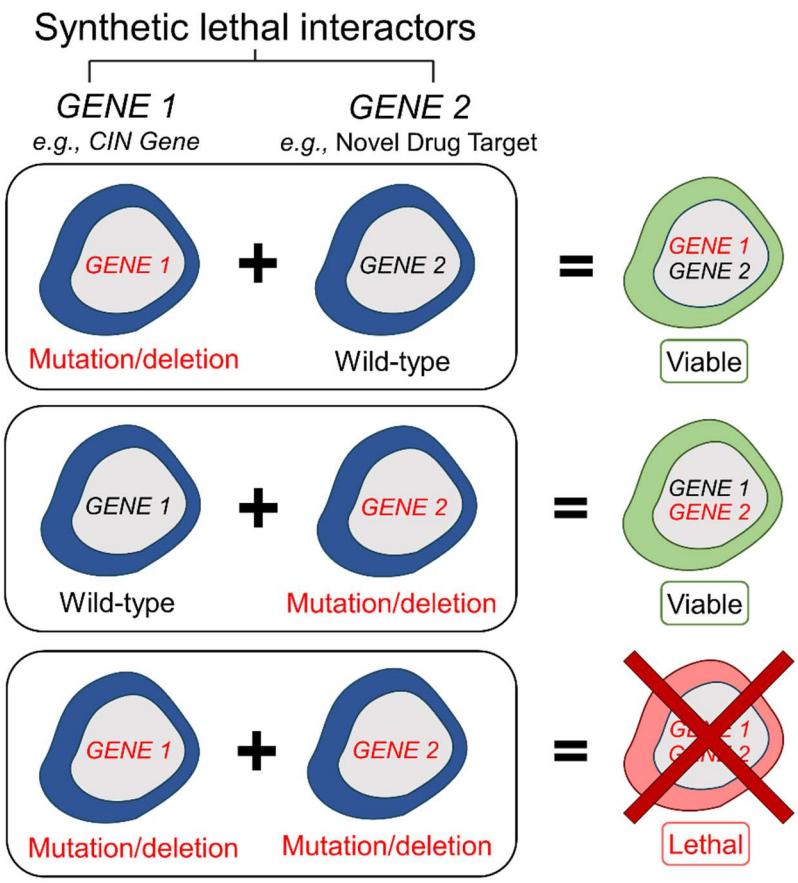

Figure 1-4. The SL Paradigm.
Schematic illustrating the SL paradigm, where synthetic lethality is defined as a rare and lethal combination of two independently viable mutations/deletions (*GENE 1* or *GENE 2*) that result in death when combined.

As stated above, synthetic lethality is an attractive therapeutic approach as it can selectively target cancer cells exhibiting diminished and/or hypomorphic expression of key genes that are frequently altered in cancer (*e.g.*, tumor suppressor genes)[103,106,112]. This deviates from the "traditional" pipeline of targeting increased and/or hypermorphic expression of oncogenes by enabling the therapeutic targeting of genetic alterations that were previously classified as "undruggable", while minimizing the off-target effects typically associated with many chemotherapeutic agents[54,69,106]. Consequently, synthetic lethality can be leveraged to better combat disease and has since been successfully translated into the clinic for the treatment of HGSOC and other cancer types[39,69,101,103,112].

1.4.2 Synthetic Lethality in the Clinic

An overarching, yet elusive goal for cancer researchers is to develop novel therapeutic strategies by identifying drug targets that can selectively target and kill cancer cells harbouring defects in genes suspected to contribute to cancer development (*e.g.*, CIN genes). It was Hartwell and colleagues[113] who originally posited that cancer cells harboring somatic mutations may be therapeutically targeted by using SL strategies[114,115]. Nearly 20 years later, the ground breaking identification of a SL interaction between *BRCA1* or *BRCA2* and *PARP1*[110,111] began the translation of synthetic lethality into the clinic[110,111]. PARP1 is a critical member of various DNA repair pathways, including single-strand break (SSB) repair, and functions by sensing DNA damage and recruiting other DDR repair proteins to the damaged site[43,110,116]. In the case of PARP1 deletion or inhibition, DNA damage leads to an accumulation of SSBs and DSBs, requiring DNA repair via HRR pathway[110,116]. As BRCA1 and BRCA2 have central roles in HRR, it was theorized that therapeutic targeting of PARP1 could be utilized to induce lethality within *BRCA1*- or *BRCA2*-deficient cells, which was later confirmed by functional biological studies[43,110]. Further clinical investigation ultimately led to the Food and Drug Administration (FDA) approval of the PARP1 inhibitor Olaparib (Lynparza) for patients with advanced stage ovarian cancer harbouring germline mutations in either *BRCA1* or *BRCA2* in 2014, and it is now employed as a maintenance therapy for all HGSOC patients[43]. Notably, PARP inhibitors are now employed to treat a variety of other tumor types harbouring germline or somatic mutations in either *BRCA1* or *BRCA2*, including prostate, breast and pancreatic cancers[43,101,112,117], further highlighting the broad therapeutic potential and clinical applicability associated with synthetic lethality as a precision medicine strategy.

1.4.3 Synthetic Dosage Lethality

Similar to synthetic lethality, synthetic dosage lethality has long been studied in model organisms and represents a promising precision medicine strategy. The term “synthetic dosage lethality” was established in 1996, following a study that determined that increasing the abundance or activity of a protein could induce lethality in a genetically sensitized strain of yeast[118]. Conceptually, the amplification of oncogenes contributes to cancer pathogenesis via hypermorphic expression and/or function of its encoded protein and is therefore an attractive target for cancer therapies. For example, *MYCN*, also known as *N-Myc*, encodes a transcription factor involved in regulating cell cycle progression, cell proliferation and apoptosis. In a cancer

context, *MYCN* amplification occurs in a variety of tumor types[96,119], and is associated with increased tumorigenicity and reduced overall survival[120,121]. Despite these unfortunate associations, oncogene amplifications can also serve as a means of distinguishing tumor cells from normal surrounding tissues, where the gain-of-function alterations can be therapeutically exploited by employing a synthetic dosage lethal strategy (***Figure 1-5***). One genetic study identified *Cyclin-dependant kinase 2* (*CDK2*) as a synthetic dosage lethal interactor (drug target) of *MYCN*, after *CDK2* knockdown successfully induced apoptosis in *MYCN*-amplified neuroblastoma cells[122]. They also noted that *MYCN* silencing rescues this phenotype, highlighting that *MYCN* amplification is essential to induce lethality[122]. Accordingly, the search for novel candidate drug targets aimed at exploiting gain-of-function alterations remains an active area of research in hopes of improving treatment options and cancer patient outcomes.

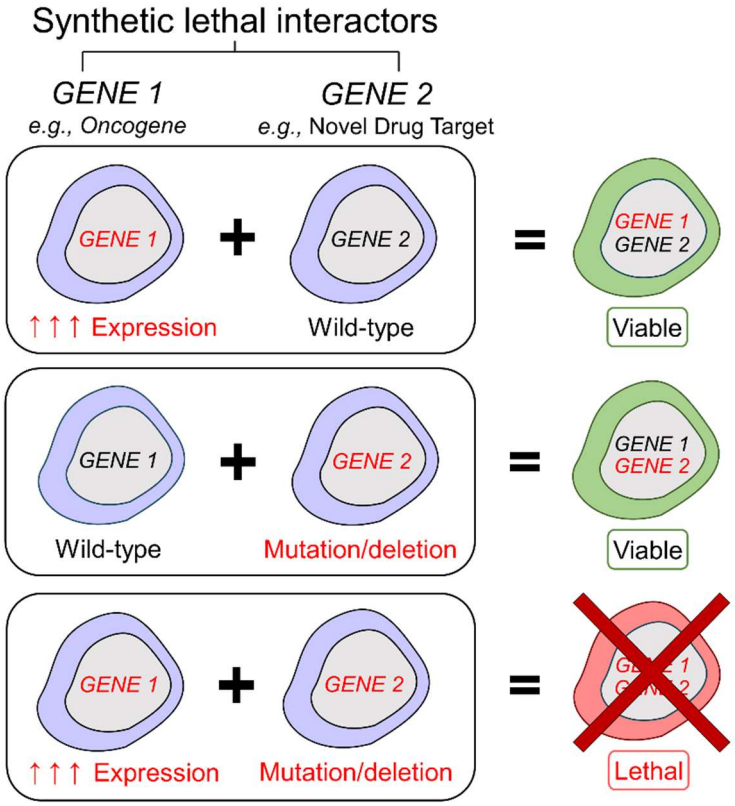

Figure 1-5. The Synthetic Dosage Lethal Paradigm.
Schematic illustrating the synthetic dosage lethal paradigm, defined as a lethal combination of the increased (*i.e.*, hypermorphic) expression of one gene (*GENE 1*) with the downregulation of another (*GENE 2*) that result in death when combined (red).

1.4.4 Methods to Identify SL Interactors

The successful translation of synthetic lethality into the clinic has ensured that it remains a prominent research area, as numerous research groups now seek to identify promising and clinically actionable SL interactors[98-100]. Many genetic and biochemical studies routinely employ quantitative screening methods and/or *in silico* approaches to identify SL interactors of genes that are mutated and/or deleted in cancer (*i.e.*, novel drug targets). For example, SL interactions have been identified using high-throughput short interfering RNA (siRNA)-based screens, as they are a well-established and effective means to identify clinically relevant SL interactions, such as *PARP1* and *PALB2*[99,123,124]. More recently, advancements in state-of-the-art genetic technologies, such as CRISPR/Cas9, have made large-scale genetic SL screens even more attainable within a variety of cancer contexts[125-127], despite the increased technical challenges and costs associated with these approaches. In fact, CRISPR screens are now commonly employed and are considered a "gold-standard approach" for genetic research studies seeking to identify novel and clinically actionable SL interactors[106].

Bioinformatic studies have shown that evolutionarily conserved synthetic genetic interactions can also be successfully identified and translated into human disease contexts by employing *in silico* approaches[99,113,128]. More specifically, data visualization tools (cBioPortal), bioinformatic analyses (R programming) and large-scale publicly available datasets (the Biological General Repository for Interaction Datasets[129]; BioGRID) are excellent resources that can be employed to identify networks of evolutionarily conserved, candidate SL interactions for testing in human cancer contexts[106]. Detailed further in ***Section 3.8.2***, BioGRID[129] contains genetic and protein interaction data from both humans and model organisms and can be utilized to identify evolutionarily conserved drug targets for downstream *in vitro* validation. Indeed, Sajesh *et al.*[99] employed *in silico* approaches and BioGRID to identify putative SL interactors of RAD54 Homolog B (*RAD54B*) an established CIN gene, through which they identified *SOD1* as a novel SL interactor of *RAD54B* in colorectal cancer contexts following *in vitro* validation. In a similar manner, *in silico* approaches could be utilized alongside genetic screening methods to streamline the identification of novel SL interactors of other CIN genes that have been implicated in cancer development, including *SKP1*, *CUL1*, or *RBX1*.

CHAPTER 2. RATIONALE, HYPOTHESIS & RESEARCH AIMS

2.1. RATIONALE

HGSOC is the most commonly diagnosed histotype of epithelial ovarian cancer and remains the most lethal gynecological malignancy. This is largely attributed to the fact that there are no early detection methods and that the etiological events driving HGSOC development and progression remain poorly understood. In this regard, it is perhaps unsurprising that >80% of HGSOC patients are diagnosed at late stages (III and IV), when survival rates are drastically reduced and therapeutic options are limited. As ~70-80% of HGSOC patients experience tumor recurrence and succumb to drug resistant disease, it is imperative that new and more effective treatment strategies are identified to improve HGSOC patient outcomes. CIN is an enabling hallmark of virtually all cancer types and was recently identified in ~95% of HGSOCs; however, the molecular determinants (*i.e.*, aberrant genes, proteins and pathways) underlying CIN have only just begun to be evaluated in ovarian cancer contexts. In this regard, *SKP1*, *CUL1* and *RBX1* have been identified as novel CIN genes in HGSOC precursor cells and diminished expression of these genes is now suspected to contribute to HGSOC pathogenesis. Although the role of CIN in HGSOC development has yet to be fully elucidated, it is of great interest given its potential clinical utility in the development of novel precision medicine strategies.

Synthetic lethality is an innovative therapeutic strategy that can be employed to selectively target and kill cancer cells harbouring distinct genetic susceptibilities (*e.g.*, defects in *RBX1*), while minimizing the off-target effects that are commonly associated with traditional chemotherapeutics. Therefore, identifying novel SL interactors of the SCF complex may uncover additional treatment strategies to improve the lives and outcomes of HGSOC patients. My Master of Science thesis seeks to identify novel drug targets for HGSOC by identifying SL interactors of *SKP1*, *CUL1* and *RBX1* in clinically relevant FT secretory epithelial cell lines.

2.2. HYPOTHESIS & RESEARCH AIMS

I hypothesize that reduced expression of *SKP1*, *CUL1*, or *RBX1* can be therapeutically targeted by identifying novel SL interactors. This hypothesis is addressed through the execution of two Research Aims.

Aim 1: To Identify and Prioritize SL Interactors of SCF Complex Members.

Aim 2: To Validate Prioritized Putative SL interactors of the SCF Complex.

CHAPTER 3. MATERIALS & METHODS

3.1 REAGENTS

All reagents and solutions employed within this study were purchased from ThermoFisher Scientific, Sigma-Aldrich and Gibco (Life Technologies) and are listed in ***Appendix A***.

3.2 CELL CULTURE

The key characteristic features of the two adherent cell lines employed in this study are summarized in ***Table 3-1***. Two FT cell lines, FT194 and FT246, were generated by Dr. R. Drapkin (University of Pennsylvania, USA) and generously provided by Drs. G. DiMattia and T. Shepherd (University of Western Ontario, Canada) with permission.

Table 3-1. Properties of Human Cell Lines Employed in this Thesis.

Cell Line	FT194	FT246
Organism	Human	Human
Tissue	FT	FT
Cell Type	Secretory Epithelial, Immortalized (TERT; SV40 TAg), Non-transformed, Non-malignant	Secretory Epithelial, Immortalized (TERT; p53shRNA; CDK4-R24C), Non-transformed, Non-malignant
Properties	Adherent	Adherent
Sex	Female	Female
Growth Medium	DMEM/F12 + 2% Ultroser G	DMEM/F12 + 2% Ultroser G
Doubling Time	~24 hours	~36 hours
Modal Karyotype	46, XX, Stable	46, XX, Stable
Source	Dr. R. Drapkin (University of Pennsylvania)	Dr. R. Drapkin (University of Pennsylvania)

3.2.1 Cell Passaging

FT194 and FT246 cells were cultured in Dulbecco's Modified Eagle Medium (DMEM)/F12 supplemented with 2% Ultroser G (***Appendix A; Tables S1-S3***) and maintained in 10 centimeter (cm) tissue culture dishes (Starstedt) in a humidified incubator at 37 degrees Celsius (°C) containing 5% CO_2. To generate humidity and prevent microbial and fungal growth, a dish containing Milli-Q water and cupric sulphate pentahydrate (***Appendix A; Table S4***) was placed in the base of the incubator. Cells were maintained at subconfluent levels and passaged

every 3-4 days in a biological safety cabinet. Medium was aspirated from the tissue culture dish and adhered cells were washed with sterile phosphate buffered saline (1× PBS; ***Appendix A***; ***Table S5-S6***). To detach cells from the dish, 1.5 millilitres (mL) of 0.05% trypsin containing ethylenediaminetetraacetic acid (EDTA) (Gibco; Life Technologies) were added and plates were incubated for 5 minutes (min) at room temperature (RT) for FT194 cells or at 37 °C for FT246 cells. Cell detachment was monitored with an inverted ID03 microscope (Zeiss) equipped with a 10× objective. Trypsin was neutralized with 3 mL of complete medium, followed by 3 mL of 1× PBS to wash any remaining cells from the bottom of the plate. For all cell lines, detached cells were collected in a 15 mL conical tube (Sarstedt) and pelleted by centrifugation at 140 × g at RT for 5 min in a Legend XFR centrifuge (ThermoFisher Scientific). The supernatant was discarded and the cell pellet was resuspended in either 5 mL (FT194) or 3 mL (FT246) of 1× PBS. Approximately (~) 1 mL of cell suspension was replated in the 10 cm tissue culture dish containing 10 mL fresh complete medium and returned to the incubator.

3.2.2 Cell Counting and Seeding

In preparation for seeding various assays, cells were passaged, pelleted and resuspended in 1× PBS as described above. To eliminate cell aggregates and obtain a single-cell suspension, cells (FT194) were passed through a 40 micrometer (μm) cell strainer. FT246 cells do not aggregate in suspension, and therefore do not require a cell strainer. Within a 0.5 mL microcentrifuge tube, an aliquot of 40 microliters (μL) of cell suspension was mixed in a 1:1 ratio with 0.2% trypan blue stain (Gibco). For each condition, a 20 μL aliquot of cell suspension/trypan blue mixture was dispensed into a cell counter slide (Cedex Smart Slide, Roche) in duplicate. The number of viable cells/mL of suspension (*i.e.*, cell counts) was assessed using a Cedex XS cell counter and associated software (Roche), which distinguishes between live and dead cells with a dye-exclusion approach (*i.e.*, stains dead/dying cells with compromised cellular membrane integrity). The average viable cell count was used to calculate the dilution of cells needed for western blots, dose response curves and subsequent direct SL tests (***Table 3-2***).

Table 3-2. Cell Seeding Densities Employed in this Study.

Treatment	Cell Seeding Density	Experimental Approach[A]	Plate Format
siRNA-based Silencing	70,000 cells/well	Western Blots	6-well plate
	1,000 cells/well	Direct SL Tests	96-well plate
Small Molecule Inhibitor	70,000 cells/well	Western Blots	6-well plate
	1,000 cells/well	Dose Response Curves	96-well plate
	1,000 cells/well	Direct SL Tests	96-well plate

[A]SL, synthetic lethal

3.3 siRNA-BASED GENE SILENCING

For each gene of interest, a set of four individual ON-TARGETplus siRNA duplexes targeting distinct regions of the respective gene coding sequence and siControl were purchased from Dharmacon. Briefly, individual siRNA duplexes were resuspended in 1× siRNA buffer (Dharmacon; ***Appendix A***; ***Table S7***) to a stock concentration of 20 µM and a working concentration of 10 µM. A pooled siRNA mixture was prepared by combining equimolar volumes (10 µM) of the four individual siRNA duplexes. Small 10 µL aliquots of each siRNA were stored at -80 °C and were thawed and frozen as needed for a maximum of 5 freeze/thaw cycles. To perform forward siRNA-based transfections, cells were seeded as described in ***Table 3-2*** for the appropriate downstream experiment and permitted to attach to the plates for 24 hours (h) at 37 °C prior to transient, lipid-mediated transfection with RNAiMAX (Invitrogen). The required volume of each transfection reagent was adjusted according to the vessel format as listed in ***Table 3-3***. For each experimental condition, siRNAs were diluted in the appropriate volume of serum-free medium (SFM) and the total volume of RNAiMAX required for the experiment was prepared in a separate tube by gently mixing with SFM medium. The siRNA and RNAiMAX solutions were mixed in a 1:1 ratio, inverted gently and allowed to incubate for 20 min at RT. Transfection mixtures were dispensed into appropriate wells and rocked gently and returned to the incubator for either 4 (FT194) or 6 (FT246) days, after which whole cell protein lysates are extracted and/or SL assays were fixed.

Table 3-3. Pipetting Volumes Employed for siRNA Transfection.

Experimental Approach[A]	Plate Format	Volume siRNA in Tube 1[B]	Volume RNAiMAX in Tube 2[B]	Volume Medium in Well	Total Volume
Western Blots	6-well plate	0.5 µL in 250 µL SFM	3 µL in 250 µL SFM	2,000 µL	2,500 µL
Direct SL Tests	96-well plate	0.05 µL in 250 µL SFM	0.3 µL in 250 µL SFM	200 µL	220 µL

[A]SL, synthetic lethal
[B]SFM, serum-free medium

3.4 WESTERN BLOT ANALYSES

Western blot analyses were employed to confirm *SKP1*, *CUL1* and *RBX1* abundance within the heterozygous knock-out clones and to evaluate the siRNA-based silencing efficiency of SL interactors of interest.

3.4.1 Whole Cell Protein Extraction

Whole cell protein extracts were harvested from asynchronous cells growing in 6-well tissue culture dishes. Cell culture medium was aspirated and cells were rinsed three times with 1 mL cold (4 °C) 1× PBS. Protein extraction buffer consisting of modified radioimmunoprecipitation assay (RIPA) buffer and protease inhibitor (complete EDTA-free; Roche) (***Appendix A***; ***Tables S8-S10***) was added to each well and allowed to incubate at 4 °C for 5 min. Cell lysates for each condition were collected using cell scrapers, transferred to 1.5 mL microcentrifuge tubes and sonicated twice for 2 seconds (s) with a Sonifer Cell Disrupter (Branson Sonic Power Co.) with a duty cycle of 50% amplitude and output control setting of 6. Samples were centrifuged (Biofuge Fresco; ThermoFisher Scientific) at 16,000 × g for 2 min at 4 °C to remove insoluble debris. The protein-containing supernatant was gently removed and transferred to new, cold, 1.5 mL microcentrifuge tubes and stored at -20 °C for short-term storage (< 2 weeks) or at -80 °C for long-term storage (> 2 weeks).

3.4.2 Protein Quantification by Bicinchoninic Acid Assay

To determine protein concentrations, the Pierce Bicinchoninic Acid (BCA) Assay kit (ThermoFisher Scientific) was employed according to the manufacturer. Briefly, Reagent A

(containing BCA) and Reagent B (containing 4% cupric sulfate) were combined in a 50:1 ratio and 200 µL/well was dispensed into a recipient 96-well plate (Corning). Nine bovine serum albumin (BSA) protein standards of known concentrations ranging from 0 to 2000 µg/mL were prepared and assessed by adding 25 µL of each standard into the recipient plate in duplicate. Experimental protein samples (5 µL/well) and RIPA (20 µL/well) were dispensed into the recipient plate in triplicate. The plate was agitated on a Multi-Microplate Genie (Scientific Industries) for 30 s and incubated in the dark at 37 °C for 1 h. Following the incubation period, a Cytation 3 Cell Imaging Multi-Mode Reader (BioTek) was employed to quantify the 562 nm absorbance for each well. A standard curve was generated from the absorbance values of the BSA standards which was used to determine the protein concentrations of the experimental samples. To determine protein concentrations, values from the triplicate sample wells were averaged and multiplied by five to account for the dilution factor.

3.4.3 Gel Electrophoresis and Western Blot

Following protein quantification, protein samples were mixed with appropriate volumes of 6× sodium dodecyl sulfate (SDS) Sample Loading Buffer (***Appendix A***; ***Tables S11-S12***) and RIPA to achieve equal protein concentrations for each condition (20 µg/well). Proteins were denatured by incubating in a heat block (Eppendorf) at 99 °C for 5 min with orbital mixing, and subsequently chilled on ice to maintain a denatured state. A precast 4-20% mini-Protean TGX polyacrylamide gel (BioRad) was assembled inside an electrophoresis tank (BioRad) and filled with 1× Running Buffer (***Appendix A***; ***Table S13-S14***). A 10 µL volume of BLUelf Prestained Protein Ladder (FroggaBio) was dispensed into one well of the gel and the remaining wells were loaded with 24 µL of denatured protein sample mixture (containing 20 µg of protein/condition). The gel electrophoresis was run for 67 min and 4 °C at 140 volts (V) using a PowerPac HC power supply (BioRad). During this time, 3× blotting pads were soaked in 1× Transfer Buffer (***Appendix A***; ***Table S15***) for ~1 hour prior to transfer. A 0.45 µm polyvinylidene difluoride (PVDF) membrane (Millipore) was activated with methanol, rinsed 3× with Milli-Q water and incubated in 1× Transfer Buffer until protein transfer. The gel and membrane were assembled in a TransBlot Semi-Dry Transfer Cell (Bio-Rad) with 1× Transfer Buffer and a constant voltage of 14 V was applied for 40 min at RT to transfer the proteins to the PVDF membrane. To confirm efficient protein transfer, PVDF membranes were incubated for 5 min at RT in the protein stain copper phthalocyanine 3,4',4'',4'''-tetrasulfonic acid tetrasodium salt (CPTS; ***Appendix A***;

Table S16). The membranes were de-stained by washing for 10 min in Tris-buffered saline solution containing 0.1% Tween20 (1× TBST; ***Appendix A***; ***Table S17-S18***), followed by 1 h incubation at RT in blocking solution composed of 5% weight/volume (w/v) non-fat milk in 1× TBST (***Appendix A***; ***Table S19***). Following the incubation period, the blocking solution was discarded and the blots were cut to separate the regions of interest (*e.g.*, separate PARP1 from the loading control, Cyclophilin B). A primary antibody targeting each protein of interest was diluted in 5% w/v milk solution to the appropriate concentration (***Table 3-4***) and dispensed over the membrane(s), which were subsequently incubated overnight (O/N) at 4 °C with gentle rocking. The following day, the primary antibody solution was discarded and the membrane(s) were rinsed with 1× TBST three times for 10 min intervals on a Belly Dancer (Stovall Life Science Inc.) at medium speed. A secondary antibody conjugated to horseradish peroxidase (HRP) and targeting the appropriate species was diluted in 5% w/v milk solution to the appropriate concentration (***Table 3-4)*** and dispensed over the membrane(s), which were incubated for 1 h at RT with gentle rocking. Finally, the secondary antibody solutions were discarded and the blots were rinsed with 1× TBST three times for 10 min intervals prior to semi-quantitative analysis as detailed below.

Table 3-4. Antibodies Employed for Western Blot.

Epitope[A]	Supplier	Catalog Number	Species	[WB][B]
Primary Antibodies				
α-Tubulin*	Abcam	ab7291	Mouse	1:20,000
CDK2	Abcam	ab32147	Rabbit	1:2,000
CHEK2	Abcam	ab109413	Rabbit	1:2,000
CUL1	Abcam	ab75812	Rabbit	1:1,000
Cyclophilin B*	Abcam	ab16045	Rabbit	1:25,000
PARG	ThermoFisher Scientific	TA808614	Mouse	1:1,000
PARP1	Abcam	ab6079	Rabbit	1:7,500
RBX1	Abcam	ab133565	Rabbit	1:30,000
SKP1	Abcam	ab76502	Rabbit	1:2,000
Secondary Antibodies				
Anti-Rabbit HRP	Jackson ImmunoResearch	111-035-144	Goat	1:15,000
Anti-Mouse HRP	Jackson ImmunoResearch	115-035-146	Goat	1:10,000

[A]Protein targeted by the antibody. Note: proteins listed with an asterisk were employed as western blot loading controls. HRP, Horseradish peroxidase.
[B]Antibody dilution employed for western blot (WB) analyses.

3.4.4 Semi-quantitative Immunoblot Analysis

To visualize proteins of interest, the EZ-ECL kit (FroggaBio) was utilized as described by the manufacturer. To prepare the visualization solution, the stable peroxide solution and the luminol/enhancer solution were combined in a 1:1 ratio and ~750 µL were applied to the membrane, which was left to incubate in the dark for 5 min at RT. Excess visualization solution was removed by gently dabbing the edge of the blot on a kimwipe and the membrane was placed into a clear page protector. The protein of interest was visualized by standard chemiluminescence utilizing a MyECL imager (ThermoFisher Scientific) and images were acquired using exposure times producing a strong signal without pixel saturation. Images were imported into ImageJ software (National Institutes of Health) to perform semi-quantitative analyses of protein expression levels, where band intensities were first normalized to the corresponding loading control (Cyclophilin B or α-tubulin) and are subsequently presented relative to a control sample

(*e.g.*, siControl or Non-Targeting Control [NT-Control]), which is set to 100 to enable semi-quantitative comparisons of protein expression levels between conditions. Figures were assembled in Photoshop CS6 (Adobe).

3.5 SL ASSAYS

3.5.1 Screening the DDR Library

The siRNA library targeting 239 DDR genes (Dharmacon) was arrayed across three 96-well plates, where each well contains a pooled siRNA comprised of four desiccated siGENOME siRNA duplexes (0.5 nmol total) targeting distinct regions of the coding sequence for each DDR gene. The siRNAs were resuspended in 50 µL of 1× siRNA buffer to a stock concentration of 10 µM and were aliquoted and arrayed across 4 × V-bottom 96-well plates (siDDR-1, -2, -3 and -4; Abgene storage plate; ThermoFisher Scientific) containing 8 µL siRNA solution per well to minimize freeze-thaw cycles. Within each siRNA plate, negative controls were added in duplicate by dispensing 8 µL of 10 µM siControl (non-targeting). In addition, positive transfection controls were added in duplicate by dispensing 8 µL of 10 µM pooled siRNAs targeting Polo-like kinase 1 (*PLK1*; an essential gene), as *PLK1* silencing induces cell death[130,131]. Plates were stored at -20 °C and employed within ~1 month to preserve the quality of the siRNAs. To perform SL screens within FT194 (NT-Control, *CUL1*$^{+/-}$-1) and FT246 (NT-Control, *SKP1*$^{+/-}$-1, *SKP1*$^{+/-}$-2, *RBX1*$^{+/-}$-1, *RBX*$^{+/-}$-2), each clone was seeded into 96-well plates at a density of 1,000 cells/well on day 0 of the screen (***Figure 3-1***). On day 1, DDR library pools were transfected into each cell line according to the manufacturer. Briefly, for each well of a 96-well plate, 0.05 µL of 10 µM siRNA targeting a given DDR gene were mixed in 10 µL serum-free medium. In a separate 50 mL conical tube, 0.15 µL RNAiMAX was added to 10 µL serum-free medium for each well. Each siRNA-containing V-bottom plate was gently mixed in a 1:1 ratio with the RNAiMAX solution, sealed and incubated at RT for 20 min. For each silencing condition within the siDDR-1, -2, -3 and -4 plates, 20 µL of the siRNA/RNAiMAX mixture (siRNA [50 nM]) were added to each well within the FT194 (NT-Control, *CUL1*$^{+/-}$-1) and FT246 (NT-Control, *SKP1*$^{+/-}$-1, *SKP1*$^{+/-}$-2, *RBX1*$^{+/-}$-1, *RBX*$^{+/-}$-2) plates and returned to the incubator. To account for differences in doubling times and ensure equal numbers of cell cycles, transfected cells were either fixed 96 h (FT194) or 144 h (FT246) post-transfection with 4% (w/v) paraformaldehyde (***Appendix A***; ***Table S20***) and counterstained with Hoechst 33342 (300

ng/mL; ThermoFisher Scientific) in 1× PBS (***Appendix A***; ***Table S21-S22***). Plates were stored at 4 °C overnight and imaged the following day with a Cytation 3 (BioTek; detailed in ***Section 3.5.4***). To account for potential differences in growth rates between cell lines, the nuclear count for each well was normalized to the average nuclear counts for the two siControl conditions contained with each plate. To determine the magnitude of the SL phenotypes, a SL ratio was calculated for each DDR gene and is defined as the normalized nuclear count within the NT-control condition divided by the normalized nuclear count within the experimental condition. For each cell line, a minimum threshold of SL ratio > 1.25 was applied to identify putative SL interactors.

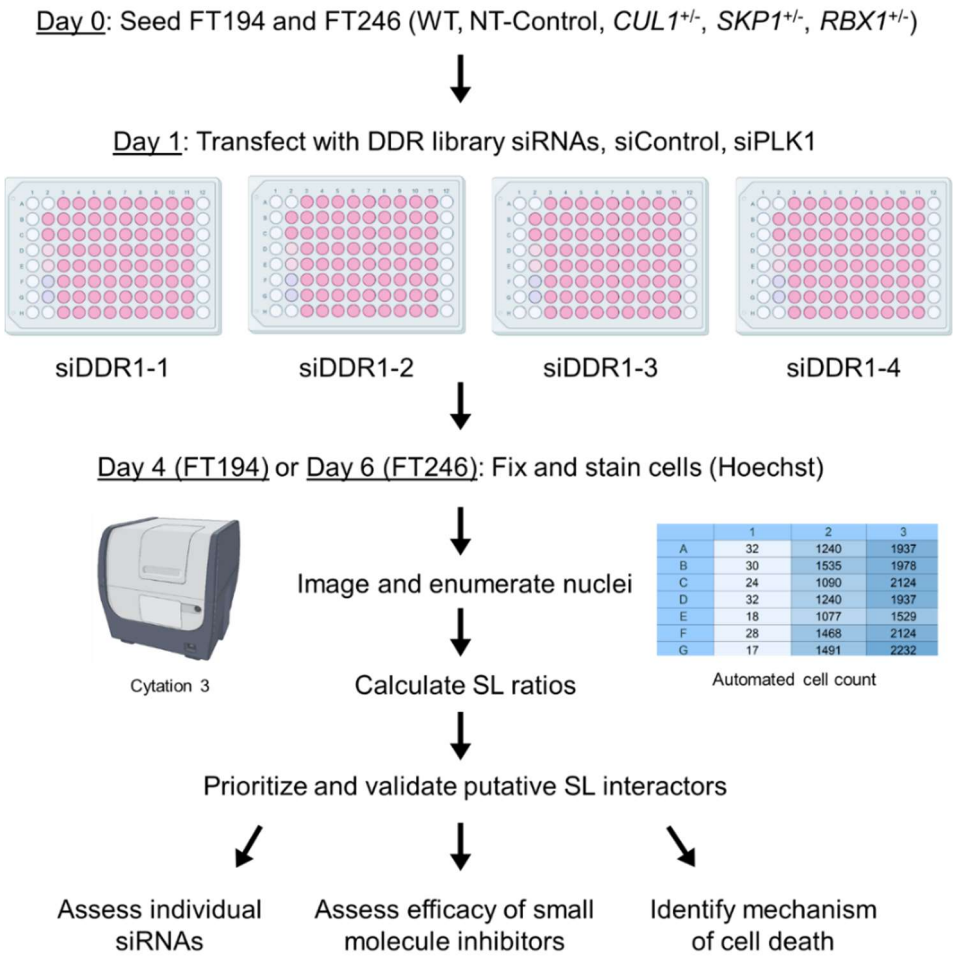

Figure 3-1. Experimental Workflow of the siRNA-based Screen Performed in *Aim 1*.
RNAi-based screen of *SKP1*, *CUL1* and *RBX1* knockout and NT-control clones to identify putative SL interactors within the DDR library. Putative SL interactors are prioritized based on the magnitude of the SL ratio, reproducibility of the SL phenotypes amongst the various knockout clones and the availability of small molecule inhibitors (SMIs). Prioritized candidates are subsequently validated through a series of direct SL tests.

3.5.2 Direct SL Tests

Putative SL interactors were prioritized based on the magnitude of the SL phenotype (*i.e.*, SL ratio), the reproducibility between the knockout clones, the availability of small molecule inhibitors (SMIs) and whether the SL interactors are evolutionarily conserved in model organisms (*e.g.*, *S. cerevisiae*). Briefly, 1,000 cells are seeded per well on day 0, permitted to attach and are transfected 24 h post seeding. On day 1, individual (siDDR-1,-2,-3,-4) or pooled (siDDR-Pool) ON-TARGETplus siRNA duplexes targeting the DDR gene of interest (*i.e.*, the prioritized putative SL interactor) were utilized. Briefly, 0.05 µL of 10 µM siRNA were mixed in 10 µL serum-free medium. In a separate 1.5 mL microcentrifuge tube, 0.3 µL RNAiMAX was added to 10 µL serum-free medium for each well. The FT246 NT-Control, *RBX1*$^{+/-}$-1, *RBX*$^{+/-}$-2 clones were then transfected, fixed, counterstained as detailed in ***Section 3.5.1***. Plates were stored at 4 °C overnight and imaged the following day with a Cytation 3 (BioTek; see ***Section 3.5.4***).

3.5.3 Small Molecule Inhibitor Dose-Response Curves

Standard dose-response curves[128] were generated using 10- or 5-fold serial dilutions of Olaparib (PARP1 inhibitor; 100 µM to 256 pM; Selleckchem) and SNS-032 (CDK2 inhibitor; 100 µM to 1 pM; Selleckchem), respectively. Dose response curves were performed a minimum of two times with each concentration assessed in sextuplet within the FT246 clones (NT-Control, *RBX1*$^{+/-}$-1, *RBX*$^{+/-}$-2) in a 96-well plate format. Briefly, FT246 NT-Control, *RBX1*$^{+/-}$-1 or *RBX1*$^{+/-}$-2 clones were dispensed into each well of a 96-well plate in 200 µL of media. The following day, 50 µL of complete media supplemented with either 10- or 5-fold serial dilutions of Olaparib, SNS-032 or vehicle control (dimethyl sulfoxide; DMSO). Cells were permitted to grow for 6 days (~4 doubling times), at which point they were fixed with 4% (w/v) paraformaldehyde and nuclei were counterstained with Hoechst (detailed in ***Section 3.5.1***). Plates were stored at 4 °C overnight and imaged the following day using a Cytation 3 (BioTek; detailed in ***Section 3.5.4***). Data (nuclear counts) were imported into Prism v9 (GraphPad) and the average nuclear count from the six technical replicates was calculated and normalized to the average nuclear count from the appropriate control (DMSO) for each condition. For the SMIs employed in this study, the normalized nuclear counts from the NT-Control were compared to the normalized nuclear counts from each experimental condition (*RBX1*$^{+/-}$). All data were transformed to a logarithmic scale and dose response curves were fit using a sigmoidal nonlinear

regression model (log[inhibitor] vs. response - variable slope), as detailed elsewhere[128]. An Effective Concentration 50 (EC50) value was determined from each dose response curve and is defined as the concentration of the SMIs that results in the half-maximal response (normalized cell numbers) relative to the DMSO control. The concentrations of SMIs that induced the greatest SL phenotypes within the *RBX1*$^{+/-}$ clones were validated by performing additional direct SL tests a minimum of three times and employed for all subsequent experiments.

3.5.4 Single-cell Quantitative Imaging Microscopy

Following direct SL tests and dose response curves, 96-well plates were imaged using a Cytation 3 Cell Imaging Multi-Mode Reader (BioTek) with the number of nuclei imaged employed as a surrogate marker for cell numbers using the automated Gen5 software (BioTek). The Cytation 3 is equipped with a 16-bit, charge-coupled device camera (Sony) and for each well, 16 non-overlapping 2D images (4 × 4 matrix) were acquired using an Olympus 10× objective (0.3 numerical aperture).

3.6 FLUORESCENCE IMAGING MICROSCOPY

3.6.1 Semi-Quantitative Indirect Immunofluorescent (IIF) Labeling

Semi-quantitative IIF labeling of γ-H2AX and cleaved Caspase-3 was performed a minimum of three times for the FT246 NT-Control, *RBX1*$^{+/-}$-1 and *RBX1*$^{+/-}$-2 clones. Cells were seeded at ~90% confluency onto ethanol-sterilized glass coverslips (18 × 18 mm) in a 6-well culture plate prior to fixation. After 24 h, cells were fixed with freshly prepared 4% (w/v) paraformaldehyde for 10 min at RT. After fixing, the paraformaldehyde was removed and the cells were washed three times with 1× PBS. Cell membranes were permeabilized with 1× PBS containing 0.5% (v/v) Triton X-100 (***Appendix A***; ***Table S23***) for 10 min at RT. Following three additional 1× PBS washes, the coverslips were placed cell-side down over a ~30 µL aliquot of primary antibody solution (diluted in 1× PBS; ***Table 3-5***) and incubated overnight at RT in a humidified chamber to prevent desiccation. Coverslips were returned to the 6-well culture plate and rinsed once with 1× PBS and incubated with 1× PBS containing 0.1% (v/v) Triton X-100 (***Appendix A***; ***Table S24***) for 5 min. Coverslips were rinsed three additional times with 1× PBS and placed cell-side down over a ~30 µL aliquot of secondary antibody solution (diluted in 1× PBS; ***Table 3-5***) and allowed to incubate at RT for at least 1 h in the dark. Coverslips were

returned to the 6-well plate and rinsed with 1× PBS containing 0.1% (v/v) Triton X-100, followed by three additional washes with 1× PBS. Coverslips were mounted onto glass slides containing a ~10 µL aliquot of 4′,6-diamidino-2-phenylindole (DAPI) in mounting media (***Appendix A***; ***Tables S25-S26***). For SMI treatments, media containing Olaparib, SNS-032 or DMSO was added to wells 24 h post cell seeding and grown for an additional 48 h. Bleomycin was employed as a positive control for DNA DSBs (γ-H2AX labeling) and apoptosis (cleaved Caspase-3 labeling), as described elsewhere[128]. Briefly, cells were treated with 0.1 µg/mL of Bleomycin and fixed 2 h post-treatment. Slides were stored at 4 °C and protected from light for a minimum of 24 h prior to imaging to enable DAPI to equilibrate across all nuclei.

Table 3-5. Antibodies Employed for IIF.

Epitope[A]	Supplier	Catalog Number	Species	[IIF][B]
Primary Antibodies				
γ-H2AX	Abcam	ab26350	Mouse	1:200
Secondary Antibodies				
Anti-Mouse Cy3	Abcam	ab97035	Goat	1:200

[A]Protein targeted by the antibody.
[B]Antibody dilution employed for IIF.

3.6.2 High-Resolution Semi-Quantitative Fluorescence Imaging Microscopy

IIF images were collected using an AxioImager Z2 microscope (Zeiss) equipped with an AxioCam HRm CCD (Zeiss), a 40× oil immersion Plan-Apochromat lens (1.30 numerical aperture) and DAPI and Cy3 filters (Zeiss). Exposure times were independently optimized for each channel and maintained constant throughout imaging, while semi-quantitative imaging analyses were employed to compare the relative abundance of γ-H2AX within the FT246 NT-Control, *RBX1*$^{+/-}$-1 and *RBX1*$^{+/-}$-2 clones. Briefly, the number of γ-H2AX Irradiation-induced foci (IRIF)-like foci, an established surrogate marker of DNA DSBs[132], were determined for each nucleus following treatment with Olaparib or SNS-032 and compared to the DMSO condition. Images were assembled in Imaris v9.6.0 (Bitplane) image analyses and presentation software. All channels (*e.g.*, DAPI and Cy3) were imported into Imaris and the pixel dimensions were adjusted to reflect the pixel dimensions of the camera and 40× objective (x/y dimensions; 0.102 µm × 0.102 µm). Individual channels are typically presented in black and white, while the

merged images are pseudo-coloured red or green for the DAPI and Cy3 channels, respectively. All images were exported as TIFFs and panels were assembled in Photoshop CS6.

3.7 BIOINFORMATIC APPROACHES

3.7.1 Gene Copy Number Alterations

All *SKP1*, *CUL1* and *RBX1* copy number alteration (CNA) data were acquired from The Cancer Genome Atlas (TCGA; Pan-Cancer Atlas data)[15] with all data extraction and visualization performed using cBioPortal (www.cbioportal.org)[96,119]. CNAs were identified using the following cBioPortal OncoQuery Language commands: (1) HOMDEL (deep deletion; loss of both alleles); (2) HETLOSS (shallow deletion; loss of one allele); (3) GAIN (gain of one allele); and (4) AMP (large amplification; gain of two or more alleles). To determine the prevalence of *SKP1*, *CUL1* and *RBX1* CNAs in cancer, patient-derived, publicly available data from 10 commonly diagnosed cancer types (bladder, breast, colon, head & neck, lung, melanoma, ovarian, pancreatic, stomach and uterine) were extracted from TCGA Pan-Cancer Atlas[15]. *SKP1*, *CUL1* and *RBX1* CNA data were imported into Prism v9 and shallow deletions were plotted for 10 common cancer types. All figures were assembled in Photoshop CS6.

3.7.2 Bioinformatic Analyses to Identify Putative SL Interactors of the SCF Complex

To identify putative SL interactors capable of exploiting *SKP1*, *CUL1* and *RBX1* copy-number losses, SynLethDB[133,134] (http://synlethdb.sist.shanghaitech.edu.cn/), UniProtKB[135] and BioGRID[129] (https://thebiogrid.org/) were combined with *in silico* approaches to extract pre-existing SL data from model organisms to identify candidate SL interactions that may be evolutionarily conserved in humans. SynLethDB[133,134] is a database containing ~50,000 SL gene pairs identified through biochemical assays, *in silico* approaches and text mining within humans and various model organisms (*e.g.*, *Mus musculus*). Genes were queried by human gene name (*e.g.*, *RBX1*) and SL interactor data were exported into Excel (Microsoft). In addition, the UniProtKB[135] database (https://www.uniprot.org/) was employed to identify the functional orthologs of *SKP1*, *CUL1* and *RBX1* within *S. cerevisiae* (*ScGENE*). The corresponding UniProtKB[135] Entry number for *ScSKP1 ScCUL1* and *ScRBX1* was queried within BioGRID to mine published genetic interactions within *S. cerevisiae*, as described elsewhere[106]. BioGRID contains genetic and protein interaction data from both humans and various model organisms

(*e.g.*, *S. cerevisiae*; *Drosophila melanogaster*) and is comprised of more than 70,000 publications detailing both individual studies and high-throughput datasets (*e.g.*, Costanzo[107] *et al.*), and is ideal for studies seeking to identify evolutionarily conserved SL interactions and subsequent downstream bioinformatic analyses. Published genetic interactions classified as "synthetic lethality", "synthetic growth defect" and "negative genetic interactions" were used to identify candidate SL interactions that may be evolutionarily conserved in humans. All data were exported into Excel and figures were assembled in Photoshop CS6.

3.8 STATISTICAL ANALYSES

The number of experimental/biological replicates (N) and technical replicates (n) are indicated for all experiments presented in this thesis. All statistical analyses were performed using Prism v9.

3.8.1 Direct SL Tests

Data (nuclear counts) were imported into Prism v9 and the average nuclear count from the six technical replicates was calculated and normalized to the average nuclear count from the respective control (siControl) for each condition. For each condition (*e.g.*, siRNA or SMI), the normalized nuclear counts from the NT-Control cells were compared to the normalized nuclear counts from each experimental condition (*e.g.*, $RBX1^{+/-}$). The average normalized nuclear counts were imported into Prism v9, where paired *t*-tests were employed to assess the statistical reproducibility of each condition across experimental replicates. A p-value < 0.05 was considered statistically significant.

3.8.2 Semi-Quantitative Fluorescence Imaging Microscopy

Data were imported into Prism v9 and the number of γ-H2AX foci was calculated for each condition, where the number of γ-H2AX foci within the DMSO condition was compared to the number of γ-H2AX foci following treatment with Olaparib or SNS-032 within NT-Control cells and $RBX1^{+/-}$ clones. Data were imported into Prism v9, where Kolmogorov-Smirnov (KS) tests were employed to assess the statistical significance of each condition. A p-value < 0.05 was considered statistically significant.

CHAPTER 4. RESULTS

4.1 AIM 1: To Identify and Prioritize SL Interactors of SCF Complex Members

4.1.1 Employing In Silico Approaches to Identify Putative SL Interactors of the SCF Complex

To identify putative SL interactors capable of exploiting human *SKP1*, *CUL1* and *RBX1* copy-number losses, *in silico* approaches were employed to extract pre-existing SL data from humans and model organisms (*e.g.*, *S. cerevisiae*, *D. melanogaster*). SynLethDB[133] is a database comprised SL gene pairs derived from biochemical assays and computational predictions, rendering it well-suited for *in silico* genetic analyses. Using this approach, a total of 61 putative SL interactors of the SCF complex were identified, including *PARP1* and *CDK2* (***Figure 4-1***; ***Tables S27-29***). As a complimentary approach, BioGRID[129] was employed to assess whether any of the SL pairs identified with SynLethDB[133] are evolutionarily conserved within *S. cerevisiae*, as previous genetic studies have shown that evolutionarily conserved SL interactions can be identified by employing cross-species approaches[106]. Of those identified (***Tables S30-32***), *S. cerevisiae CDC28* (*i.e.*, the functional ortholog of human *CDK2*), was identified as a SL interactor of *S. Cerevisiae CDC53* (*i.e.*, functional ortholog of human *CUL1*), further highlighting its potential relevance as a therapeutic target for HGSOCs harbouring alterations in SCF complex member genes.

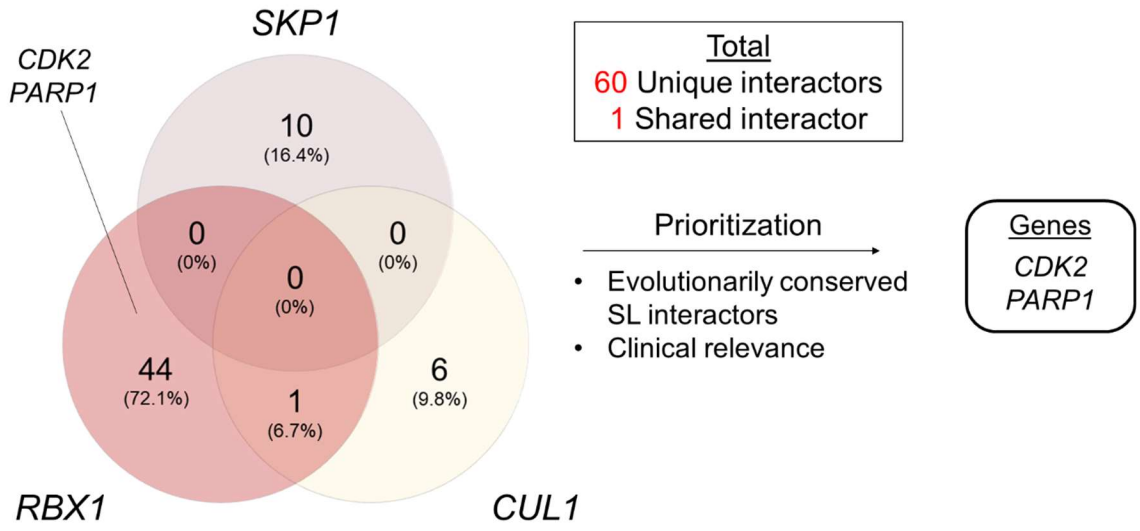

Figure 4-1. SynLethDB Identifies Putative SL Interactors of *SKP1*, *CUL1* and *RBX1*.
Venn diagram presenting the number of putative SL interactors identified from SynLethDB[133] for *SKP1*, *CUL1* and *RBX1*, with 2 prioritized candidates indicated.

4.1.2 Confirming Reduced Protein Expression in FT194 and FT246 Clones

To confirm reduced protein expression in the heterozygous knockout clones that were previously generated in the FT194 and FT246 cell lines, proteins were harvested from FT194 NT-Control, FT194 *CUL1*$^{+/-}$, FT246 NT-Control, FT246 *SKP1*$^{+/-}$-1, FT246 *SKP1*$^{+/-}$-2, FT246 *RBX1*$^{+/-}$-1 and FT246 *RBX1*$^{+/-}$-2 clones. Semi-quantitative western blot analyses reveal that FT194 *CUL1*$^{+/-}$-1 retains ~60% endogenous CUL1 abundance relative to the NT-Control clone (***Figure 4-2***). Similarly, *SKP1*$^{+/-}$-1 and *SKP1*$^{+/-}$-2 retain ~30% endogenous abundance relative to NT-Control FT246 clones, whereas *RBX1*$^{+/-}$-1 and *RBX1*$^{+/-}$-2 retain ~80% and ~60% endogenous RBX1 abundance, respectively (***Figure 4-2***). Collectively, these data confirm these heterozygous gene knockout models exhibit reduced protein abundance and therefore are suitable models in which to perform SL tests.

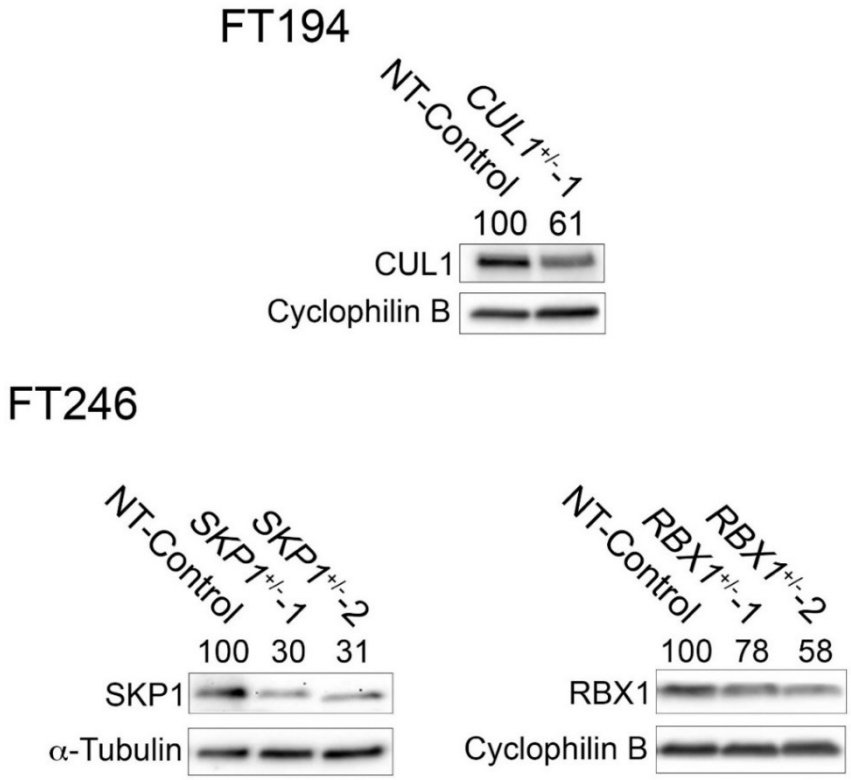

Figure 4-2. Western Blots Confirm Diminished SKP1, CUL1 and RBX1 Abundance in Heterozygous Knockout Clones.
Western blot (top) presenting CUL1 abundance in a heterozygous FT194 clone, with Cyclophilin B serving as a loading control. Semi-quantitative analyses were performed where SKP1, CUL1 and RBX1 expression levels were normalized to the corresponding loading control and are presented relative to NT-control (100). Semi-quantitative western blots (bottom) of heterozygous *SKP1* and *RBX1* FT246 clones depicting the abundance of SKP1 and RBX1, with α-Tubulin and Cyclophilin B serving as loading controls, respectively.

4.1.3 Screening DDR Genes Identify Putative SL Interactors of the SCF Complex

To identify putative SL interactors capable of exploiting *SKP1*, *CUL1* and *RBX1* copy-number losses, an siRNA-based screen of the DDR library was performed within a representative heterozygous FT clone described above (***Section 4.1.2***; FT194 [NT-Control, *CUL1*$^{+/-}$-1] and FT246 [NT-Control, *SKP1*$^{+/-}$-2, *RBX1*$^{+/-}$-1]). The DDR library is comprised of 239 genes encoding functions within DDR pathways (***Table S33***) and was purposely selected as numerous FDA approved, small molecule inhibitors exist against DDR members that may expedite pre-clinical translation. In the context of *CUL1*, silencing of 99/239 DDR genes resulted in quantitative decreases in the number of *CUL1*$^{+/-}$-1 clones relative to the NT-Control clones, identifying these 99 genes as putative *CUL1* SL interactors, including *PARP1* (***Figure 4-3***; ***Table S34***). For *SKP1* and *RBX1*, silencing of 119/239 and 70/239 DDR genes resulted in quantitative decreases in the number of *SKP1*$^{+/-}$-2 (***Figure 4-3; Table S35***) and *RBX1*$^{+/-}$-1 clones (***Figure 4-3; Table S36***), respectively, relative to the NT-Control clones, identifying them all as putative SL interactors. Collectively, 180 unique DDR genes were identified as a putative SL interactor of *SKP1*, *CUL1* or *RBX1*, 84 of which are shared between at least two clones, including *Checkpoint kinase 2* (*CHEK2*) and *Poly(ADP-Ribose) Glycohydrolase* (*PARG*).

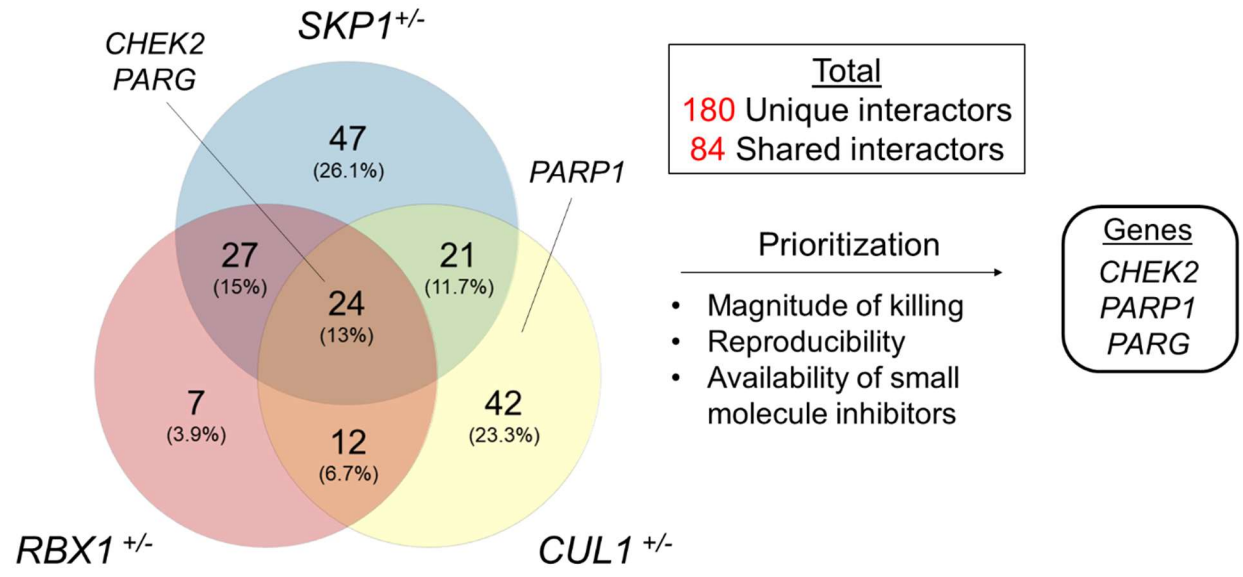

Figure 4-3. RNAi-based Screen of the DDR Library Identifies Putative SL interactors of *SKP1*, *CUL1* and *RBX1*.
Venn diagram presenting the number of putative SL interactors identified from the DDR library in *SKP1*, *CUL1* and *RBX1* heterozygous knockout clones, with 3 prioritized candidates indicated.

The putative SL interactors identified in the siRNA-based screen were subsequently prioritized based on the magnitude of killing, the conservation of SL interactions across species and between knockout clones, and the availability of SMIs. Based on this prioritization scheme and the *in silico* data (***Section 4.1.1***), *CHEK2*, *PARG*, *PARP1* and *CDK2* were selected for subsequent study (***Figure 4-4***).

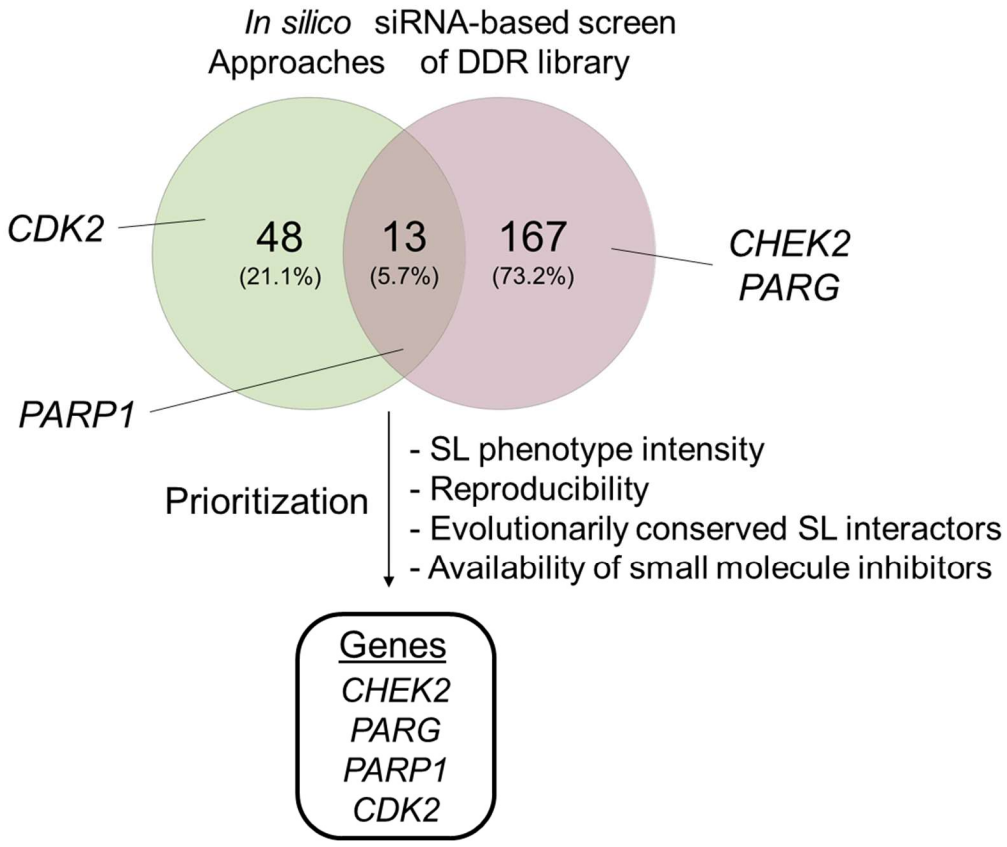

Figure 4-4. *In Silico* and RNAi-based Approaches Identify Putative SL interactors of the SCF Complex Members.
Venn diagrams presenting the number of putative SL interactors identified from SynLethDB[133] and the DDR library in *SKP1*, *CUL1* and *RBX1* heterozygous knockout clones, with the 4 prioritized candidates (*CDK2*; *PARP1*; *CHEK2*; *PARG*) indicated.

4.2 AIM 2: To Validate Prioritized Putative SL Interactors of the SCF Complex

4.2.1 *RBX1*$^{+/-}$ Clones are Sensitive to *CHEK2* Silencing

As the initial *in silico* approaches and siRNA-based screen did not assess DDR protein expression or knockdown efficiency within the respective knockout clones, it is critical that these be assessed to confirm putative SL interactors. With the knowledge that heterozygous loss of *RBX1* occurs in ~81% of ovarian cancers[15,119] (detailed in ***Section 1.3.4***), while *SKP1* and *CUL1* are only heterozygously lost in 43% and 11%, respectively, diminished *RBX1* expression is the most clinically relevant context in which to study SL interactors and identify novel drug targets. Thus, due to clinical reasons and time constraints, only the *RBX1*$^{+/-}$ clones were used to directly assess the four prioritized SL interactors identified above.

Prior to assessing the SL interactions, it was first necessary to establish the silencing efficiencies of the siRNAs employed within the cell lines employed. In this regard, the silencing efficiencies of four individual siRNAs (siCHEK2-1, -2, -3, -4), a pooled siRNA condition (equimolar mixture of the four individual siRNAs; siCHEK2-Pool) and a non-targeting siRNA control (siControl) were transiently transfected into cells. Cells were permitted to grow for 6 days, at which time protein were extracted and semi-quantitative western blot analyses were performed (see ***Section 3.4***). As shown in ***Figure 4-5A***, western blot reveal an overall reduction of endogenous CHEK2 abundance ranging from ~1% to 20% of siControl levels, with siCHEK2-1 and siCHEK2-2 exhibiting the greatest reduction. These data show that *CHEK2* is efficiently silenced within these cells and therefore, can be employed in subsequent direct SL tests.

To determine the reproducibility of SL phenotypes initially identified above, the two most efficient individual (siCHEK2-1, -2) and pooled siRNA duplexes targeting *CHEK2* were utilized for all downstream assays. Representative images reveal visual decreases in the number of nuclei (*i.e.*, a marker for cell numbers) within the *RBX1*$^{+/-}$ clones relative to NT-Control following *CHEK2* silencing (***Figure 4-5B***). Quantification of SL phenotypes (see ***Section 3.9.1***) show trending decreases in cell numbers within *RBX1*$^{+/-}$-1 (~11 to 25% decrease) and *RBX1*$^{+/-}$-2 (~1 to 27% decrease) relative to NT-Control clones following *CHEK2* silencing (***Figure 4-5C***; ***Table S37***). In both *RBX1*$^{+/-}$ clones, these decreases were found to be statistically significant with the siCHEK2-Pool silencing condition (but not with siCHEK2-1 or -2), supporting the possibility that *CHEK2* may be a novel SL interactor of *RBX1*.

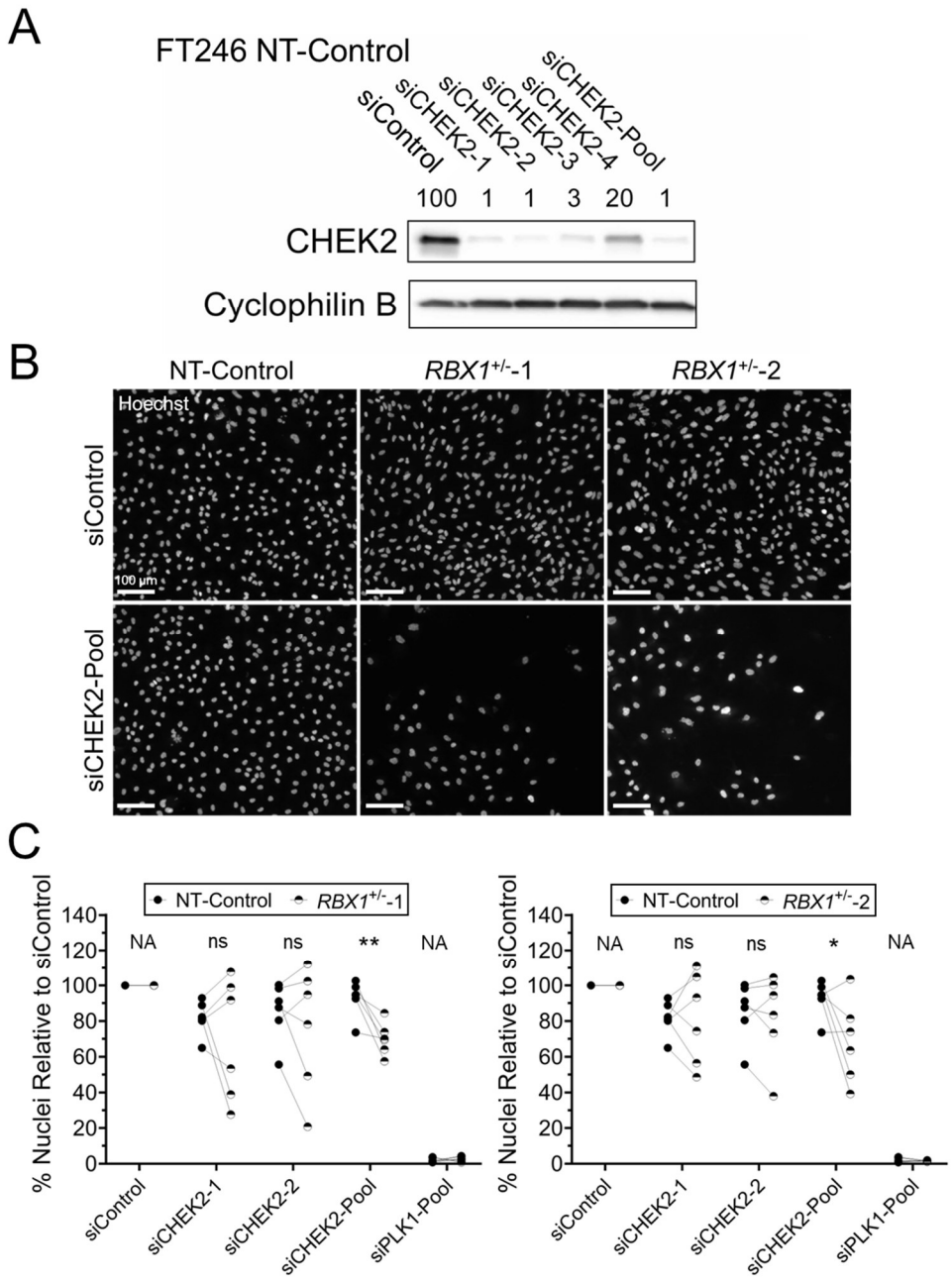

Figure 4-5. *CHEK2* is a Putative SL Interactor of *RBX1*.

(A) Semi-quantitative western blot presenting endogenous CHEK2 abundance in NT-Control cells following silencing, with Cyclophilin B serving as a loading control and the relative abundance (%) of CHEK2 presented above each lane. **(B)** Representative low resolution images of NT-Control, *RBX1*$^{+/-}$-1, *RBX1*$^{+/-}$-2 depicting reduced cell (nuclear) numbers following *CHEK2* silencing in *RBX1*$^{+/-}$ clones relative to NT-control. **(C)** Dot plots presenting the mean number of nuclei (cells) relative to siControl following *CHEK2* silencing within NT-Control (black circles) and *RBX1*$^{+/-}$ clones (black/white circles). Quantification of SL phenotypes identify trending and significant decreases in cell numbers in *RBX1*$^{+/-}$ clones relative to NT-Control cells following *CHEK2* silencing (N=6; n=6; ns = not significant; * p-value < 0.05; p-value ** ≤ 0.01).

4.2.2 *RBX1*$^{+/-}$ Clones are Sensitive to *PARG* Silencing

To validate the silencing efficiencies of siRNAs targeting *PARG*, protein extractions were generated from *PARG* silenced NT-Control clones and assessed using western blot analyses. Semi-quantitative western blot reveal that PARG abundance is reduced to ~1% to 36% of endogenous levels (NT-Control), with siPARG-2 and siPARG-3 exhibiting the greatest reduction (~6% and ~16%, respectively; ***Figure 4-6A***). Direct SL tests revealed that *PARG* silencing is associated with visual (***Figure 4-6B***) and quantitative decreases in cell numbers within *RBX1*$^{+/-}$-1 (~5 to 35% decrease; significant in all conditions) and *RBX1*$^{+/-}$-2 (~1 to 32% decrease; significant with siPARG-Pool) relative to NT-Control clones (***Figure 4-6C; Table S38***). However, despite achieving statistical significance and the general reproducibility of SL phenotypes between silencing conditions and *RBX1*$^{+/-}$ clones, *PARG* silencing also tends to be associated with moderate decreases in the number of NT-Control clones, suggesting it may also impact normally growing cells that may correspond with side effects in HGSOC patients. In this regard, although these data support the possibility that *PARG* is a novel SL interactor of *RBX1*, additional SL assays are required to better understand its potential clinical utility.

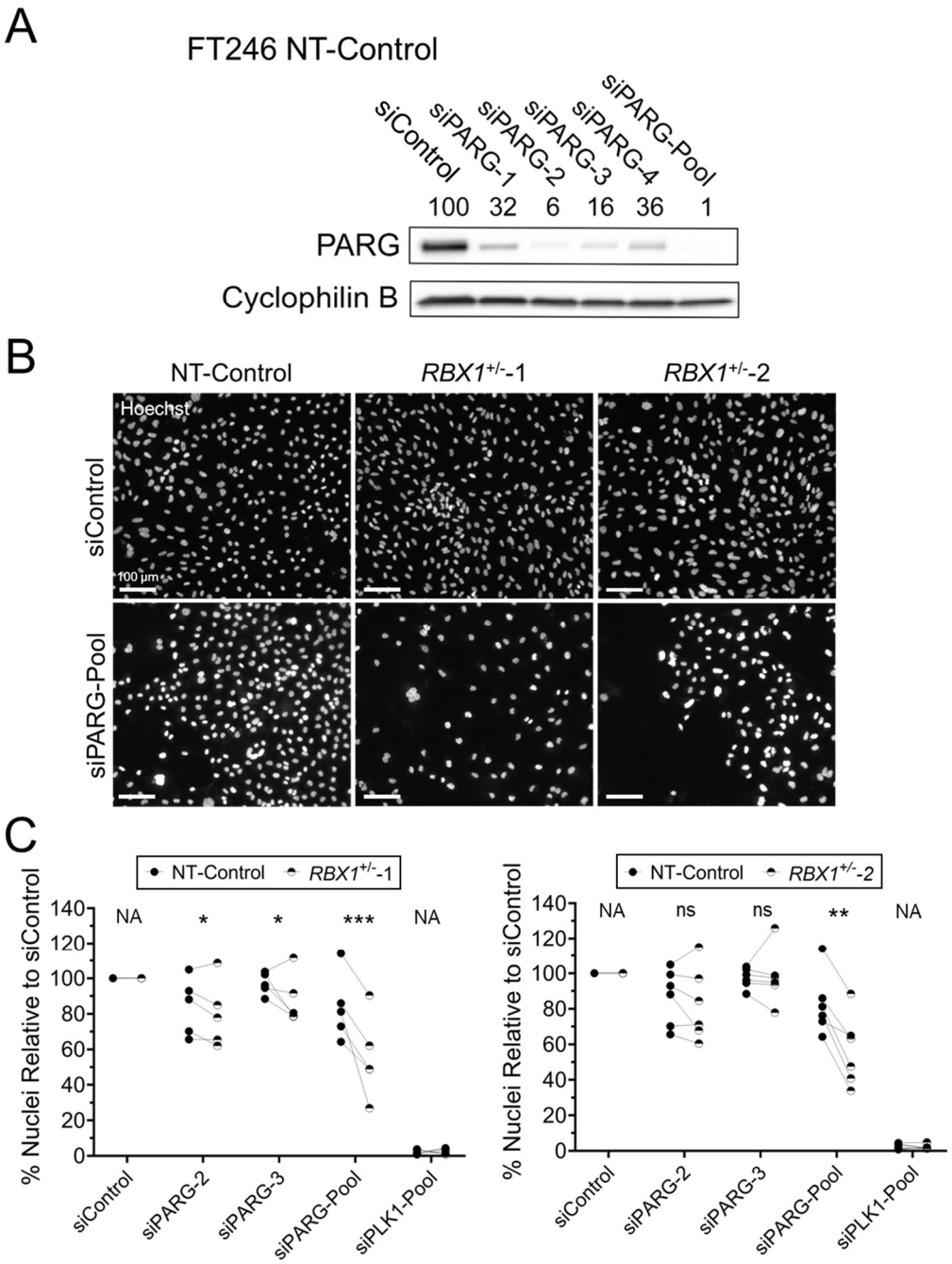

Figure 4-6. *PARG* is a Putative SL Interactor of *RBX1*.

(A) Representative western blots depicting endogenous PARG abundance in FT246 NT-Control cells following *PARG* silencing; Cyclophilin B is the loading control. **(B)** Low resolution images of NT-Control, *RBX1*$^{+/-}$-1, *RBX1*$^{+/-}$-2 depicting reduced cell numbers following *PARG* silencing in *RBX1*$^{+/-}$ clones relative to NT-control. **(C)** Dot plots presenting the mean number of nuclei relative to siControl following *PARG* silencing within NT-Control and *RBX1*$^{+/-}$ clones, reveal significant decreases in cell numbers in *RBX1*$^{+/-}$ clones following *PARG* silencing (N=5; n=6; ns = not significant; * p-value < 0.05; ** p-value ≤ 0.01; *** p-value ≤ 0.001).

4.2.3 *PARP1* Silencing Corresponds with Reduced *RBX1*$^{+/-}$ Cell Numbers

As above, semi-quantitative western blots were performed on *PARP1* silenced NT-Control cells to identify the most efficient silencing siRNA duplexes. Western blotting determined that PARP1 abundance is reduced to <8% in each condition relative to siControl, with siPARP1-1 and siPARP1-2 exhibiting the greatest reduction (***Figure 4-7A***). Subsequent direct SL tests revealed visual (***Figure 4-7B***) and trending decreases within *RBX1*$^{+/-}$-1 (~4 to 19% decrease; significant with siPARP1-1) and *RBX1*$^{+/-}$-2 (~6 to 13% decrease; not statistically significant) relative to NT-Control (***Figure 4-7***; ***Table S39***). It is important to note that the heterogeneity of SL phenotypes observed in the siRNA-based direct tests may be reflective of the dynamic nature of the *RBX1* clones that exhibit ongoing CIN and are karyotypically unstable, which may result in differential responses, in addition to the technical limitations of siRNA-based approaches relative to treatment with small molecule inhibitors (discussed further in ***Section 5.2.2***). As such, the *in silico* data, siRNA-based screen and direct SL tests support the possibility that *PARP1* is a SL interactor of *RBX1*. Moreover, given its established clinical relevance in HGSOC therapies, these initial results further highlight the potential therapeutic relevance of *PARP1* for HGSOC patients exhibiting diminished expression of *RBX1*.

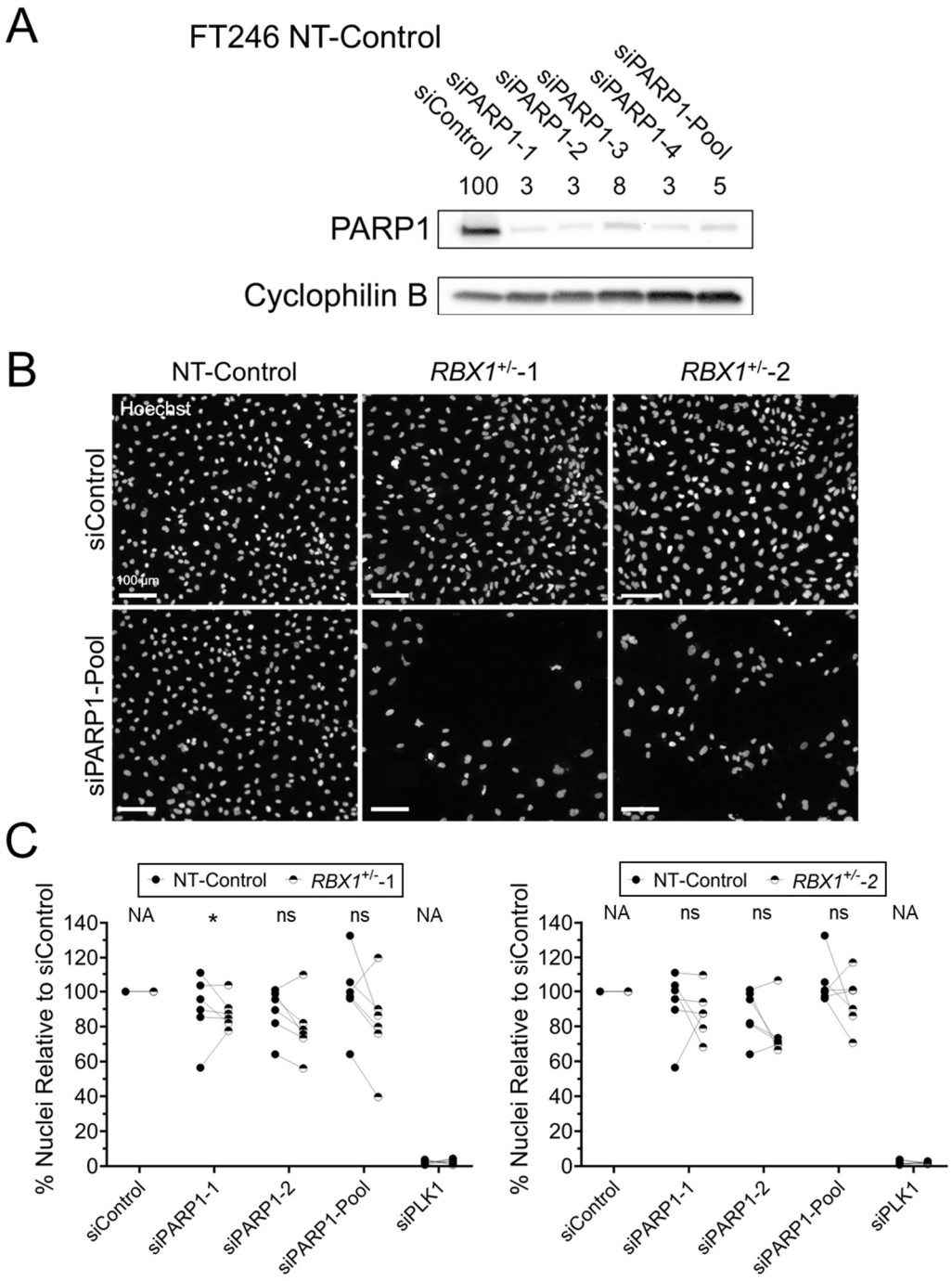

Figure 4-7. *PARP1* may be a Putative SL Interactor of *RBX1*.
(A) Representative western blot depicting endogenous PARP1 abundance in NT-Control cells following *PARP1* silencing; Cyclophilin B is the loading control. **(B)** Low resolution images of NT-Control, *RBX1*$^{+/-}$-1, *RBX1*$^{+/-}$-2 depicting reduced cell numbers following *PARP1* silencing in *RBX1*$^{+/-}$ clones relative to NT-control. **(C)** Dot plots presenting the mean number of nuclei relative to siControl following *PARP1* silencing within NT-Control and *RBX1*$^{+/-}$ clones, revealing trending decreases in cell numbers within *RBX1*$^{+/-}$ clones following *PARP1* silencing (N=6; n=6; ns = not significant; p-value * ≤ 0.05).

4.2.4 *RBX1*$^{+/-}$ Clones are Sensitive to Olaparib Treatments

To assess whether the SL phenotypes identified using siRNA-based approaches can be recapitulated using a clinically relevant PARP1 inhibitor, dose-response curves (*i.e.*, 2.5-fold serial dilution) were generated within *RBX1*$^{+/-}$ and NT-Control clones with Olaparib and DMSO to establish EC50 values. Briefly, an EC50 is defined as the concentration required to induce a half maximal response of a given phenotype. Data show that *RBX1*$^{+/-}$-1 and *RBX1*$^{+/-}$-2 exhibit enhanced sensitivity to Olaparib treatments relative to NT-control clones (***Figure 4-8A***), having EC50 values of 4.376 μM, 4.358 μM, and 8.863 μM, respectively. A 6.40 μM dose of Olaparib was found to induce the greatest SL phenotypes (*i.e.*, magnitude of killing) within *RBX1*$^{+/-}$ clones and was subsequently employed for additional direct SL tests. Quantification of SL phenotypes reveal trending and statistically significant decreases (~0.5-fold) in *RBX1*$^{+/-}$-1 and *RBX1*$^{+/-}$-2, respectively, relative to NT-Control clones (***Figure 4-8B***; ***Table S40***). Overall, these data support that SL phenotypes following *PARP1* silencing can be recapitulated using clinically relevant PARP1 inhibitors (*e.g.*, Olaparib), which may ultimately be of therapeutic benefit for HGSOCs exhibiting diminished expression of *RBX1*.

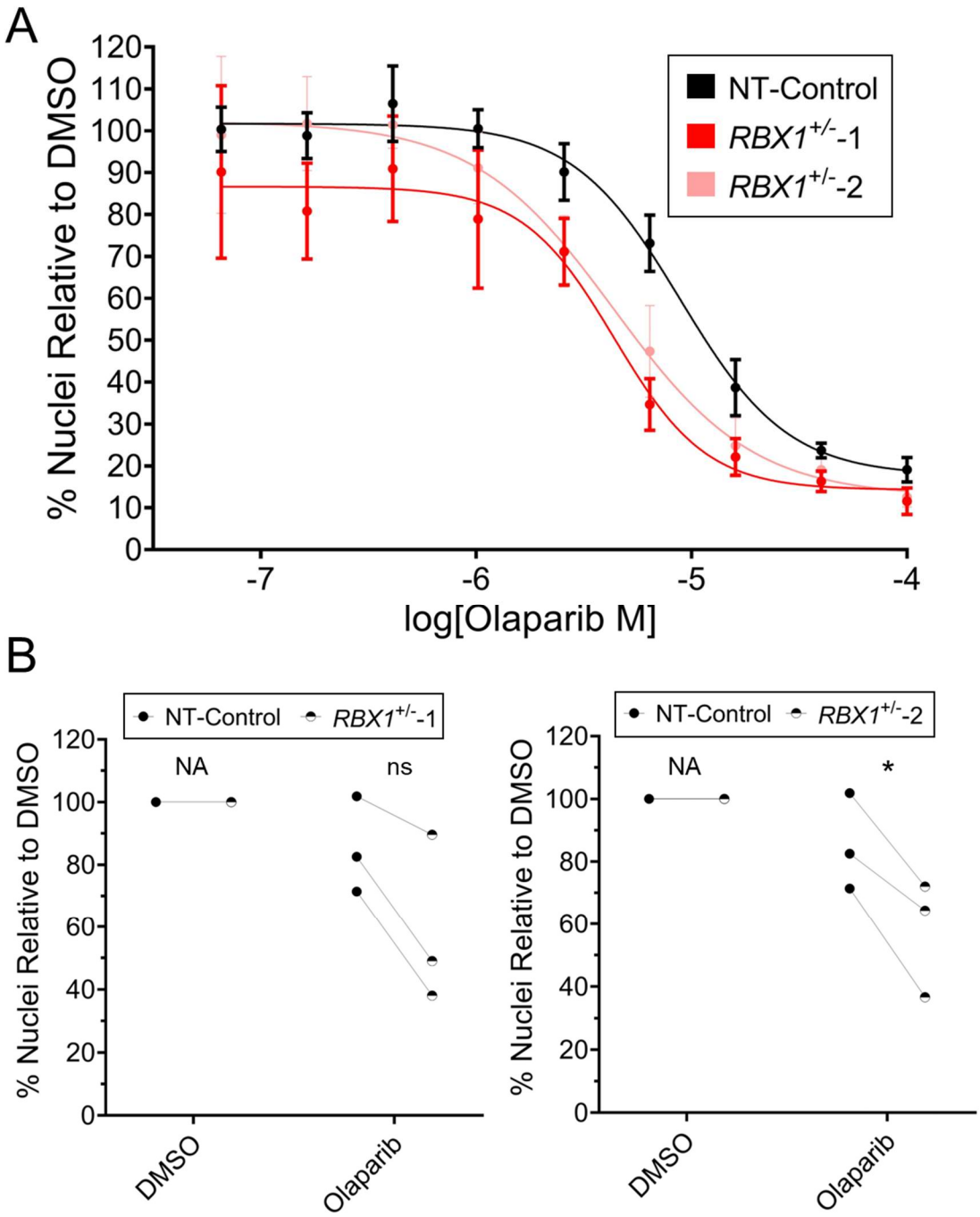

Figure 4-8. PARP1 Inhibition Induces Decreases in Cell Numbers in *RBX1*$^{+/-}$ Clones.
(A) Representative dose response curves (2.5-fold serial dilution) for *RBX1*$^{+/-}$ and NT-control clones treated with Olaparib (PARP1 inhibitor). Data are normalized to the vehicle control and bars represent standard deviation (DMSO; N = 2, n =6). **(B)** Dot plots presenting the mean number of nuclei relative to DMSO following treatment with Olaparib (6.40 µM) within NT-Control and *RBX1*$^{+/-}$ clones. Paired *t*-tests reveal trending and significant decreases in cell numbers within *RBX1*$^{+/-}$ clones following PARP1 inhibition (N=3; n=6; ns=not significant; p-value * ≤ 0.05).

4.2.5 Olaparib induces DNA-Damage in *RBX1*$^{+/-}$ Clones

In HRR-deficient cells, Olaparib induces an accumulation of unrepaired SSBs, which leads to the formation of DSBs that cannot be repaired via the HRR pathway[40]. To assess the prevalence of DNA DSBs within *RBX1*$^{+/-}$ clones following PARP1 inhibition, semi-quantitative IIF was employed to evaluate changes in the global abundance of γ-H2AX (number of IRIF like foci; an established surrogate marker of DNA DSBs)[132]. First, to validate the γ-H2AX antibody, IIF was performed on NT-Control clones, where results show that γ-H2AX foci increased within the Bleomycin-treated samples relative to untreated controls (***Figure 4-9***). Next, semi-quantitative IIF was performed to determine whether treatment with Olaparib preferentially induces DNA DSBs within *RBX1*$^{+/-}$ clones. Results show visual and statistically significant increases in the abundance of γ-H2AX within *RBX1*$^{+/-}$-1 (~4.7-fold mean increase; statistically significant) and *RBX1*$^{+/-}$-2 (~1.7-fold mean increase; statistically significant) following treatment with Olaparib (***Figure 4-10***; ***Table S41***). The NT-Control clones also exhibited significant increases (~1.5-fold) in the abundance of γ-H2AX following treatment with Olaparib relative to DMSO. However, these increases were less pronounced than those observed within the *RBX1*$^{+/-}$ clones, and these lesions likely would have been repaired via HRR had the NT-Control clones been permitted to recover post-treatment, as they are karyotypically stable and are suspected to have an intact HRR pathway (discussed further in ***Section 5.2***). In addition, although the concentration of DMSO employed within the IIF experiments (0.08%) was slightly higher than that employed for the direct SL tests (0.03%), it is not enough to induce significant increases in the abundance of DNA DSBs[136]. Therefore, these data suggest that treatment with Olaparib induces increases of DNA DSBs within *RBX1*$^{+/-}$ clones relative to corresponding controls, which may partially explain their increased sensitivity to PARP1 inhibition.

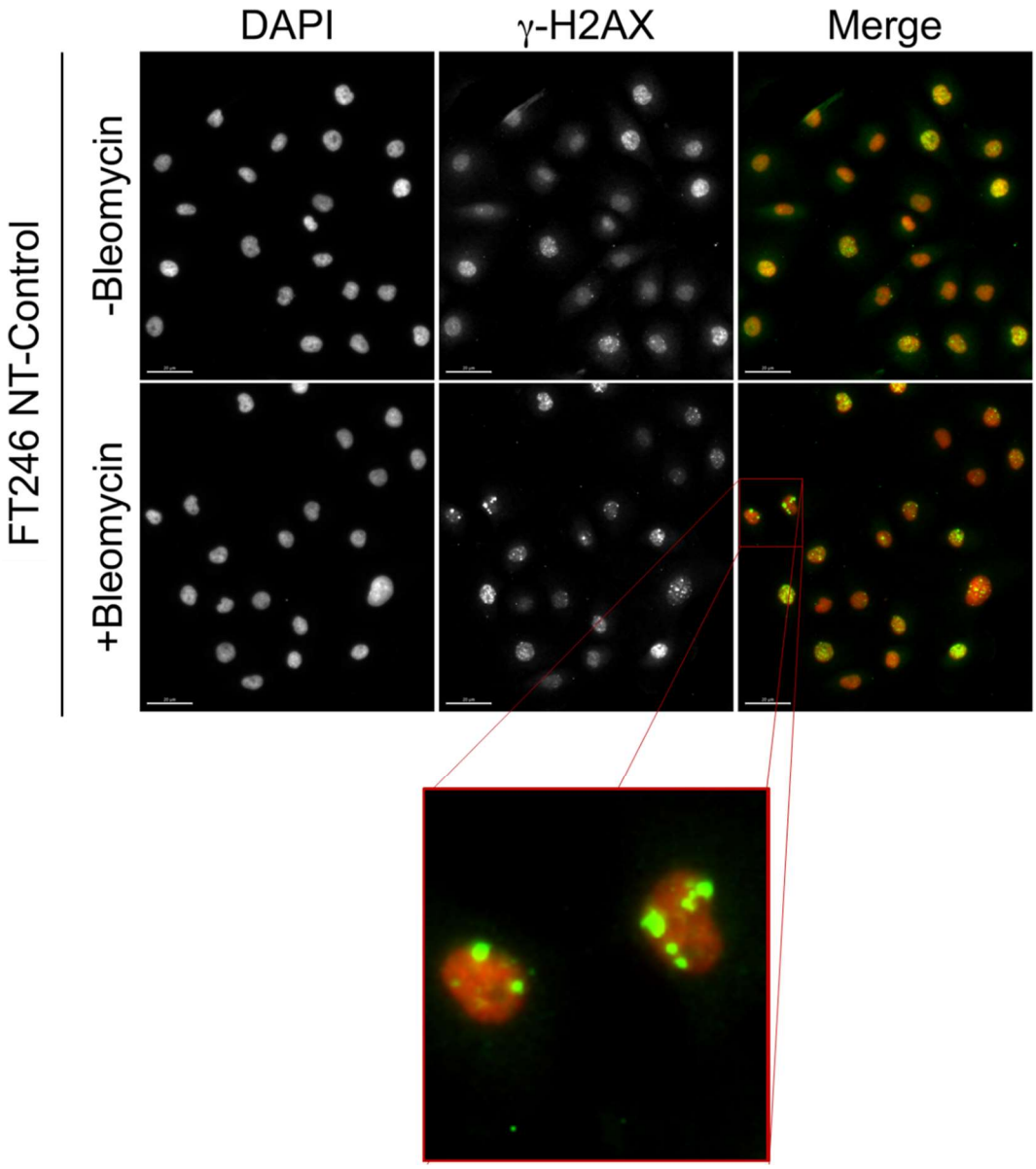

Figure 4-9. Validation of γ-H2AX Antibody within NT-Control Clones.
Representative low-resolution IIF images depicting the localization and abundance of γ-H2AX as reflected by visual increases in the number of IRIF-like foci (bounding box) following treatment with bleomycin relative to untreated controls as a marker of DNA DSBs. DAPI and γ-H2AX are pseudo-colored red and green within the merged image, respectively. Scale bar=20μm.

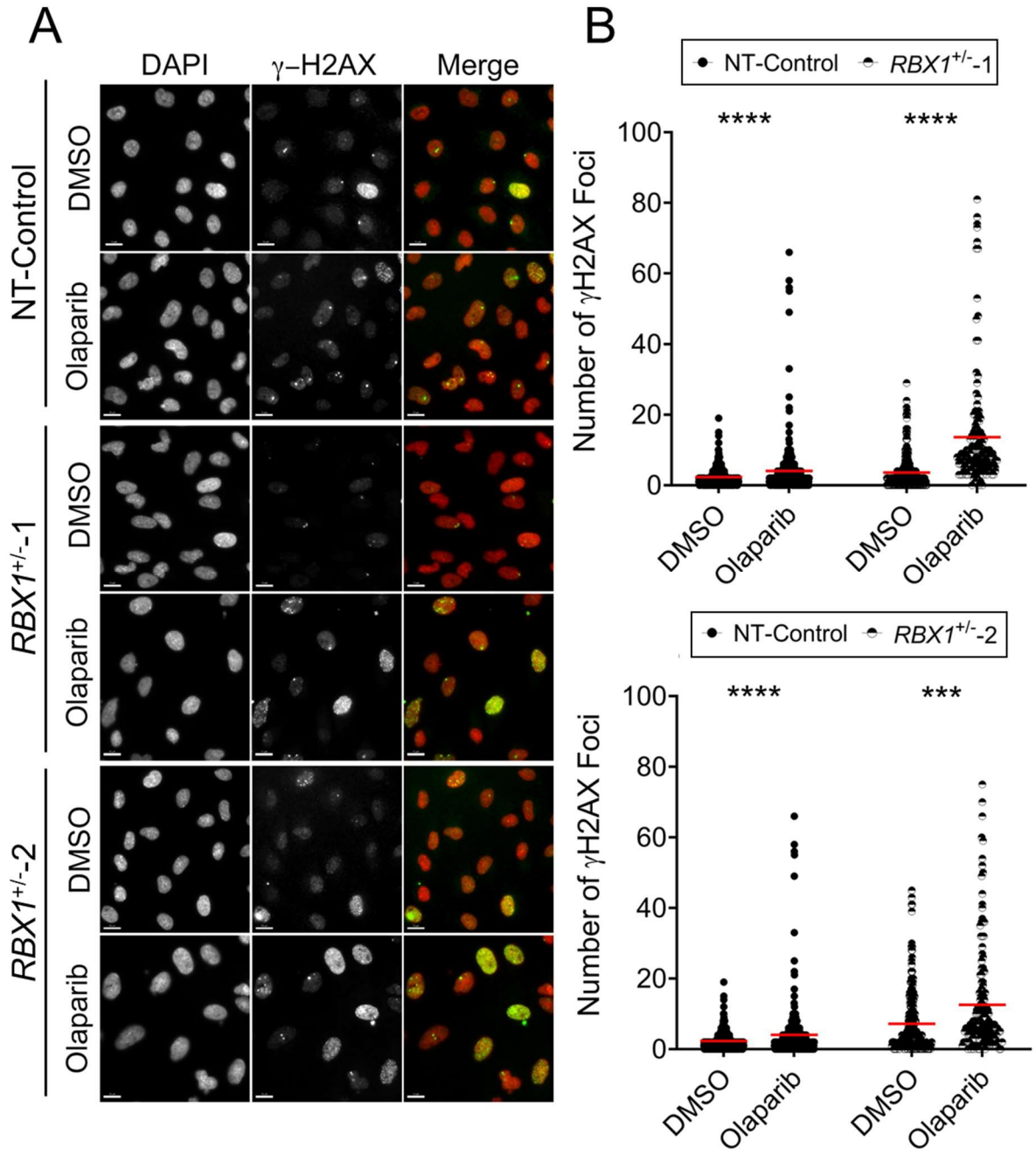

Figure 4-10. PARP1 Inhibition Induces DNA DSBs in *RBX1*$^{+/-}$ Clones.
(A) Representative low-resolution images of γ-H2AX abundance within NT-Control (top), *RBX1*$^{+/-}$-1 (middle) and *RBX1*$^{+/-}$-2 (bottom) treated with DMSO or Olaparib for 48 h. Images were acquired using identical exposure times at each wavelength so that qualitative and quantitative analyses could be performed. Scale bar=15μm. **(B)** Dot plots presenting the number of IRIF-like foci following treatment with Olaparib (6.40 μM) or DMSO within NT-Control and *RBX1*$^{+/-}$ clones. Red bars indicate mean number of foci for each conditon (N=1; n≥125; ns = not significant; *** p-value < 0.001; **** p-value < 0.0001).

4.2.6 *RBX1*$^{+/-}$ Clones are Sensitive to *CDK2* Silencing

To validate siRNAs targeting *CDK2*, western blots and semi-quantitative analyses were performed on *CDK2* silenced NT-Control cells. Data show a reduction in CDK2 levels ranging from ~14 to 1%, with siCDK2-3 and siCDK2-4 exhibiting the greatest reduction in endogenous CDK2 abundance to ~1% relative to the siControl condition (***Figure 4-11A***). Next, siCDK2-3, siCDK2-4 and siCDK2-Pool were employed to assess the reproducibility of SL phenotypes within *RBX1*$^{+/-}$ clones, where results show that CDK2 silencing is associated with visual (***Figure 4-11B***) and quantitative decreases within the *RBX1*$^{+/-}$-1 (~8 to 75% decrease) and *RBX1*$^{+/-}$-2 (~11 to 85% decrease) relative to NT-Control clones (***Figure 4-11C***). It was somewhat surprising that silencing with siCDK2-3 impacted the *RBX1*$^{+/-}$ clones and NT-Control cells in a similar manner, despite achieving efficient *CDK2* knockdown. However, the generation of additional biological replicates are currently ongoing and these unexpected results may be due to off target effects (discussed further in ***Section 5.2.3***). Taken together with the *in silico* data, these results support the possibility that *CDK2* is an evolutionarily conserved SL interactor of the SCF complex.

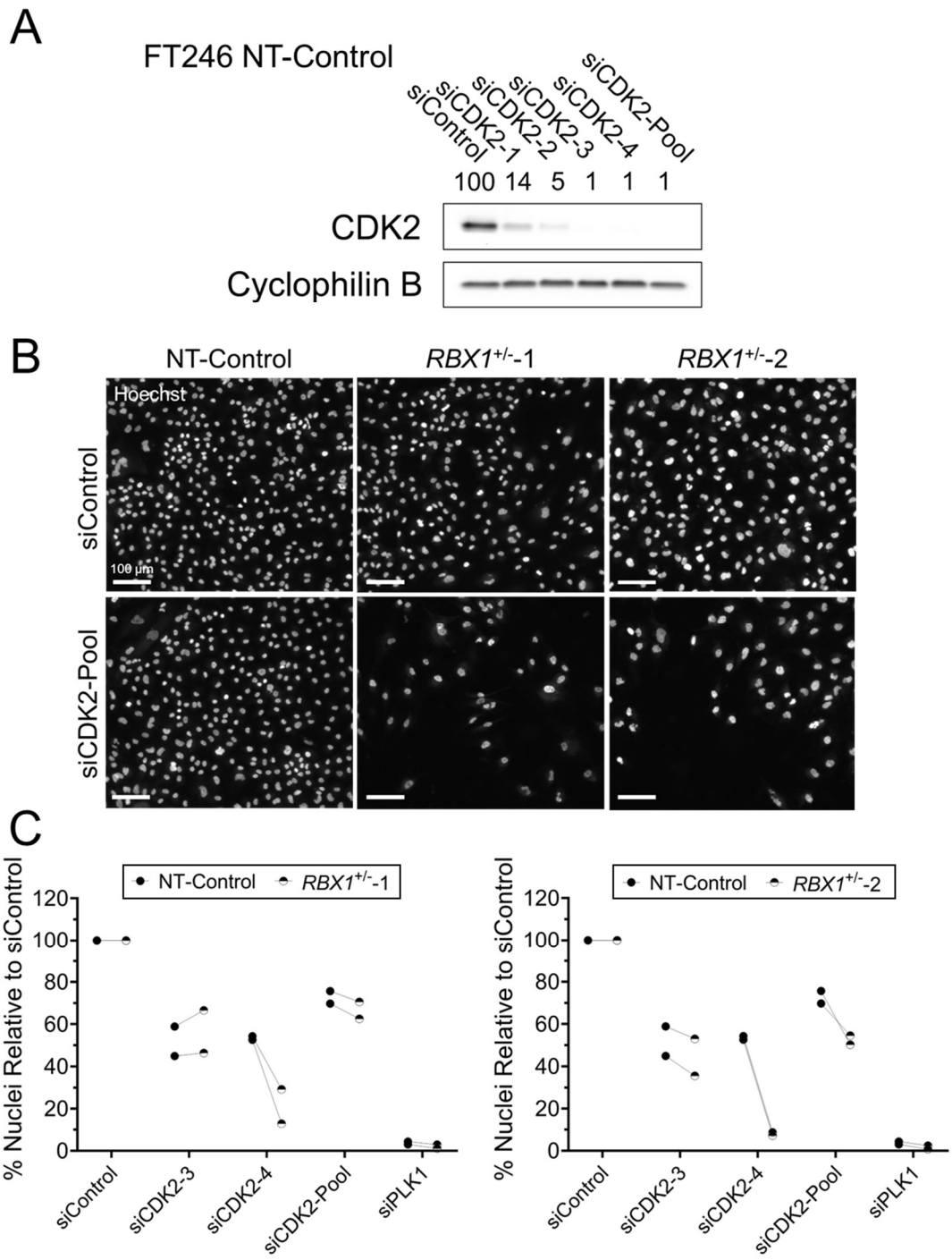

Figure 4-11. *CDK2* may be a Putative SL Interactor of *RBX1*.
(A) Representative western blot depicting endogenous CDK2 abundance in NT-Control cells following *PARP1* silencing; Cyclophilin B is the loading control. **(B)** Low resolution images of NT-Control, *RBX1*$^{+/-}$-1, *RBX1*$^{+/-}$-2 depicting reduced cell numbers following *CDK2* silencing in *RBX1*$^{+/-}$ clones relative to NT-control. **(C)** Dot plots presenting the mean number of nuclei relative to siControl following *CDK2* silencing within NT-Control and *RBX1*$^{+/-}$ clones, revealing trending decreases in cell numbers within *RBX1*$^{+/-}$ clones following *CDK2* silencing (N=2; n=6).

4.2.7 *RBX1*$^{+/-}$ Clones are Hypersensitive to Treatment with SNS-032

To investigate the potential clinical relevance of CDK2 inhibition, dose-response curves (*i.e.*, 5-fold serial dilution) were generated for SNS-032 (CDK2 inhibitor) and DMSO (vehicle control). Data reveal that *RBX1*$^{+/-}$-1 and *RBX1*$^{+/-}$-2 are hypersensitive (~10-fold) to SNS-032 treatments relative to NT-control clones (***Figure 4-12A***), with a calculated EC50 of 0.594 nM, 0.877 nM and 0.322 μM, respectively. As 0.160 μM of SNS-032 induced the greatest SL phenotypes within *RBX1*$^{+/-}$ clones, this concentration was employed to perform additional direct SL tests. Quantification of direct SL tests show that treatment with SNS-032 induces significant and reproducible decreases within *RBX1*$^{+/-}$ clones relative to NT-Control clones (***Figure 4-12B***; ***Table S42***). These results suggest that SL phenotypes following silencing of *CDK2* can be recapitulated using SNS-032 and supports that SNS-032 may be an inhibitor worthy of preclinical study for the treatment of HGSOC patients with diminished *RBX1* expression.

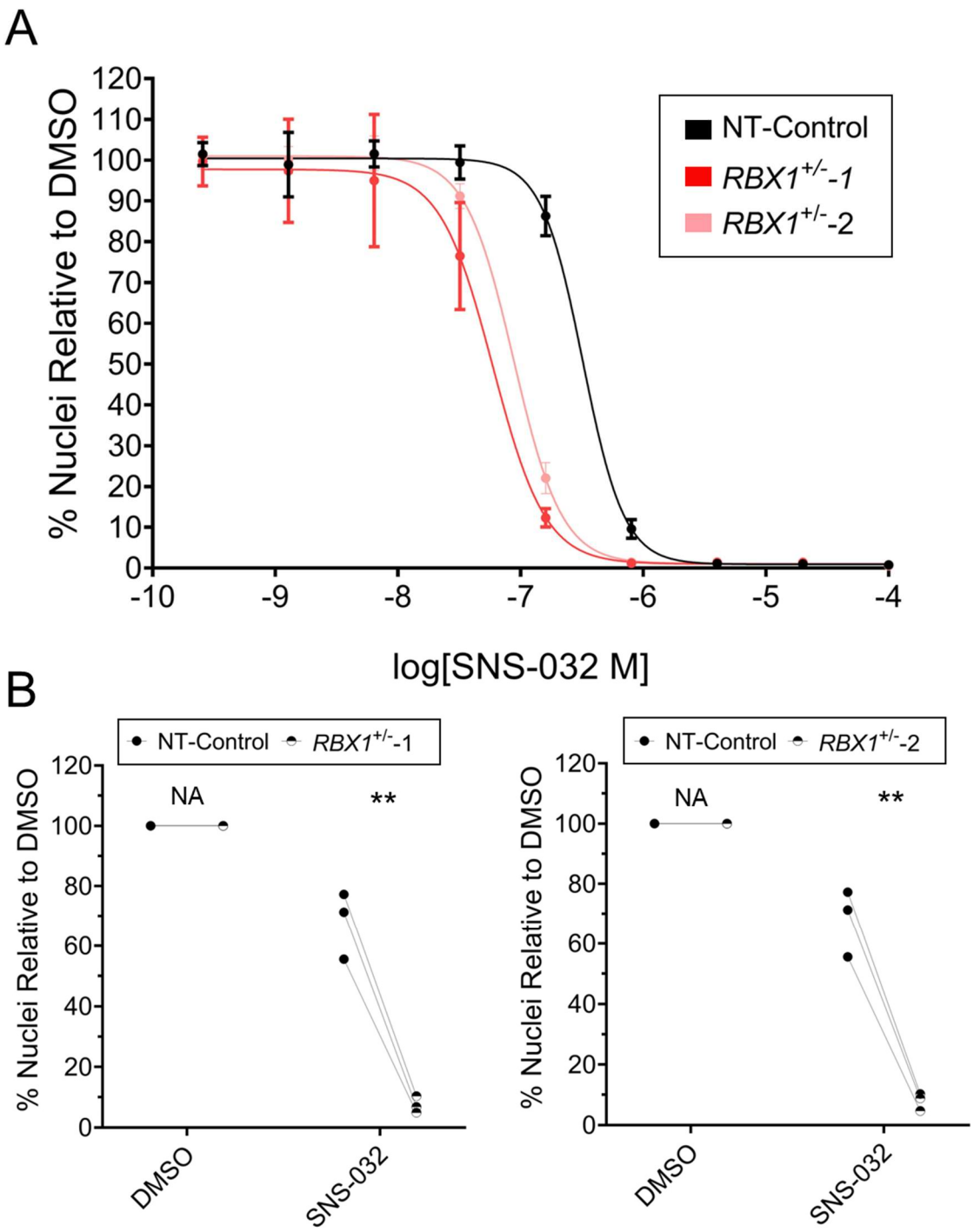

Figure 4-12. CDK2 Inhibition Induces Decreases in Cell Numbers in *RBX1*$^{+/-}$ Clones.
(A) Dose response curves (5-fold serial dilution) for *RBX1*$^{+/-}$ and NT-control clones treated with SNS-032 (CDK2 inhibitor). Data are normalized to the vehicle control and bars represent standard deviation (DMSO; N=2, n=6). **(B)** Dot plots presenting the mean number of nuclei relative to DMSO following treatment with SNS-032 (0.160 µM) within NT-Control and *RBX1*$^{+/-}$ clones. Paired *t*-tests reveal significant decreases in cell numbers in *RBX1*$^{+/-}$ clones following CDK2 inhibition (N=3; n=6; ns = not significant; p-value ** ≤ 0.01).

4.2.8 SNS-032 Induces DNA-damage in *RBX1*$^{+/-}$ Clones

As genetic studies have shown that treatment with SNS-032 induces increases in the abundance of γ-H2AX^{137}, semi-quantitative IIF was performed following treatment with SNS-032 within *RBX1*$^{+/-}$ and NT-Control clones. Results show visual and statistically significant increases in the abundance of γ-H2AX within *RBX1*$^{+/-}$-1 (~3.25-fold mean increase; statistically significant) and *RBX1*$^{+/-}$-2 (~2.67-fold mean increase; statistically significant) relative to NT-Control clones following treatment with SNS-032 (***Figure 4-13***; ***Table S43***). Collectively, these data suggest that treatment with SNS-032 induces overall increases in DNA DSBs within *RBX1*$^{+/-}$ clones relative to corresponding controls, which may contribute to their hypersensitivity to CDK2 inhibition.

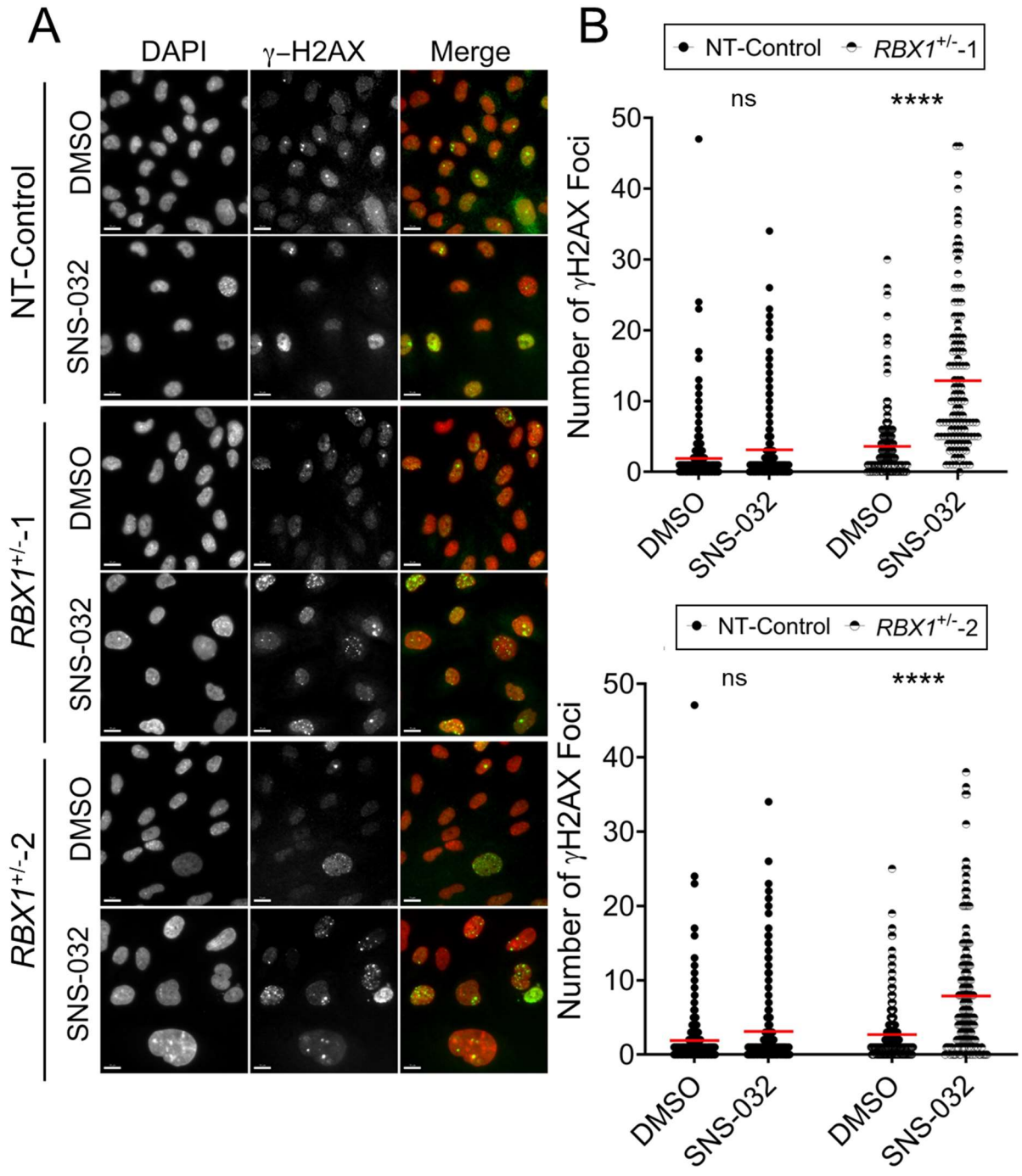

Figure 4-13. CDK2 Inhibition Induces DNA DSBs in *RBX1*$^{+/-}$ Clones.
(A) Representative low-resolution images of γ-H2AX abundance within NT-Control (top), *RBX1*$^{+/-}$-1 (middle) and *RBX1*$^{+/-}$-2 (bottom) treated with DMSO or SNS-032 for 48 h. Scale bars=15 µm. **(B)** Dot plots presenting the number of IRIF-like foci following treatment with SNS-032 (0.160 µM) or DMSO within NT-Control and *RBX1*$^{+/-}$ clones. Red bars indicate mean number of foci per condion (N=1; n=100; ns=not significant; **** p-value < 0.0001).

CHAPTER 5. SUMMARY, DISCUSSION, CONCLUSIONS & SIGNIFICANCE

5.1 SUMMARY

In this study, SL approaches were employed to identify SL interactors (*i.e.*, novel drug targets) of *SKP1*, *CUL1* and *RBX1*. In *Aim 1*, *in silico* and siRNA-based approaches were employed within clinically relevant *SKP1*, *CUL1* and *RBX1* heterozygous knockout clones that were previously generated in FT secretory epithelial cell lines (CRISPR/Cas9). *In silico* approaches were employed to mine the SynLethDB to identify putative SL interactors of the SCF complex from model organisms, while siRNA-based approaches were combined with quantitative imaging microscopy to screen 239 genes encoding functions within the DDR pathways (*i.e.*, the DDR library). Collectively, both approaches identified 228 putative SL interactors, of which *PARP1* and *CDK2* were selected for subsequent validation within $RBX1^{+/-}$ clones. In *Aim 2*, direct SL tests were performed using siRNAs and small molecule inhibitors targeting *PARP1* or *CDK2* to assess the reproducibility of SL phenotypes within $RBX1^{+/-}$ clones. Treatment with siRNAs, Olaparib (PARP1 inhibitor) and SNS-032 (CDK2 inhibitor) resulted in trending and significant decreases within the number of $RBX1^{+/-}$ clones relative to NT-Control clones. In addition, treatment with Olaparib or SNS-032 induced significant increases in γ-H2AX foci in $RBX1^{+/-}$ clones, suggesting an accumulation of DNA DSBs may contribute to the SL phenotypes. Collectively, the findings from this study support *PARP1* and *CDK2* being novel SL interactors of *RBX1*.

5.2 DISCUSSION

5.2.1 The Magnitude of SL Phenotypes in $RBX1^{+/-}$ Clones may be Exacerbated by the Aberrant Function of Multiple E3 Ligases

Protein ubiquitylation plays an important role in cell biology, as it regulates the stability, localization and activity of key substrates involved in a diverse array of essential biological processes[71,72,82,95]. It is well established that the SCF complex has important roles in maintaining genome stability[55-60], the DDR[138,139] and the cell cycle[72,74,140] (detailed further in ***Section 1.3***). Genetic studies have shown that core SCF complex member genes frequently harbour shallow deletions in a variety of cancer types and are thus of tremendous clinical interest for the development of novel precision medicine strategies, including SL-based approaches[17,54]. In the context of the current study, heterozygous loss of *RBX1* is the most clinically relevant genetic

alteration of the core SCF complex member genes, as it occurs in ~81% of ovarian cancers[15,96]. Therefore, to maximize clinical potential, most of the SL assays were performed within clinically relevant FT cell lines exhibiting diminished *RBX1* expression.

Beyond the clinical relevance of *RBX1* alterations in cancer, the results from the siRNA-based screen of the DDR library (*Aim 1*) revealed that the *RBX1*$^{+/-}$ clones generally exhibited enhanced SL phenotypes relative to the *SKP1*$^{+/-}$ and *CUL1*$^{+/-}$ clones. These results were somewhat surprising, as *SKP1*, *CUL1* and *RBX1* have each been identified as novel CIN genes in HGSOC contexts[56,57]. It is conceivable however, that the observed differences in the strength of the SL phenotypes observed between the various heterozygous knockout clones may reflect the functional importance of RBX1 in regulating a wider array of essential biological processes (*e.g.*, genome stability) relative to SKP1 and CUL1. For example, while *SKP1*, *CUL1* and *RBX1* are proposed to be essential genes[83,141,142] whose diminished expression induces CIN[56,57], only diminished *RBX1* expression was demonstrated to promote cellular transformation phenotypes in HGSOC contexts[56]. While the exact molecular mechanisms underlying these differences have yet to be determined, these findings suggest that diminished *RBX1* expression may have greater pathogenic implications relative to diminished *SKP1* or *CUL1* expression. Biochemical studies have shown that other cullin proteins, such as Cullin 7 (CUL7), can functionally compensate for CUL1 within the SCF complex, as they harbour similar binding motifs and overlapping functions[143], which may prevent or limit the SL phenotypes following DDR gene silencing within *CUL1*$^{+/-}$ clones[57]. In contrast, although a closely related member to RBX1 has been identified, namely RBX2, they are functionally distinct and RBX2 is reported to regulate distinct protein substrates[144,145]. For example, RBX2 predominantly interacts with Cullin 5 (CUL5) and is suspected to regulate a smaller subset of protein targets, whereas RBX1 interacts with all 7 members of the cullin protein family and consequently, is expected to regulate a larger number of targets[84,146,147]. Furthermore, the primary function of SKP1 is to function as an adaptor for the SCF complex[55,57,59], whereas RBX1 functions as a core member within several E3 ligases (detailed below)[148], including the KEAP1-CUL3-RBX1 complex[90] and the DDB2-RBX1-CUL4A/4B complex[149] (***Figure 5-1***), and thus, is involved in the ubiquitination of many additional protein targets relative to SKP1. Collectively, these functional differences between core SCF complex members support the possibility that diminished *RBX1* expression may adversely impact the regulation of a broader range of protein targets and biological pathways

relative to *SKP1* and *CUL1*, which may account for the stronger SL phenotypes observed in our screen.

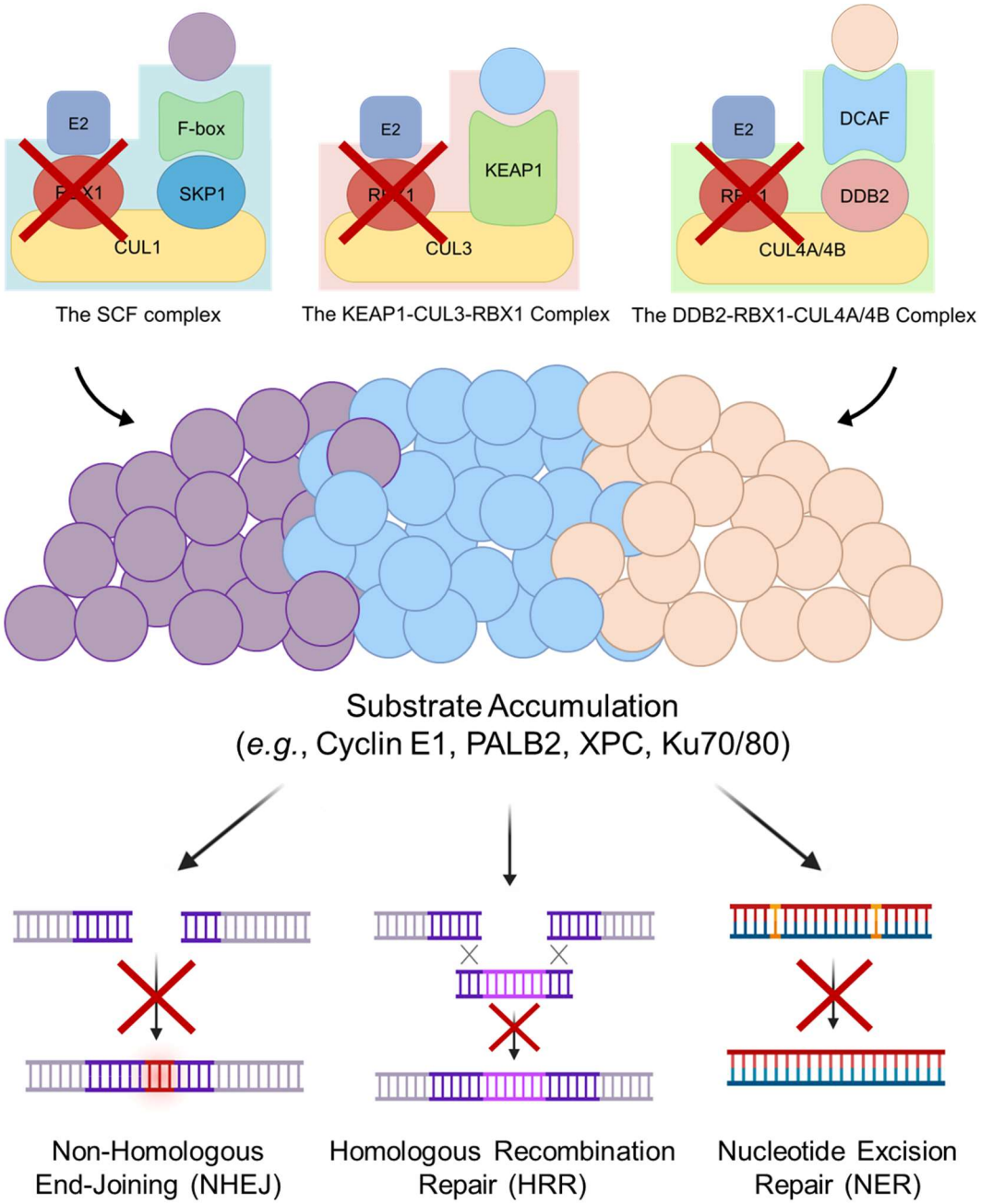

Figure 5-1. Aberrant *RBX1* Expression May Adversely Impact the Formation and Function of Multiple E3 Ubiuqitin Ligases.
Schematic illustrating the suspected impact that diminished *RBX1* expression may have on the formation and function of three E3 ligases. The aberrant function of these E3 ligases and subsequent misregulation of their respective and/or shared protein targets may induce defects in essential biological pathways to induce enhanced SL interactions relative to the other core SCF complex members (SKP1 and CUL1).

The KEAP1-CUL3-RBX1 complex (***Figure 5-1***) is an E3 ligase comprised of KEAP1, CUL3 and RBX1, and is a well-known regulator of the Nuclear factor erythroid 2-related factor 2 (NRF2)-mediated antioxidant response and the DDR[90,150]. Briefly, the KEAP1-CUL3-RBX1 complex has been implicated in HRR as a regulator of PALB2 (see ***Section 1.3.3***) and FANCD2[90,148]. The monoubiquitylation of FANCD2 during HRR enables the formation of the FANCD2-FANCI complex, which regulates the recruitment of other essential members of the HRR pathway to DSBs, including BRCA1/2, PALB2 and RAD51[150]. Another E3 ligase in which RBX1 is a core member is the DDB2-RBX1-CUL4A/4B complex, which is comprised of DDB2 (DNA damage-binding protein 2), Cullin 4A/4B (CUL4A/CUL4B) and RBX1 (***Figure 5-1***)[80,151]. The DDB2-RBX1-CUL4A/4B complex regulates a variety of proteins involved in chromatin formation (histones H2A, H3 and H4), DNA replication (Chromatin licensing and DNA replication factor 1; CTD1) and the DDR (XPC)[80,148]. Interestingly, several putative targets of the DDB2-RBX1-CUL4A/4B complex are also suspected to be regulated by the SCF complex, including N-Myc and Cyclin E1[75,120,148,151]. Within the DDR, the DDB2-RBX1-CUL4A/4B complex is a key regulator of the nucleotide excision repair (NER) pathway[151], a multi-step DNA repair pathway that functions to remove bulky DNA lesions that commonly arise from environmental mutagens or ultraviolet (UV) light (reviewed by Schärer *et al.*[152]). During NER, UV-induced DNA lesions are removed by a process that involves the poly-ubiquitylation of XPC, DDB2 and histones H2A, H3, and H4 by the DDB2-RBX1-CUL4A/4B complex[139,149].

Diminished *RBX1* expression is suspected to impair SCF complex formation and function, leading to the aberrant accumulation of oncogenic protein targets such as Cyclin E1 that induces CIN and promotes cellular transformation[56]. In a similar manner, diminished *RBX1* expression may also impair the formation and function of other E3 ligases (***Figure 5-1***), inducing defects in DDR pathways like HRR and NER through aberrant substrate regulation. Therefore, while additional functional studies are warranted, it would be reasonable to suggest that cells harbouring diminished *RBX1* expression may exhibit enhanced SL interactions due to the simultaneous disruption of multiple E3 ligases. As SL interactors often encode functions within the same and/or parallel biological pathways[54], the aberrant function of multiple E3 ligases and subsequent misregulation of their respective (*e.g.*, PALB2) and/or shared (*e.g.*, Cyclin E1) protein targets may induce defects in essential biological pathways in a manner that is incompatible with viability.

5.2.2 Exploring Aberrant *RBX1* Expression in Olaparib-responsive, non-*BRAC1/2* Mutated Ovarian Cancer Patients

PARP1 is a well-established drug target and multifunctional protein involved in a wide range of cellular processes, including transcriptional regulation, genome stability and the DDR[153]. *PARP1* spans 35 kb genomic DNA, localizes to 1q42.12 and encodes a protein with a molecular mass of ~116 kDa[77]. Within the DDR, PARP1 is a regulator within the NHEJ, HRR and BER pathways, with its foremost function being to facilitate the repair of DNA SSB via BER[116]. PARP1 functions as a DNA damage sensor within the BER pathway that is rapidly recruited to DNA SSB, where it utilizes nicotinamide adenine dinucleotide (NAD+) as a substrate to catalyze the addition of poly-ADP-ribose (PAR) onto itself and acceptor proteins[43,116]. This post-translational modification process, termed PARylation, facilitates the recruitment of chromatin remodeling complexes and additional members of the DDR to repair SSBs[154]. Accordingly, PARP1 knock-down or inhibition induces defects within the BER pathway, leading to the accumulation of unrepaired SSBs[116]. These SSBs can be subsequently converted to DSBs over time, necessitating repair through the HRR pathway to maintain genome stability[111,154]. This theoretical concept laid the foundation for the SL studies conducted by Bryant[110] and Farmer[111] who determined that BRCA1/2-defective (HRR-deficient) cells exposed to *PARP1* silencing or inhibition are unable to repair these SSBs and ensuing DSBs effectively, leading to an accumulation of DSBs that induces apoptotic cell death.

When Olaparib was initially translated into the clinic, it was indicated for the treatment of hereditary breast and ovarian cancer patients harbouring germline mutations in *BRCA1/2*, as the underlying mechanism suggested that only tumors classified as HRR-deficient would respond effectively to PARP1 inhibitors[43]. Since then, three additional PARP1 inhibitors have been FDA-approved, including Rucaparib (2016; Clovis Oncology, Inc.), Niraparib (2017; Tesaro, Inc.) and Talazoparib (2018; Pfizer), and the eligibility criteria for treatment expanded to individuals exhibiting platinum-sensitivity, high-levels of genome instability and HRR-deficiency[153]. Although genes such as *BRCA1/2* and *RAD51* are commonly assessed, there is currently no precise definition or consensus on what classifies an individual as HRR-deficient and emerging clinical and functional data now strongly suggest there are many additional genetic alterations (*i.e.*, therapeutic biomarkers) that may confer therapeutic benefit to treatment with PARP1 inhibitors[153,155]. In fact, numerous clinical studies have shown that PARP1 inhibitors are able to

confer therapeutic benefit to a much broader spectrum of patients, including individuals traditionally deemed HRR-proficient[155-158]. For example, an *in vitro* study conducted by Keung *et al.*[158] determined that various breast cancer cells exhibited sensitivity to a variety of PARP1 inhibitors, including Olaparib, Rucaparib and Niraparib, regardless of *BRCA1/2* status. These results are consistent with those from other clinical studies showing that treatment with Niraparib can significantly improve clinical outcomes within HRR-proficient ovarian cancer patients and suggest that additional genes and/or pathways may be contributing to the success of PARP1 inhibitors within HRR-proficient cancers[156]. These findings further suggest that the observed therapeutic effects may not be limited to a particular PARP1 inhibitor, despite the fact that many PARP1 inhibitors frequently exhibit slight differences in their pharmacological characteristics and thus exert varying therapeutic effects[159]. As such, elucidating the additional molecular mechanisms underlying the anti-tumor effects of PARP1 inhibitors is essential for optimizing treatment strategies and improving patient outcomes, as it may identify novel therapeutic biomarkers for the development of precision medicine strategies. One of the major clinical benefits of employing SL-based approaches is the ability to utilize the genetic alterations harboured by the tumor as a means of guiding treatment decisions for targeted chemotherapeutic strategies[54,103,123]. It well-established that PARP1 inhibitors induce synthetic lethality within HRR-deficient cells by inducing defects in another essential DNA repair pathway (*i.e.*, BER)[43,117,123,154]. However, there is currently no consensus on what classifies an individual as HRR-deficient and the molecular mechanisms underlying the therapeutic effects within patients classified as HRR-proficient are not well understood[153].

Within the current study, *PARP1* was identified as a putative SL interactor of the SCF complex through *in silico* approaches and within the siRNA-based screen of the DDR library and was further prioritized due to its established clinical relevance in the treatment of HGSOC[43]. The direct SL tests performed in *Aim 2* revealed that *PARP1* silencing is associated with variable, yet trending decreases in the number of *RBX1*$^{+/-}$ clones relative to controls (see ***Section 4.2.3***). Although *PARP1* silencing did not induce statistically significant decreases in the number of *RBX1*$^{+/-}$ clones within most silencing conditions, the variability between SL phenotypes may be due to the genetic heterogeneity contained within the *RBX1*$^{+/-}$ clonal populations. SL studies traditionally employ homozygous knockout models to identify novel SL interactors, as it helps minimize the possibility of compensatory mechanisms, thus increasing the reproducibility of

observed SL phenotypes. In contrast, the *RBX1*$^{+/-}$ clones have reduced *RBX1* expression (*i.e.*, reduced functionality), are karyotypically unstable and exhibit ongoing CIN that drives genetic and cell-to-cell heterogeneity[56]. These genetic differences may lead to compensatory mechanisms through the remaining wild-type *RBX1* allele and/or cause gains or losses of key genes that could potentially mitigate or supress the impact of *PARP1* silencing, leading to variable SL phenotypes between biological replicates. In addition, this phenotypic variation may be somewhat reflective of the technical limitations that are associated with using siRNA-based approaches relative to small molecule inhibitors. Briefly, siRNA transfection efficiencies can vary between individual cells[160], leading to differences in knock-down efficiencies that are undetectable via conventional western blots that present a population average. In contrast, cells typically receive the same dose of a given small molecule inhibitor in any given experiment. These differences may partially explain why the observed SL phenotypes within *RBX1*$^{+/-}$ clones following treatment with Olaparib were more consistent and pronounced than those performed using siRNA-based approaches. Indeed, Olaparib treatments induced trending and statistically significant decreases within *RBX1*$^{+/-}$-1 and *RBX1*$^{+/-}$-2, respectively, reducing the number of *RBX1*$^{+/-}$ clones to ~70% of the NT-Control clones in almost all biological replicates (see ***Section 4.2.4***). Therefore, while additional research is required, these results support the possibility that *PARP1* is a novel SL interactor of *RBX1* and highlight the potential clinical utility of Olaparib for the treatment of *RBX1*$^{+/-}$ HGSOCs.

Previous pharmacological studies have established that PARP1 inhibitors exert their anti-tumor effects by interacting with the active site of PARP1 to block NAD+ binding and enzymatic activity, consequently "trapping" the PARP1-chromatin complex at SSB sites to prevent effective repair[161]. The resulting inhibitor-PARP1-DNA complexes interfere with DNA replication by destabilizing replication forks leading to replication fork collapse that induces genome instability and cell death[110,162]. As discussed in ***Section 5.2.1***, decreased *RBX1* expression is suspected to impair the formation and function of at least three E3 ligases, leading to the misregulation of numerous protein targets, such as PALB2, which may adversely impact numerous biological processes, including HRR[56,76,90,149]. Synthetic genetic studies have shown that clinically actionable SL interactions are often be found upstream or downstream established SL gene pairs (*e.g.*, *PARP1* and *BRCA1/2*) and frequently encode functions within the same biological pathway. For example, *PALB2* was identified as a SL interactor of *PARP1*, after an *in*

vitro study by Buisson *et al.*[163] demonstrated that *PALB2*-deficient cells could be selectively targeted using Olaparib relative to those with harbouring wild-type *PALB2* expression. Therefore, as effective HRR is dependant upon the ubiquitination of PALB2 by the KEAP1-CUL3-RBX1 E3 ligase, treatment with Olaparib may induce selective decreases within *RBX1*$^{+/-}$ clones in a similar manner to cells exhibiting diminished *PALB2* expression. Another factor that must be considered is that although CIN is suspected to drive cancer pathogenesis by inducing gains and losses of key genes that promote cell survival and growth, genetic studies suggest that cells exhibiting CIN also may have an intrinsic threshold or a "CIN threshold", where levels beyond this threshold become lethal[164,165]. As PARP1 inhibition induces high levels of genome instability[39,154,155,166], an additional mechanism that may be contributing to the SL phenotypes observed within the current study may be that treatment with Olaparib exacerbates the existing levels of CIN within the *RBX1*$^{+/-}$ clones that propels cells past this threshold to induce cell death (***Figure 5-2***)[164,165]. In either case, additional research is required before we can elucidate the molecular mechanisms underlying the SL phenotypes within *RBX1*$^{+/-}$ clones following Olaparib treatments. Taken together, the data presented in this thesis shed novel insight into why certain cancers may benefit from treatment with PARP1 inhibitors, regardless of their HRR status and identify *PARP1* as a novel SL interactor of *RBX1*. Moreover, these findings highlight the potential clinical utility of utilizing *RBX1* as a therapeutic biomarker within HGSOC patients that would otherwise be classified as HRR-proficient, which may broaden the clinical benefit of PARP1 inhibitors by making them accessible to a wider patient population.

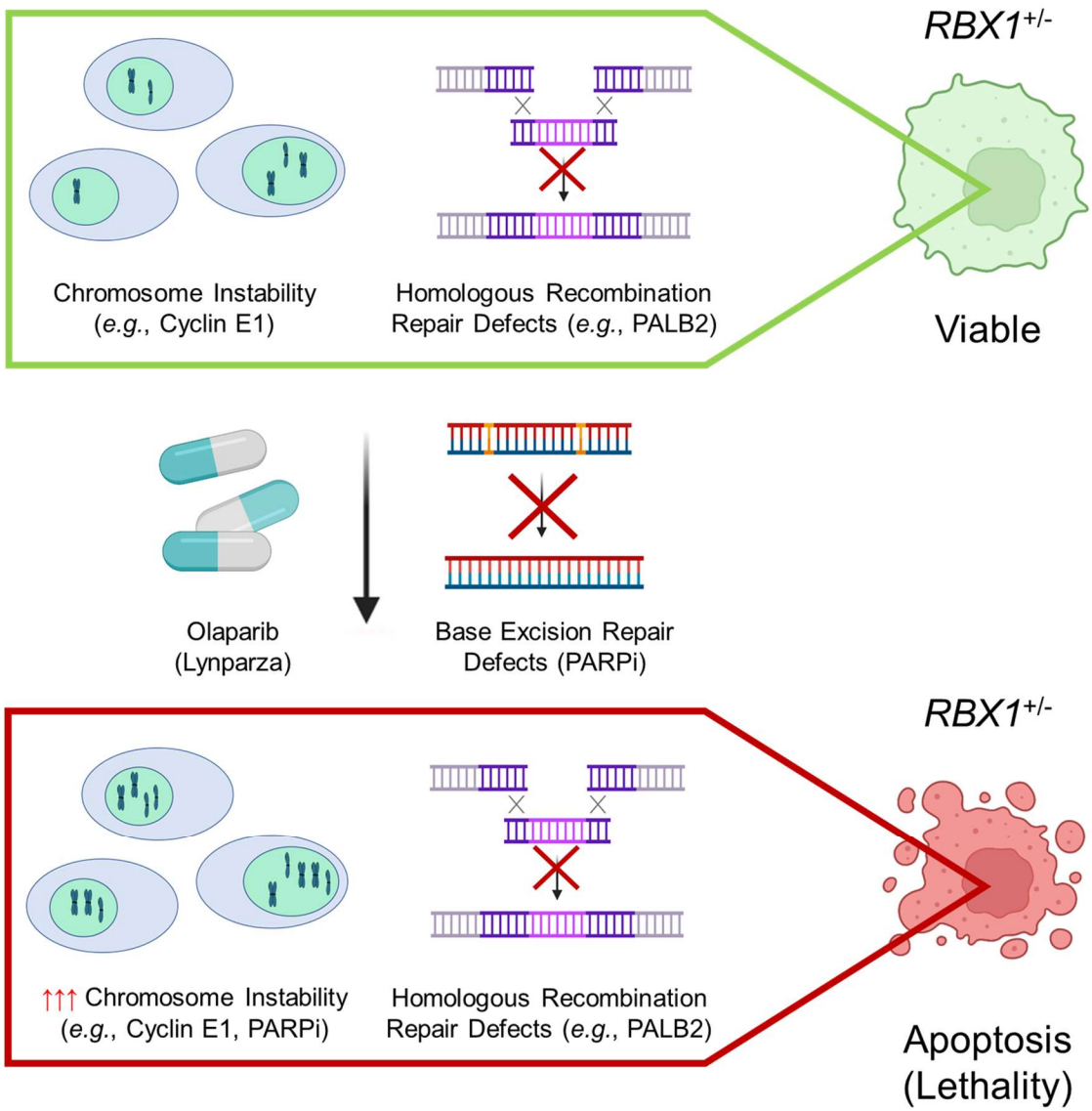

Figure 5-2. Olaparib Preferentially Targets *RBX1*$^{+/-}$ Clones.
Schematic illustrating the suspected molecular mechanism underlying selective decreases in *RBX1*$^{+/-}$ clones following Olaparib treatment. *RBX1*$^{+/-}$ clones exhibit CIN and defects in HRR due to the aberrant accumulation of substrate targets (*e.g.*, PALB2). Olaparib treatment inhibits PARP1, which exacerbates pre-existing genome instability and induces defects in BER that cannot be repaired by HRR that results in cell death via apoptosis.

5.2.3 Enhanced SL Phenotypes within *RBX1*$^{+/-}$ Clones following Silencing or Inhibition of CDK2 may be due to the Ablation of Multiple Biological Pathways

CDK2 is a serine/threonine kinase and a well-established regulator of the cell cycle that interacts with Cyclin E1 to promote the G1/S-phase transition to promote DNA replication[77]. *CDK2* spans 6 kb of genomic DNA, localizes to 12q13.2 and encodes a 298 aa protein with a mass of ~33 kDa[77]. Briefly, Cyclin E1 is expressed at low levels during the G1 phase of the cell

cycle, and it is the accumulation of Cyclin E1 that triggers binding to CDK2 to form a stable complex, leading to CDK2 activation[167]. The activated Cyclin E1-CDK2 complex phosphorylates retinoblastoma protein (Rb) to induce the release of E2F transcription factors that promote the expression of genes required for entry into S-phase and DNA replication[167]. To ensure proper control of the cell cycle, this process is regulated by negative feedback loops that modulate the Cyclin E1-CDK2 complex[167]. Contrastingly, aberrantly high levels of Cyclin E1 leads to dysregulated cell cycle control, resulting in uncontrolled cell proliferation and increased genome instability[167]. Therefore, it is perhaps unsurprising that genomic amplification of the Cyclin E1 gene and increased abundance is associated with tumor progression and poor prognosis in ovarian cancer[168]. Despite Cyclin E1 gene amplification occurring in up to 20% of ovarian cancer cases, increased Cyclin E1 protein levels are present in ~50% of HGSOCs and are suspected to arise, at least in part, by its misregulation by the ubiquitin proteosome system[11,56,57]. Indeed, genetic studies have shown that decreased expression of each core SCF complex member is associated with increases in Cyclin E1 abundance that is suspected to induce CIN and contribute to HGSOC pathogenesis (detailed further in ***Section 1.3***)[56,57]. However, Cyclin E1 lacks enzymatic activity (*i.e.*, it cannot be directly inhibited) and is therefore more difficult to therapeutically target compared to a traditional enzyme[169]. Clinical studies have shown that ovarian cancer cells harbouring increased expression levels of Cyclin E1 exhibit greater CDK2 activity and thus may exhibit enhanced sensitivity to CDK2 knock-down or inhibition[170]. Moreover, while most non-malignant cells harbour low CDK2 expression levels, it is frequently upregulated in many cancer types and has therefore become of interest as a candidate drug target[170].

Within the current study, *CDK2* was identified as a putative SL interactor of *RBX1* using *in silico* approaches[133] and was further prioritized as *CDK2* is a SL interactor of *CUL1* in *S. cerevisiae*[129]. As genetic studies have shown that SL interactions can be evolutionarily conserved[106,171] and both *CUL1* and *RBX1* encode invariable core members of the SCF complex[17,56,60,72,89], it is reasonable to posit that *CDK2* may also be a SL interactor of *RBX1*. The direct SL tests performed in *Aim 2* revealed that *CDK2* silencing is associated with overall decreases in the number of $RBX1^{+/-}$ clones relative to controls, except for siCDK2-3, that seemed to impact both the NT-Control and $RBX1^{+/-}$ clones in a similar manner (see ***Section 4.2.6***). Biochemical studies have shown that while multiple siRNAs may achieve comparable

knockdown efficiencies of a gene of interest, off-target effects may result in variable cellular responses[172]. Therefore, the lack of SL phenotype within *RBX1*$^{+/-}$ clones following silencing with siCDK2-3 may be the result of an off-target effect.

To confirm on-target specificity, additional chemo-genetic SL tests were performed using SNS-032, a CDK2 inhibitor. SNS-032 is 10- and 20-fold more selective toward CDK2 than CDK1 and CDK4, respectively, and is suspected to exert its anti-tumor effects by inducing apoptosis[173]. Excitingly, treatment with SNS-032 effectively reduced the number of *RBX1*$^{+/-}$ clones to ~10% of the NT-Control clones, supporting its potential clinical utility for the treatment of HGSOCs with diminished *RBX1* expression. It is important to note that while SNS-032 is a selective inhibitor of CDK2, it also impacts CDK7 and CDK9[170]. So, while the promiscuity associated with many CDK inhibitors may render them challenging to integrate within clinical settings due to the non-specific targeting effects, certain cancers may benefit from this promiscuity[174]. For example, tumors harbouring *CCNE1* amplifications and CDK2 dependencies may benefit from a CDK2/CDK7 inhibitor, as CDK7 inhibition prevents the activation of residual CDK2[174]. This possibility is consistent with results of Yang *et al.*[170] who assessed the efficacy of SNS-032 in ovarian cancer contexts and determined that *CCNE1* over-expressing cell lines are 40-fold more sensitive to treatment with SNS-032, inducing significant increases in number of apoptotic cells relative to those without *CCNE1* overexpression. As decreased *RBX1* expression induces increases in Cyclin E1 abundance[56], the findings in the Yang study are consistent with those from this thesis that show that *RBX1*$^{+/-}$ clones can be selectively targeted using SNS-032. Accordingly, our data identify a potential clinical utility for the treatment of HGSOCs harbouring similar genetic alterations, although further pre-clinical studies are highly warranted.

It is also worth noting that although no CDK2-specific inhibitors were available prior to the commencement of this study, the development of new and more selective CDK2 inhibitors (*e.g.*, BLU-222) is underway. The VELA study is a Phase I/II clinical trail aimed at assessing the clinical utility of BLU-222 for the treatment of advanced solid tumors, including *HER2*-negative breast cancers, ovarian cancers and cancers harbouring *CCNE1* amplifications[175]. While this clinical trail is ongoing, recent data from an *in vitro* study conducted by Brown *et al.*[176] show that BLU-222 exhibits increased selectivity toward CDK2 relative to other CDK family members, including CDK1, -4, -6, -7, and -9, and that ovarian cancer cell lines harbouring

CCNE1 amplifications exhibit increased sensitivity to BLU-222 relative to those with normal *CCNE1* expression. Collectively, these findings support further studies involving emerging CDK2 inhibitors, such as BLU-222, to determine their potential clinical utility in the treatment of cancers harboring increased Cyclin E1 abundance, which includes *RBX1*$^{+/-}$ HGSOCs.

As stated above, decreased *RBX1* expression is suspected to impact a broad range of target substrates as it potentially impacts multiple E3 ligases, including the SCF complex[56,90,149]. These genetic alterations may cause aberrant turnover of key protein targets and adversely impact the biological processes in which they function such as the cell cycle (N-Myc[75,120] and Cyclin E1[55,57,167,168,177]), HRR (PALB2[90-92]) and NER (XPC[148]). Thus, it is reasonable to suggest that *CDK2* silencing, or inhibition may induce selective decreases in the number *RBX1*$^{+/-}$ clones due to the ablation of multiple essential biological pathways. Although CDK2 is well-characterized for its role in regulating the cell cycle, emerging evidence now suggests it is also an important regulator of the DDR[174]. Indeed, biochemical studies have shown that HRR is defective in mouse embryonic fibroblasts following *CDK2* knock-down, knock-out, or inhibition, as CDK2 inhibition prevents the recruitment of RAD51 to DNA damage lesions[174]. Accordingly, CDK2 inhibition may exacerbate existing defects within the DDR and cell cycle within *RBX1*$^{+/-}$ clones, leading to enhanced SL phenotypes (***Figure 5-3***). Therefore, while additional research is required to identify the molecular mechanisms underlying the SL phenotypes, the results included in this thesis support the possibility that *CDK2* is an evolutionarily conserved SL interactor of the SCF complex and highlight the potential clinical utility of targeting CDK2 for the treatment of HGSOCs with diminished *RBX1* expression.

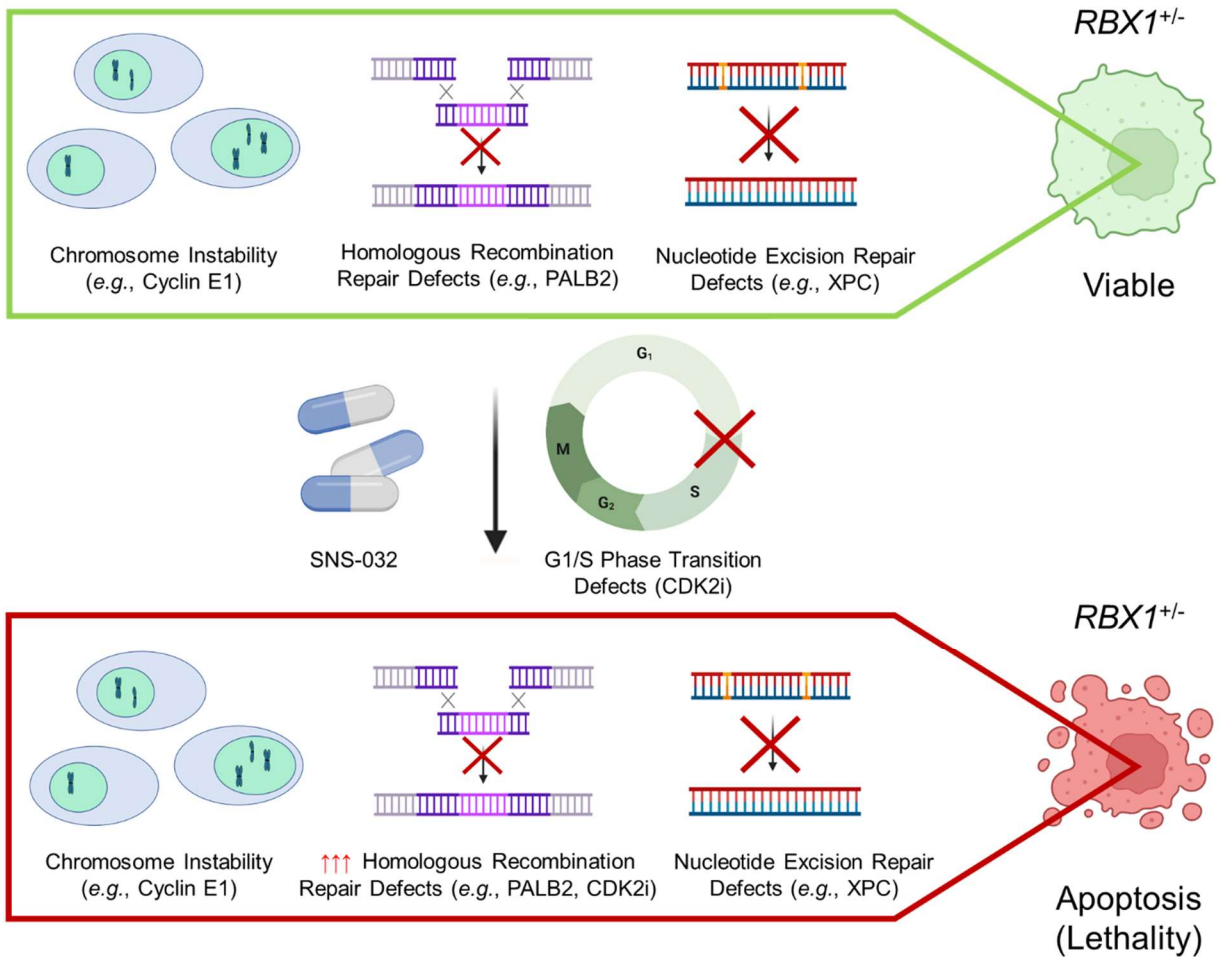

Figure 5-3. SNS-032 Selectively Targets *RBX1*$^{+/-}$ Clones.
Schematic illustrating the suspected molecular mechanism underlying selective decreases in *RBX1*$^{+/-}$ clones following treatment with SNS-032. *RBX1*$^{+/-}$ clones exhibit CIN and defects in HRR and/or NER due to the aberrant accumulation of substrate targets (*e.g.*, Cyclin E1, PALB2, XPC). Treatment with SNS-032 inhibits CDK2 and exacerbates existing defects in HRR (*e.g.*, RAD51) and causes cell cycle arrest at the G1/S phase transition in the cell cycle. CDK2 inhibition induces cell death via apoptosis due to the dependance of *RBX1*$^{+/-}$ clones on high CDK2/Cyclin E1 activity.

5.3 FUTURE EXPERIMENTAL DIRECTIONS

The results of this study support *PARP1* and *CDK2* as being novel SL interactors of *RBX1* in a novel heterozygous model and that diminished *RBX1* expression can be therapeutically exploited using a SL paradigm. While these findings explore the potential clinical utility of targeting PARP1 and CDK2 for the treatment of *RBX1*$^{+/-}$ HGSOCs, additional studies aimed at identifying the mechanisms through which *PARP1* and *CDK2* knock-down or inhibition induce selective decreases within *RBX1*$^{+/-}$ clones are required. Furthermore, assessing the

therapeutic benefit of utilizing PARP1 and/or CDK2 inhibitors in combination with standard-of-care chemotherapeutics and within clinically relevant 3-dimensional (3D) cell culture models is highly warranted.

5.3.1 Investigating the Potential Cell Death Mechanisms Underlying SL Phenotypes in *RBX1*$^{+/-}$ Clones following Treatment with Olaparib and SNS-032

Identifying the molecular mechanisms underlying SL phenotypes is essential for optimizing dose recommendations and drug safety, as individuals may have varying responses to chemotherapeutic treatments due to various genetic and/or environmental factors. First, Real-Time Cellular Analysis can be employed to determine whether the observed SL phenotypes (*i.e.*, decreases in cell numbers) within *RBX1*$^{+/-}$ clones following treatment with Olaparib or SNS-032 are due to a cell cycle arrest or cell death. Real-Time Cellular Analysis can monitor electrical impedance, termed cell index, to measure cell proliferation that can be used to generate growth curves to assess the impact of Olaparib or SNS-032 on *RBX1*$^{+/-}$ clones over time. Briefly, a stationary Cell Index (*i.e.*, extended plateau) following a specific treatment is indicative of a cell cycle arrest, whereas a rapid decrease in Cell Index (*i.e.*, curve decrease) is indicative of cell death. Should a SL interaction be observed, IIF approaches can be employed to assess changes in the relative abundance of key cell death markers within *RBX1*$^{+/-}$ clones relative to NT-Control clones. Recall that treatment with Olaparib or SNS-032 is known to induce apoptosis in cells exhibiting defects in HRR and increased expression levels of Cyclin E1, respectively (see ***Sections 5.2.2 and 5.2.3***)[100,158,170,178]. Accordingly, assessing changes in Cleaved Caspase-3 abundance (*i.e.*, an established apoptotic marker)[100,179] within *RBX1*$^{+/-}$ clones following treatment with either inhibitor could be informative. If the IIF results suggest that Olaparib and SNS-032 induce apoptosis within *RBX1*$^{+/-}$ clones, pan-caspase inhibitors such as Z-Val-Ala-Asp fluoromethyl ketone[40] (Z-VAD-FMK) can be employed to validate these findings and help discern whether additional cell death mechanisms may be contributing to SL phenotypes. For example, employing apoptosis inhibitors could shed insight into whether SL phenotypes were arising through the intrinsic or extrinsic apoptotic pathway by targeting specific caspase enzymes. In contrast, if apoptosis inhibitors do not prevent cell death from occurring, alternative cell death mechanisms can be explored, providing a more comprehensive understanding of the cellular response of *RBX1*$^{+/-}$ clones to treatment with Olaparib and SNS-032.

5.3.2 Evaluating the Potential Clinical Utility of Combining PARP1 and/or CDK2 Inhibitors with Standard-of-Care Chemotherapeutics

One of the major clinical challenges in treating HGSOC is that >70% of patients will ultimately develop drug-resistant disease[44]. Thus, determining the utility of combinatorial approaches involving PAPR1 and/or CDK2 inhibitors with and without standard of care agents is essential to improve HGSOC patient outcomes, as it may enhance therapeutic benefit through drug synergy or reducing the drug concentrations and/or mitigate the acquisition of multi-drug resistance to ultimately enhance quality of life. The current first-line standard of care for HGSOC patients is a combination carboplatin and paclitaxel (see ***Section 1.1.4***); however, most patients relapse within ~18 months of receiving their first-line treatments and ultimately succumb with drug resistant disease[4,180]. In this regard, combining PARP1 or CDK2 inhibitors may help to enhance and/or restore sensitivity to first-line chemotherapeutic agents. For example, as PARP1 inhibitors induce DSBs and platinum-based chemotherapies interfere with DNA transcription and translation[40] (see ***Sections 1.1.4 and 1.4.2***), administering an Olaparib/carboplatin combination may exhibit a therapeutic benefit. Indeed, clinical studies have shown that combining Olaparib with carboplatin increases progression free survival within HRR-deficient ovarian cancer patients[181]. In a similar manner, Brown *et al.*[176] determined that combining the CDK2 inhibitor BLU-222 with standard-of-care agents such as carboplatin, Olaparib or gemcitabine induced ovarian tumor regression even after treatment cessation. The results from this thesis show that *RBX1*$^{+/-}$ clones exhibit moderate sensitivity to Olaparib (~3-fold decrease) relative to treatment with SNS-032 (~10-fold decrease). Accordingly, exploring the synergistic potential of Olaparib with SNS-032 and/or first-line chemotherapy agents for the treatment of *RBX1*$^{+/-}$ HGSOCs is warranted. Conceptually, as PARP1 and CDK2 inhibitors exert their anti-tumor effects by impairing DNA repair and cell cycle progression[100,117,170,181], combinatorial approaches using Olaparib, SNS-032 and other first-line chemotherapy agents may have synergistic potential through the simultaneous disruption of multiple biological pathways. This may potentially enable the administration of lower, yet more effective drug doses, effectively maximizing the therapeutic benefit and minimizing the side effects to improve the lives and outcomes of individuals living with HGSOC.

5.3.3 Determining the Effectiveness of PARP1 and CDK2 Inhibitors in Clinically Relevant 3D Cell Culture and Xenograft Models

The tumor microenvironment is biologically complex, comprised of numerous tumor cells, stromal cells, and extracellular matrix components[182,183]. The use of 3D cell culture models, like spheroids or organoids has emerged as a valuable approach in ovarian cancer research studies[184], as they offer numerous benefits over traditional 2D cell culture models[185,186]. In an ovarian cancer studies, the term spheroid generally refers to multicellular aggregates that are grown in suspension and can be generated using cell lines or patient samples[187]. As ~30% of HGSOC patients develop ascites that require routine removal[187], spheroids could be generated from the isolated tumor cells of *RBX1*$^{+/-}$ individuals to monitor and predict *in vivo* responses to Olaparib and/or SNS-032 over the course of treatment (*i.e.*, months/years). In a different manner, organoids are complex three-dimensional structures that mimic the architecture and function of specific organs or tissues in the body and are more reflective of solid tumor samples. Synthetic extracellular matrices (*e.g.*, Matrigel, Cultrex) are often used for 3D cell culture to recapitulate this environment, enabling researchers to study the potential impact of tumor-stromal interactions, cell-cell communication, and extracellular matrix remodeling on treatment response[188,189]. As such, spheroids and organoids are more structurally complex than 2D cell culture models and can be derived from cell lines or patient samples using cancerous or non-cancerous tissue to enable the study of inter- and intratumoral heterogeneity[190], a key feature associated with HGSOC[11]. This is critical, as emerging evidence suggests that many technical limitations associated with 2D cell culture approaches contribute to the low success rate (~5%) of translating novel chemotherapeutics into the clinic[191]. Indeed, recent clinical studies have shown that 3D cell culture models are more reflective of the histological and molecular features of primary tumors than 2D cell culture models[191], and in many cases, can successfully recapitulate the *in vivo* drug responses of ovarian cancer patients[188]. Therefore, by incorporating a variety of cell types derived from cell lines or HGSOC patient samples, 3D cell culture models and can thus provide invaluable insight for the development of novel precision medicine strategies and offers a clinically relevant alternative to mouse models in a controlled *in vitro* setting. For example, generating patient-derived organoids from *RBX1*$^{+/-}$ HGSOCs and treating them with Olaparib and/or SNS-032 could further validate the findings from this thesis and could one day be employed for precision medicine strategies to guide patient care plans in real-time.

Finally, if SL phenotypes are observed under the above conditions, these studies could be adapted for *in vivo* drug response assays by injecting the experimental *RBX1*$^{+/-}$ cell lines into the peritoneum of immunocompromised (*e.g.*, OD-Rag1null IL2rgnull [NRG]) mice and treating them with Olaparib or SNS-032 following the emergence of cellular transformation phenotypes[56]. Collectively, these models provide a more physiologically relevant platform to investigate the potential therapeutic impact of PARP1 or CDK2 inhibition for the treatment of HGSOCs exhibiting diminished *RBX1* expression by better mimicking the biological complexities found within the *in vivo* tumor microenvironment.

5.4 CONCLUSIONS & SIGNIFICANCE

The findings presented in this thesis suggest that reduced *RBX1* expression can be therapeutically exploited using a SL paradigm and that *PARP1* and *CDK2* are novel SL interactors of *RBX1* in a HGSOC context. In this regard, silencing or inhibition of either target induces selective decreases in cell numbers and significant increases in DSBs in *RBX1*$^{+/-}$ clones. Collectively, these findings suggest that small-molecule inhibitors targeting PARP1 and CDK2, such as Olaparib and SNS-032, respectively, may hold clinical utility in the treatment of HGSOCs harboring heterozygous loss and reduced expression of *RBX1*. These data also highlight the potential clinical utility of *RBX1* as a therapeutic biomarker and examines the functional importance of RBX1 in the regulation of several essential biological pathways relative to other core SCF complex members. Collectively, the work presented in this thesis sheds novel insight into the potential utility of exploiting aberrant expression of the SCF complex for the treatment of HGSOC, while highlighting the novelty and biological complexities that are associated with utilizing clinically relevant heterozygous models for the development of precision medicine strategies to exploit novel SL interactions. Furthermore, these preliminary findings warrant additional experiments aimed at determining the molecular mechanisms leading to cell death and the therapeutic benefit of utilizing PARP1 and/or CDK2 inhibitors in combination with standard-of-care therapies within 3D and pre-clinical animal models.

HGSOC remains the most lethal gynecological malignancy, with an estimated ~3,100 Canadians diagnosed and ~1950 succumbing to their disease each year. As such, identifying new and more effective drug targets that can selectively exploit the aberrant genetics that are suspected to contribute to HGSOC pathogenesis (*e.g.*, defects in CIN genes such as *RBX1*) is

imperative for the development of novel therapeutic strategies to ultimately improve HGSOC patient lives and outcomes. Finally, while this thesis is focused exclusively on an HGSOC context, heterozygous loss of *RBX1* occurs in a myriad of cancer types. Thus, the results of this study may have broad-spectrum implications for therapeutic targeting in many additional cancer types, although this remains to be empirically determined.

REFERENCES

1 Canadian Cancer Statistics Advisory, C. Canadian Cancer Society's Advisory Committee on Cancer Statistics. *Canadian Cancer Statistics 2022* (2022).

2 Lim, D. & Oliva, E. Precursors and pathogenesis of ovarian carcinoma. *Pathology* **45**, 229-242, doi:10.1097/PAT.0b013e32835f2264 (2013).

3 Bowtell, D. D. The genesis and evolution of high-grade serous ovarian cancer. *Nat Rev Cancer* **10**, 803-808, doi:10.1038/nrc2946 (2010).

4 Cortez, A. J., Tudrej, P., Kujawa, K. A. & Lisowska, K. M. Advances in ovarian cancer therapy. *Cancer Chemother Pharmacol* **81**, 17-38, doi:10.1007/s00280-017-3501-8 (2018).

5 Lisio, M. A., Fu, L., Goyeneche, A., Gao, Z. H. & Telleria, C. High-Grade Serous Ovarian Cancer: Basic Sciences, Clinical and Therapeutic Standpoints. *Int J Mol Sci* **20**, doi:10.3390/ijms20040952 (2019).

6 Morden, C. R. *et al.* Chromosome instability is prevalent and dynamic in high-grade serous ovarian cancer patient samples. *Gynecol Oncol*, doi:10.1016/j.ygyno.2021.02.038 (2021).

7 Prat, J., D'Angelo, E. & Espinosa, I. Ovarian carcinomas: at least five different diseases with distinct histological features and molecular genetics. *Hum Pathol* **80**, 11-27, doi:10.1016/j.humpath.2018.06.018 (2018).

8 Reid, B. M., Permuth, J. B. & Sellers, T. A. Epidemiology of ovarian cancer: a review. *Cancer Biol Med* **14**, 9-32, doi:10.20892/j.issn.2095-3941.2016.0084 (2017).

9 Kurman, R. J. & Shih Ie, M. Molecular pathogenesis and extraovarian origin of epithelial ovarian cancer--shifting the paradigm. *Hum Pathol* **42**, 918-931, doi:10.1016/j.humpath.2011.03.003 (2011).

10 Torre, L. A. *et al.* Ovarian cancer statistics, 2018. *CA Cancer J Clin* **68**, 284-296, doi:10.3322/caac.21456 (2018).

11 Kroeger, P. T., Jr. & Drapkin, R. Pathogenesis and heterogeneity of ovarian cancer. *Curr Opin Obstet Gynecol* **29**, 26-34, doi:10.1097/GCO.0000000000000340 (2017).

12 Wiegand, K. & Shah, S. ARID1A Mutations in Endometriosis-Associated Ovarian Carcinomas. *The New England Journal of Medicine* **363** (2010).

13 Karst, A. M., Levanon, K. & Drapkin, R. Modeling high-grade serous ovarian carcinogenesis from the fallopian tube. *Proc Natl Acad Sci U S A* **108**, 7547-7552, doi:10.1073/pnas.1017300108 (2011).

14 Kuhn, E. *et al.* TP53 mutations in serous tubal intraepithelial carcinoma and concurrent pelvic high-grade serous carcinoma--evidence supporting the clonal relationship of the two lesions. *J Pathol* **226**, 421-426, doi:10.1002/path.3023 (2012).

15 Hoadley, K. A. *et al.* Cell-of-Origin Patterns Dominate the Molecular Classification of 10,000 Tumors from 33 Types of Cancer. *Cell* **173**, 291-304 e296, doi:10.1016/j.cell.2018.03.022 (2018).

16 Karst, A. M. *et al.* Cyclin E1 deregulation occurs early in secretory cell transformation to promote formation of fallopian tube-derived high-grade serous ovarian cancers. *Cancer Res* **74**, 1141-1152, doi:10.1158/0008-5472.CAN-13-2247 (2014).

17 Campos Gudino, R., Farrell, A. C., Neudorf, N. M. & McManus, K. J. A Comprehensive Assessment of Genetic and Epigenetic Alterations Identifies Frequent Variations Impacting Six Prototypic SCF Complex Members. *Int J Mol Sci* **23**, doi:10.3390/ijms23010084 (2021).

18 Mukhopadhyay, A. *et al.* Development of a functional assay for homologous recombination status in primary cultures of epithelial ovarian tumor and correlation with sensitivity to poly(ADP-ribose) polymerase inhibitors. *Clin Cancer Res* **16**, 2344-2351, doi:10.1158/1078-0432.CCR-09-2758 (2010).
19 Mukhopadhyay, A. *et al.* Clinicopathological features of homologous recombination-deficient epithelial ovarian cancers: sensitivity to PARP inhibitors, platinum, and survival. *Cancer Res* **72**, 5675-5682, doi:10.1158/0008-5472.CAN-12-0324 (2012).
20 Risch, H. A. *et al.* Population BRCA1 and BRCA2 mutation frequencies and cancer penetrances: a kin-cohort study in Ontario, Canada. *J Natl Cancer Inst* **98**, 1694-1706, doi:10.1093/jnci/djj465 (2006).
21 King, M., Marks, J. & Mandell, J. Breast and Ovarian Cancer Risks Due to Inherited Mutations in BRCA1 and BRCA2. *Science* **302** (2003).
22 Kauff, N. D. & Barakat, R. R. Risk-reducing salpingo-oophorectomy in patients with germline mutations in BRCA1 or BRCA2. *J Clin Oncol* **25**, 2921-2927, doi:10.1200/JCO.2007.11.3449 (2007).
23 Piek, J. M. *et al.* Dysplastic changes in prophylactically removed Fallopian tubes of women predisposed to developing ovarian cancer. *J Pathol* **195**, 451-456, doi:10.1002/path.1000 (2001).
24 Cancer Genome Atlas Research, N. Integrated genomic analyses of ovarian carcinoma. *Nature* **474**, 609-615, doi:10.1038/nature10166 (2011).
25 Ahmed, A. A. *et al.* Driver mutations in TP53 are ubiquitous in high grade serous carcinoma of the ovary. *J Pathol* **221**, 49-56, doi:10.1002/path.2696 (2010).
26 Kobel, M. *et al.* Optimized p53 immunohistochemistry is an accurate predictor of TP53 mutation in ovarian carcinoma. *J Pathol Clin Res* **2**, 247-258, doi:10.1002/cjp2.53 (2016).
27 Kindelberger, D. *et al.* Intraepithelial Carcinoma of the Fimbria and Pelvic Serous Carcinoma- Evidence for a Causal Relationship. *Am J Physiol Surg Pathol* **31** (2007).
28 Crum, C., Drapkin, R., Miron, A., Ince, T. & Lee, Y. The distal fallopian tube- a new model for pelvic serous carcinogenesis. *Current Opinion in Obstetrics and Gynecology* **9** (2007).
29 Soong, T. R., Kolin, D. L., Teschan, N. J. & Crum, C. P. Back to the Future? The Fallopian Tube, Precursor Escape and a Dualistic Model of High-Grade Serous Carcinogenesis. *Cancers (Basel)* **10**, doi:10.3390/cancers10120468 (2018).
30 Coleman, R. L., Monk, B. J., Sood, A. K. & Herzog, T. J. Latest research and treatment of advanced-stage epithelial ovarian cancer. *Nat Rev Clin Oncol* **10**, 211-224, doi:10.1038/nrclinonc.2013.5 (2013).
31 Menon, U. *et al.* Ovarian cancer population screening and mortality after long-term follow-up in the UK Collaborative Trial of Ovarian Cancer Screening (UKCTOCS): a randomised controlled trial. *Lancet* **397**, 2182-2193, doi:10.1016/s0140-6736(21)00731-5 (2021).
32 Whitwell, H. J. *et al.* Improved early detection of ovarian cancer using longitudinal multimarker models. *Br J Cancer* **122**, 847-856, doi:10.1038/s41416-019-0718-9 (2020).
33 Kessous, R. *et al.* CA-125 reduction during neoadjuvant chemotherapy is associated with success of cytoreductive surgery and outcome of patients with advanced high-grade ovarian cancer. *Acta Obstet Gynecol Scand* **99**, 933-940, doi:10.1111/aogs.13814 (2020).

34 Doubeni, C., Doubeni, A. & Myers, A. *Diagnosis and management of ovarian disorders.*, Vol. 93 937–944 (2016).
35 Cohen, J. D. *et al.* Detection and localization of surgically resectable cancers with a multi-analyte blood test. *Science* **359**, 926-930, doi:10.1126/science.aar3247 (2018).
36 Berek, J. S., Renz, M., Kehoe, S., Kumar, L. & Friedlander, M. Cancer of the ovary, fallopian tube, and peritoneum: 2021 update. *International Journal of Gynecology & Obstetrics* **155**, 61-85, doi:https://doi.org/10.1002/ijgo.13878 (2021).
37 Cancer., A. J. C. o. in *AJCC Cancer Staging Manual, 8th Ed.* (ed Springer) (2017).
38 Berek, J. S., Kehoe, S. T., Kumar, L. & Friedlander, M. Cancer of the ovary, fallopian tube, and peritoneum. *Int J Gynaecol Obstet* **143 Suppl 2**, 59-78, doi:10.1002/ijgo.12614 (2018).
39 Gadducci, A. *et al.* Current strategies for the targeted treatment of high-grade serous epithelial ovarian cancer and relevance of BRCA mutational status. *J Ovarian Res* **12**, 9, doi:10.1186/s13048-019-0484-6 (2019).
40 Wishart, D. S. *et al.* DrugBank 5.0: a major update to the DrugBank database for 2018. *Nucleic Acids Res* **46**, D1074-D1082, doi:10.1093/nar/gkx1037 (2018).
41 Devlin, E. J., Denson, L. A. & Whitford, H. S. Cancer Treatment Side Effects: A Meta-analysis of the Relationship Between Response Expectancies and Experience. *J Pain Symptom Manage* **54**, 245-258 e242, doi:10.1016/j.jpainsymman.2017.03.017 (2017).
42 Mikula-Pietrasik, J. *et al.* Comprehensive review on how platinum- and taxane-based chemotherapy of ovarian cancer affects biology of normal cells. *Cell Mol Life Sci* **76**, 681-697, doi:10.1007/s00018-018-2954-1 (2019).
43 Mateo, J. *et al.* A decade of clinical development of PARP inhibitors in perspective. *Ann Oncol* **30**, 1437-1447, doi:10.1093/annonc/mdz192 (2019).
44 Sherman-Baust, C. A., Becker, K. G., Wood Iii, W. H., Zhang, Y. & Morin, P. J. Gene expression and pathway analysis of ovarian cancer cells selected for resistance to cisplatin, paclitaxel, or doxorubicin. *J Ovarian Res* **4**, 21, doi:10.1186/1757-2215-4-21 (2011).
45 Herzog, T. J. Clinical experience with topotecan in relapsed ovarian cancer. *Gynecologic Oncology* **90**, S3-S7, doi:10.1016/s0090-8258(03)00467-0 (2003).
46 Fowler, W. C., Jr. & Van Le, L. Gemcitabine as a single-agent treatment for ovarian cancer. *Gynecol Oncol* **90**, S21-23, doi:10.1016/s0090-8258(03)00340-8 (2003).
47 Lawrie, T. A., Bryant, A., Cameron, A., Gray, E. & Morrison, J. Pegylated liposomal doxorubicin for relapsed epithelial ovarian cancer. *Cochrane Database Syst Rev* **2013**, CD006910, doi:10.1002/14651858.CD006910.pub2 (2013).
48 Leary, A., Tan, D. & Ledermann, J. Immune checkpoint inhibitors in ovarian cancer: where do we stand? *Ther Adv Med Oncol* **13**, 17588359211039899, doi:10.1177/17588359211039899 (2021).
49 Kim, J. Y. *et al.* Tumor Mutational Burden and Efficacy of Immune Checkpoint Inhibitors: A Systematic Review and Meta-Analysis. *Cancers (Basel)* **11**, doi:10.3390/cancers11111798 (2019).
50 Zamarin, D. *et al.* Randomized Phase II Trial of Nivolumab Versus Nivolumab and Ipilimumab for Recurrent or Persistent Ovarian Cancer: An NRG Oncology Study. *J Clin Oncol* **38**, 1814-1823, doi:10.1200/JCO.19.02059 (2020).
51 Geigl, J. B., Obenauf, A. C., Schwarzbraun, T. & Speicher, M. R. Defining 'chromosomal instability'. *Trends Genet* **24**, 64-69, doi:10.1016/j.tig.2007.11.006 (2008).

52 Hanahan, D. & Weinberg, R. A. Hallmarks of cancer: the next generation. *Cell* **144**, 646-674, doi:10.1016/j.cell.2011.02.013 (2011).
53 Nojadeh, J. N., Behrouz Sharif, S. & Sakhinia, E. Microsatellite instability in colorectal cancer. *EXCLI J* **17**, 159-168, doi:10.17179/excli2017-948 (2018).
54 Sajesh, B. V., Guppy, B. J. & McManus, K. J. Synthetic genetic targeting of genome instability in cancer. *Cancers (Basel)* **5**, 739-761, doi:10.3390/cancers5030739 (2013).
55 Thompson, L. L., Baergen, A. K., Lichtensztejn, Z. & McManus, K. J. Reduced SKP1 Expression Induces Chromosome Instability through Aberrant Cyclin E1 Protein Turnover. *Cancers (Basel)* **12**, doi:10.3390/cancers12030531 (2020).
56 Bungsy, M. *et al.* Reduced RBX1 expression induces chromosome instability and promotes cellular transformation in high-grade serous ovarian cancer precursor cells. *Cancer Lett* **500**, 194-207, doi:10.1016/j.canlet.2020.11.051 (2021).
57 Lepage, C. C. *et al.* Reduced SKP1 and CUL1 expression underlies increases in Cyclin E1 and chromosome instability in cellular precursors of high-grade serous ovarian cancer. *Br J Cancer* **124**, 1699-1710, doi:10.1038/s41416-021-01317-w (2021).
58 Palmer, M. C. L. *et al.* The F-box protein, FBXO7 is required to maintain chromosome stability in humans. *Hum Mol Genet*, doi:10.1093/hmg/ddab330 (2021).
59 Thompson, L. L., Rutherford, K. A., Lepage, C. C. & McManus, K. J. The SCF Complex Is Essential to Maintain Genome and Chromosome Stability. *Int J Mol Sci* **22**, doi:10.3390/ijms22168544 (2021).
60 Neudorf, N. M., Thompson, L. L., Lichtensztejn, Z., Razi, T. & McManus, K. J. Reduced SKP2 Expression Adversely Impacts Genome Stability and Promotes Cellular Transformation in Colonic Epithelial Cells. *Cells* **11**, doi:10.3390/cells11233731 (2022).
61 Bakhoum, S. F. & Compton, D. A. Chromosomal instability and cancer: a complex relationship with therapeutic potential. *J Clin Invest* **122**, 1138-1143, doi:10.1172/JCI59954 (2012).
62 Lepage, C. C., Morden, C. R., Palmer, M. C. L., Nachtigal, M. W. & McManus, K. J. Detecting Chromosome Instability in Cancer: Approaches to Resolve Cell-to-Cell Heterogeneity. *Cancers (Basel)* **11**, doi:10.3390/cancers11020226 (2019).
63 Thompson, S. L., Bakhoum, S. F. & Compton, D. A. Mechanisms of chromosomal instability. *Curr Biol* **20**, R285-295, doi:10.1016/j.cub.2010.01.034 (2010).
64 Thompson, L. L. & McManus, K. J. A novel multiplexed, image-based approach to detect phenotypes that underlie chromosome instability in human cells. *PLoS One* **10**, e0123200, doi:10.1371/journal.pone.0123200 (2015).
65 Markowitz, S. D. & Bertagnolli, M. M. Molecular origins of cancer: Molecular basis of colorectal cancer. *N Engl J Med* **361**, 2449-2460, doi:10.1056/NEJMra0804588 (2009).
66 Nowak, M. A. *et al.* The role of chromosomal instability in tumor initiation. *PNAS* **99**, 6, doi:doi.org/10.1073/pnas.202617399 (2002).
67 Gerlinger, M. & Swanton, C. How Darwinian models inform therapeutic failure initiated by clonal heterogeneity in cancer medicine. *Br J Cancer* **103**, 1139-1143, doi:10.1038/sj.bjc.6605912 (2010).
68 Lee, A. J. *et al.* Chromosomal instability confers intrinsic multidrug resistance. *Cancer Res* **71**, 1858-1870, doi:10.1158/0008-5472.CAN-10-3604 (2011).
69 Thompson, L. L., Jeusset, L. M., Lepage, C. C. & McManus, K. J. Evolving Therapeutic Strategies to Exploit Chromosome Instability in Cancer. *Cancers (Basel)* **9**, doi:10.3390/cancers9110151 (2017).

70 Penner-Goeke, S. *et al.* The temporal dynamics of chromosome instability in ovarian cancer cell lines and primary patient samples. *PLoS Genet* **13**, e1006707, doi:10.1371/journal.pgen.1006707 (2017).
71 Hershko, A. & Ciechanover, A. The ubiquitin system. *Annu Rev. Biochem* **67** (1998).
72 Willems, A. R., Schwab, M. & Tyers, M. A hitchhiker's guide to the cullin ubiquitin ligases: SCF and its kin. *Biochim Biophys Acta* **1695**, 133-170, doi:10.1016/j.bbamcr.2004.09.027 (2004).
73 Thrower, J., Hoffman, L., Rechsteiner, M. & Pickart, C. Recognition of the polyubiquitin proteolytic signal. *European Molecular Biology Organization* **19** (2000).
74 Akhoondi, S. *et al.* FBXW7/hCDC4 is a general tumor suppressor in human cancer. *Cancer Res* **67**, 9006-9012, doi:10.1158/0008-5472.CAN-07-1320 (2007).
75 Otto, T. *et al.* Stabilization of N-Myc is a critical function of Aurora A in human neuroblastoma. *Cancer Cell* **15**, 67-78, doi:10.1016/j.ccr.2008.12.005 (2009).
76 Marzio, A. *et al.* The F-Box Domain-Dependent Activity of EMI1 Regulates PARPi Sensitivity in Triple-Negative Breast Cancers. *Mol Cell* **73**, 224-237 e226, doi:10.1016/j.molcel.2018.11.003 (2019).
77 Safran, M. *et al.* in *Practical Guide to Life Science Databases* Ch. Chapter 2, 27-56 (2021).
78 Schulman, B., Carrano, A., Jeffery, P., Bowen, Z. & Kinnucan, E. Insights into SCF ubiquitin ligases from the structure of the Skp1–Skp2 complex. *Nature* **408** (2000).
79 Jin, J. *et al.* Systematic analysis and nomenclature of mammalian F-box proteins. *Genes Dev* **18**, 2573-2580, doi:10.1101/gad.1255304 (2004).
80 Sarikas, A., Hartmann, T. & Pan, Z. The cullin protein family. *Genome Biology* **12**, 12, doi:10.1186/gb-2011-12-4-220 (2011).
81 Gong, L. & Yeh, E. T. Identification of the activating and conjugating enzymes of the NEDD8 conjugation pathway. *J Biol Chem* **274**, 12036-12042, doi:10.1074/jbc.274.17.12036 (1999).
82 Kawakami, T. *et al.* NEDD8 recruits E2-ubiquitin to SCF E3 ligase. *European Molecular Biology Organization* **20**, 10, doi:10.1093/emboj/20.15.4003 (2001).
83 Tan, M., Davis, S., Saunders, T., Zhu, Y. & Sun, Y. RBX1 ROC1 disruption results in early embryonic lethality due to proliferation failure, partially rescued by simultaneous loss of p27. *PNAS* **106** (2009).
84 Ohta, T., Michael, J. & Xiong, Y. Association with cullin partners protects ROC proteins from proteasome-dependent degradation. *Oncogene* **18** (1999).
85 Chen, A. *et al.* The conserved RING-H2 finger of ROC1 is required for ubiquitin ligation. *J Biol Chem* **275**, 15432-15439, doi:10.1074/jbc.M907300199 (2000).
86 Seol, J., Feldman, R. & Zachariae, W. Cdc53 cullin and the essential Hrt1 RING–H2 subunit of SCF define a ubiquitin ligase module that activates the E2 enzyme Cdc34. *Genes & Development* **13** (1999).
87 Jia, L., Soengas, M. S. & Sun, Y. ROC1/RBX1 E3 ubiquitin ligase silencing suppresses tumor cell growth via sequential induction of G2-M arrest, apoptosis, and senescence. *Cancer Res* **69**, 4974-4982, doi:10.1158/0008-5472.CAN-08-4671 (2009).
88 Furukawa, M., Ohta, T. & Xiong, Y. Activation of UBC5 ubiquitin-conjugating enzyme by the RING finger of ROC1 and assembly of active ubiquitin ligases by all cullins. *J Biol Chem* **277**, 15758-15765, doi:10.1074/jbc.M108565200 (2002).

89 Kamura, T., Conrad, M. N., Yan, Q., Conaway, R. C. & Conaway, J. W. The Rbx1 subunit of SCF and VHL E3 ubiquitination ligase activates Rub1 modification of cullins Cdc53 and Cul2. *Genes & Development* **13**, 6, doi:10.1101/gad.13.22.2928 (1999).
90 Orthwein, A. *et al.* A mechanism for the suppression of homologous recombination in G1 cells. *Nature* **528**, 422-426, doi:10.1038/nature16142 (2015).
91 Zhang, F. *et al.* PALB2 links BRCA1 and BRCA2 in the DNA-damage response. *Curr Biol* **19**, 524-529, doi:10.1016/j.cub.2009.02.018 (2009).
92 Sy, S., Huen, M. & Chen, J. PALB2 is an integral component of the BRCA complex required for homologous recombination repair. *PNAS* **106**, 7155-7160 (2009).
93 Koepp, D. M. *et al.* Phosphorylation-Dependent Ubiquitination of Cyclin E by the SCFFbw7 Ubiquitin Ligase. *Science* **294**, 4, doi:10.1126/science.1065203 (2011).
94 Postow, L. & Funabiki, H. An SCF complex containing Fbxl12 mediates DNA damage-induced Ku80 ubiquitylation. *Cell Cycle* **12**, 587-595, doi:10.4161/cc.23408 (2013).
95 Jia, L. & Sun, Y. SCF E3 Ubiquitin Ligases as Anticancer Targets. *Current Cancer Drug Targets* **11** (2011).
96 Gao, J. *et al.* Integrative analysis of complex cancer genomics and clinical profiles using the cBioPortal. *Sci Signal* **6**, pl1, doi:10.1126/scisignal.2004088 (2013).
97 Yeh, C. H., Bellon, M. & Nicot, C. FBXW7: a critical tumor suppressor of human cancers. *Mol Cancer* **17**, 115, doi:10.1186/s12943-018-0857-2 (2018).
98 Etemadmoghadam, D. *et al.* Synthetic lethality between CCNE1 amplification and loss of BRCA1. *Proc Natl Acad Sci U S A* **110**, 19489-19494, doi:10.1073/pnas.1314302110 (2013).
99 Sajesh, B. V., Bailey, M., Lichtensztejn, Z., Hieter, P. & McManus, K. J. Synthetic lethal targeting of superoxide dismutase 1 selectively kills RAD54B-deficient colorectal cancer cells. *Genetics* **195**, 757-767, doi:10.1534/genetics.113.156836 (2013).
100 Guppy, B. J. & McManus, K. J. Synthetic lethal targeting of RNF20 through PARP1 silencing and inhibition. *Cell Oncol (Dordr)* **40**, 281-292, doi:10.1007/s13402-017-0323-y (2017).
101 Nizialek, E. & Antonarakis, E. S. PARP Inhibitors in Metastatic Prostate Cancer: Evidence to Date. *Cancer Manag Res* **12**, 8105-8114, doi:10.2147/CMAR.S227033 (2020).
102 Li, K. *et al.* Cyclin-dependent kinases-based synthetic lethality: Evidence, concept, and strategy. *Acta Pharm Sin B* **11**, 2738-2748, doi:10.1016/j.apsb.2021.01.002 (2021).
103 O'Neil, N. J., Bailey, M. L. & Hieter, P. Synthetic lethality and cancer. *Nat Rev Genet* **18**, 613-623, doi:10.1038/nrg.2017.47 (2017).
104 Bridges, C. The Origin of Variations in Sexual and Sex-Limited Characters. *The American Naturalist* **56** (1922).
105 Dobzhanzky, T. Genetics of Natural Populations. Xiii. Recombination and Variability in Populations of Drosophila Pseudoobscura. *Genetics* **31** (1946).
106 Jeusset, L. M. & McManus, K. J. in *Methods Mol Biol* Vol. 2381 Ch. 6, 115-133 (2021).
107 Costanzo, M. *et al.* A global genetic interaction network maps a wiring diagram of cellular function. *Science* **353**, doi:10.1126/science.aaf1420 (2016).
108 Costanzo, M. *et al.* The genetic landscape of a cell. *Science* **327**, 425-431, doi:10.1126/science.1180823 (2010).

109 Collins, S. R. *et al.* Functional dissection of protein complexes involved in yeast chromosome biology using a genetic interaction map. *Nature* **446**, 806-810, doi:10.1038/nature05649 (2007).
110 Bryant, H. E. *et al.* Specific killing of BRCA2-deficient tumours with inhibitors of poly(ADP-ribose) polymerase. *Nature* **434**, 913-916 (2005).
111 Farmer, H. *et al.* Targeting the DNA repair defect in BRCA2 mutant cells as a therapeutic strategy. *Nature* **434**, 917-910 (2005).
112 Lord, C. J. & Ashworth, A. PARP inhibitors: Synthetic Lethality in the Clinic. *Science* **355**, 1152-1158 (2017).
113 Hartwell, L. H., Szankasi, P., Roberts, C. J., Murray, A. W. & Friend, S. H. Integrating Genetic Approaches into the Discovery of Anticancer Drugs. *Science* **278**, 1064-1068, doi:DOI: 10.1126/science.278.5340.1064 (1997).
114 Kaelin, W. Choosing anticancer drug targets in the postgenomic era. *The Journal of Clinical Investigation* **104** (1999).
115 Friend, S. & Oliff, A. Emerging uses for genomic information in drug discovery. *The New England Journal of Medicine* **338** (1998).
116 Ray Chaudhuri, A. & Nussenzweig, A. The multifaceted roles of PARP1 in DNA repair and chromatin remodelling. *Nat Rev Mol Cell Biol* **18**, 610-621, doi:10.1038/nrm.2017.53 (2017).
117 Parsels, L. A. *et al.* Combinatorial Efficacy of Olaparib with Radiation and ATR Inhibitor Requires PARP1 Protein in Homologous Recombination-Proficient Pancreatic Cancer. *Mol Cancer Ther* **20**, 263-273, doi:10.1158/1535-7163.MCT-20-0365 (2021).
118 Kroll, E., Hyland, K., Hieter, P. & Li, J. Establishing genetic interactions by a synthetic dosage lethality phenotype. *Genetics* **143** (1996).
119 Cerami, E. *et al.* The cBio cancer genomics portal: an open platform for exploring multidimensional cancer genomics data. *Cancer Discov* **2**, 401-404, doi:10.1158/2159-8290.CD-12-0095 (2012).
120 Garson, J., Pemberton, L., Sheppard, P. & Varndell, I. N-myc gene expression and oncoprotein characterisation in medulloblastoma. *Br J Cancer* **59** (1989).
121 Schwab, M. Enhanced expression of the cellular oncogene MYCN and progression of human neuroblastoma. *Advances in enzyme regulation* (1991).
122 Molenaar, J., Ebus, M., Geers, D., Koster, J. & Lamers, F. Inactivation of CDK2 is synthetically lethal to MYCN over-expressing cancer cells. *PNAS* **106** (2009).
123 Lord, C. J., McDonald, S., Swift, S., Turner, N. C. & Ashworth, A. A high-throughput RNA interference screen for DNA repair determinants of PARP inhibitor sensitivity. *DNA Repair (Amst)* **7**, 2010-2019, doi:10.1016/j.dnarep.2008.08.014 (2008).
124 Srivas, R. *et al.* A Network of Conserved Synthetic Lethal Interactions for Exploration of Precision Cancer Therapy. *Mol Cell* **63**, 514-525, doi:10.1016/j.molcel.2016.06.022 (2016).
125 Du, D. *et al.* Genetic interaction mapping in mammalian cells using CRISPR interference. *Nat Methods* **14**, 577-580, doi:10.1038/nmeth.4286 (2017).
126 Wong, A. S. *et al.* Multiplexed barcoded CRISPR-Cas9 screening enabled by CombiGEM. *Proc Natl Acad Sci U S A* **113**, 2544-2549, doi:10.1073/pnas.1517883113 (2016).
127 Han, K. *et al.* Synergistic drug combinations for cancer identified in a CRISPR screen for pairwise genetic interactions. *Nat Biotechnol* **35**, 463-474, doi:10.1038/nbt.3834 (2017).

128 Sajesh, B. V. & McManus, K. J. Targeting SOD1 induces SL killing in BLM and CHEK2-deficient colorectal cancer cells. *Oncotarget* **6**, 16, doi:10.18632/oncotarget.4875 (2015).
129 Oughtred, R. *et al.* The BioGRID database: A comprehensive biomedical resource of curated protein, genetic, and chemical interactions. *Protein Sci* **30**, 187-200, doi:10.1002/pro.3978 (2021).
130 Spa¨nkuch-Schmitt, B., Bereiter-Hahn, J., Kaufmann, M. & Strebhardt, K. Effect of RNA silencing of polo-like kinase-1 (PLK1) on apoptosis and spindle formation in human cancer cells. *Journal of the National Cancer Institute* **94** (2002).
131 Liu, X. & Erikson, R. Polo-like kinase (Plk)1 depletion induces apoptosis in cancer cells. *PNAS* **100** (2003).
132 Rogakou, E. P., Pilch, D. R., Orr, A. H., Ivanova, V. S. & Bonner, W. M. DNA double-stranded breaks induce histone H2AX phosphorylation on serine 139. *J Biol Chem* **273**, 5858-5868, doi:10.1074/jbc.273.10.5858 (1998).
133 Guo, J., Liu, H. & Zheng, J. SynLethDB: synthetic lethality database toward discovery of selective and sensitive anticancer drug targets. *Nucleic Acids Res* **44**, D1011-1017, doi:10.1093/nar/gkv1108 (2016).
134 Wu, M. *et al.* In silico prediction of synthetic lethality by meta-analysis of genetic interactions, functions, and pathways in yeast and human cancer. *Cancer Inform* **13**, 71-80, doi:10.4137/CIN.S14026 (2014).
135 UniProt, C. UniProt: the universal protein knowledgebase in 2021. *Nucleic Acids Res* **49**, D480-D489, doi:10.1093/nar/gkaa1100 (2021).
136 Tunçer, S. *et al.* Low dose dimethyl sulfoxide driven gross molecular changes have the potential to interfere with various cellular processes. *Sci Rep* **8**, 14828, doi:10.1038/s41598-018-33234-z (2018).
137 Kang, M. A. *et al.* Anticancer and radiosensitizing effects of the cyclin-dependent kinase inhibitors, AT7519 and SNS-032, on cervical cancer. *Int J Oncol* **53**, 703-712, doi:10.3892/ijo.2018.4424 (2018).
138 Postow, L. *et al.* Ku80 removal from DNA through double strand break-induced ubiquitylation. *J Cell Biol* **182**, 467-479, doi:10.1083/jcb.200802146 (2008).
139 Li, J. M. & Jin, J. CRL Ubiquitin Ligases and DNA Damage Response. *Front Oncol* **2**, 29, doi:10.3389/fonc.2012.00029 (2012).
140 Singer, J. D., Gurian-West, M., Clurman, B. & Roberts, J. M. Cullin-3 targets cyclin E for ubiquitination and controls S phase in mammalian cells. *Genes & Development* **13**, 12, doi:10.1101/gad.13.18.2375 (1999).
141 Wang, Y. *et al.* Deletion of the Cul1 gene in mice causes arrest in early embryogenesis and accumulation of cyclin E. *Current Biology* **9**, 1191-1194, doi:10.1016/S0960-9822(00)80024-X (1999).
142 Nayak, S. *et al.* The Caenorhabditis elegans Skp1-Related Gene Family: Diverse Functions in Cell Proliferation, Morphogenesis, and Meiosis. *Current Biology* **12**, 277-287, doi:10.1016/S0960-9822(02)00682-6 (2002).
143 Dias, D. C., Dolios, G., Wang, R. & Pan, Z. Q. CUL7: A DOC domain-containing cullin selectively binds Skp1.Fbx29 to form an SCF-like complex. *Proc Natl Acad Sci U S A* **99**, 16601-16606, doi:10.1073/pnas.252646399 (2002).
144 SAG, a Novel Zinc RING Finger Protein That Protects Cells from Apoptosis Induced by Redox Agents.

145 RBX1-ROC1 disruption results in early embryonic lethality due to proliferation failure, partially rescued by simultaneous loss of p27.
146 Kamura, T. *et al.* VHL-box and SOCS-box domains determine binding specificity for Cul2-Rbx1 and Cul5-Rbx2 modules of ubiquitin ligases. *Genes Dev* **18**, 3055-3065, doi:10.1101/gad.1252404 (2004).
147 ROC1, a homolog of APC11, represents a family of cullin partners with an associated ubiquitin ligase activity.
148 Y, S. Cullin-RING Ligases And Protein Neddylation.
149 Scrima, A. *et al.* Detecting UV-lesions in the genome: The modular CRL4 ubiquitin ligase does it best! *FEBS Lett* **585**, 2818-2825, doi:10.1016/j.febslet.2011.04.064 (2011).
150 Genetic Disruption of KEAP1 CUL3 E3 Ubiquitin Ligase Complex Components is a Key Mechanism of NF-KappaB Pathway Activation in Lung Cancer.
151 Hannah, J. & Zhou, P. Distinct and overlapping functions of the cullin E3 ligase scaffolding proteins CUL4A and CUL4B. *Gene* **573**, 33-45, doi:10.1016/j.gene.2015.08.064 (2015).
152 Scharer, O. D. Nucleotide excision repair in eukaryotes. *Cold Spring Harb Perspect Biol* **5**, a012609, doi:10.1101/cshperspect.a012609 (2013).
153 Kim, D. S., Camacho, C. V. & Kraus, W. L. Alternate therapeutic pathways for PARP inhibitors and potential mechanisms of resistance. *Exp Mol Med* **53**, 42-51, doi:10.1038/s12276-021-00557-3 (2021).
154 Zheng, F. *et al.* Mechanism and current progress of Poly ADP-ribose polymerase (PARP) inhibitors in the treatment of ovarian cancer. *Biomed Pharmacother* **123**, 109661, doi:10.1016/j.biopha.2019.109661 (2020).
155 Stewart, M. D. *et al.* Homologous Recombination Deficiency: Concepts, Definitions, and Assays. *Oncologist* **27**, 167-174, doi:10.1093/oncolo/oyab053 (2022).
156 Mirza, M. R. *et al.* Niraparib Maintenance Therapy in Platinum-Sensitive, Recurrent Ovarian Cancer. *N Engl J Med* **375**, 2154-2164, doi:10.1056/NEJMoa1611310 (2016).
157 Kim, D.-S. *et al.* Activation of PARP-1 by snoRNAs Controls Ribosome Biogenesis and Cell Growth via the RNA Helicase DDX21. *Molecular Cell* **75**, 1270-1285.e1214, doi:10.1016/j.molcel.2019.06.020 (2019).
158 Keung, M. Y., Wu, Y., Badar, F. & Vadgama, J. V. Response of Breast Cancer Cells to PARP Inhibitors Is Independent of BRCA Status. *J Clin Med* **9**, doi:10.3390/jcm9040940 (2020).
159 Valabrega, G., Scotto, G., Tuninetti, V., Pani, A. & Scaglione, F. Differences in PARP Inhibitors for the Treatment of Ovarian Cancer: Mechanisms of Action, Pharmacology, Safety, and Efficacy. *Int J Mol Sci* **22**, doi:10.3390/ijms22084203 (2021).
160 Neumeier, J. & Meister, G. siRNA Specificity: RNAi Mechanisms and Strategies to Reduce Off-Target Effects. *Front Plant Sci* **11**, 526455, doi:10.3389/fpls.2020.526455 (2020).
161 Ström, C. E. *et al.* Poly (ADP-ribose) polymerase (PARP) is not involved in base excision repair but PARP inhibition traps a single-strand intermediate. *Nucleic Acids Research* **39**, 3166-3175, doi:10.1093/nar/gkq1241 (2010).
162 Yang, Y. G., Cortes, U., Patnaik, S., Jasin, M. & Wang, Z. Q. Ablation of PARP-1 does not interfere with the repair of DNA double-strand breaks, but compromises the reactivation of stalled replication forks. *Oncogene* **23**, 3872-3882, doi:10.1038/sj.onc.1207491 (2004).

163 Buisson, R. *et al.* Cooperation of breast cancer proteins PALB2 and piccolo BRCA2 in stimulating homologous recombination. *Nat Struct Mol Biol* **17**, 1247-1254, doi:10.1038/nsmb.1915 (2010).
164 Giam, M. & Rancati, G. Aneuploidy and chromosomal instability in cancer: a jackpot to chaos. *Cell Div* **10**, 3, doi:10.1186/s13008-015-0009-7 (2015).
165 McGranahan, N., Burrell, R. A., Endesfelder, D., Novelli, M. R. & Swanton, C. Cancer chromosomal instability: therapeutic and diagnostic challenges. *EMBO Rep* **13**, 528-538, doi:10.1038/embor.2012.61 (2012).
166 Li, K. *et al.* Cyclin-dependent kinases-based synthetic lethality: Evidence, concept, and strategy. *Acta Pharmaceutica Sinica B* **11**, 2738-2748, doi:https://doi.org/10.1016/j.apsb.2021.01.002 (2021).
167 Fagundes, R. & Teixeira, L. K. Cyclin E/CDK2: DNA Replication, Replication Stress and Genomic Instability. *Frontiers in Cell and Developmental Biology* **9**, doi:10.3389/fcell.2021.774845 (2021).
168 Fang, D., Huang, S. & Su, S. B. Cyclin E1-CDK 2, a potential anticancer target. *Aging (Albany NY)* **8**, 571-572, doi:10.18632/aging.100946 (2016).
169 Chakravarty, D. *et al.* OncoKB: A Precision Oncology Knowledge Base. *JCO Precision Oncology*, 1-16, doi:10.1200/po.17.00011 (2017).
170 Yang, L. *et al.* Cyclin-dependent kinase 2 is an ideal target for ovary tumors with elevated cyclin E1 expression. *Oncotarget* **6**, 20801-20812, doi:10.18632/oncotarget.4600 (2015).
171 McManus, K. J., Barrett, I. J., Nouhi, Y. & Hieter, P. Specific synthetic lethal killing of RAD54B-deficient human colorectal cancer cells by FEN1 silencing. *PNAS* **106**, 5, doi:doi-org.uml.idm.oclc.org/10.1073/pnas.0813414106 (2009).
172 Qiu, S., Adema, C. M. & Lane, T. A computational study of off-target effects of RNA interference. *Nucleic Acids Research* **33**, 1834-1847, doi:10.1093/nar/gki324 (2005).
173 Rees, M. G. *et al.* Systematic identification of biomarker-driven drug combinations to overcome resistance. *Nat Chem Biol* **18**, 615-624, doi:10.1038/s41589-022-00996-7 (2022).
174 Tadesse, S. *et al.* Targeting CDK2 in cancer: challenges and opportunities for therapy. *Drug Discov Today* **25**, 406-413, doi:10.1016/j.drudis.2019.12.001 (2020).
175 Zarin, D. A., Fain, K. M., Dobbins, H. D., Tse, T. & Williams, R. J. 10-Year Update on Study Results Submitted to ClinicalTrials.gov. *New England Journal of Medicine* **381**, 1966-1974, doi:10.1056/NEJMsr1907644 (2019).
176 Brown, V. *et al.* Abstract 2306: BLU-222, an investigational, potent, and selective CDK2 inhibitor, demonstrated robust antitumor activity in CCNE1-amplified ovarian cancer models. *Cancer Research* **82**, 2306-2306, doi:10.1158/1538-7445.Am2022-2306 (2022).
177 Aziz, K. *et al.* Ccne1 Overexpression Causes Chromosome Instability in Liver Cells and Liver Tumor Development in Mice. *Gastroenterology* **157**, 210-226 e212, doi:10.1053/j.gastro.2019.03.016 (2019).
178 McCann, K. E. & Hurvitz, S. A. Advances in the use of PARP inhibitor therapy for breast cancer. *Drugs Context* **7**, 212540, doi:10.7573/dic.212540 (2018).
179 McAndrew, E. N., Lepage, C. C. & McManus, K. J. The synthetic lethal killing of RAD54B-deficient colorectal cancer cells by PARP1 inhibition is enhanced with SOD1 inhibition. *Oncotarget* **7**, 14, doi:10.18632/oncotarget.13654 (2016).

180 Brenner, D. R. *et al.* Projected estimates of cancer in Canada in 2020. *CMAJ* **192**, E199-E205, doi:10.1503/cmaj.191292 (2020).
181 Oza, A. M. *et al.* Olaparib combined with chemotherapy for recurrent platinum-sensitive ovarian cancer: a randomised phase 2 trial. *Lancet Oncol* **16**, 87-97, doi:10.1016/s1470-2045(14)71135-0 (2015).
182 Matano, M. *et al.* Modeling colorectal cancer using CRISPR-Cas9-mediated engineering of human intestinal organoids. *Nat Med* **21**, 256-262, doi:10.1038/nm.3802 (2015).
183 Phan, N. *et al.* A simple high-throughput approach identifies actionable drug sensitivities in patient-derived tumor organoids. *Commun Biol* **2**, 78, doi:10.1038/s42003-019-0305-x (2019).
184 Dumont, S. *et al.* Organoids of epithelial ovarian cancer as an emerging preclinical in vitro tool: a review. *J Ovarian Res* **12**, 105, doi:10.1186/s13048-019-0577-2 (2019).
185 Sato, T. *et al.* Long-term expansion of epithelial organoids from human colon, adenoma, adenocarcinoma, and Barrett's epithelium. *Gastroenterology* **141**, 1762-1772, doi:10.1053/j.gastro.2011.07.050 (2011).
186 Fujii, M., Matano, M., Nanki, K. & Sato, T. Efficient genetic engineering of human intestinal organoids using electroporation. *Nat Protoc* **10**, 1474-1485, doi:10.1038/nprot.2015.088 (2015).
187 Ford, C. E., Werner, B., Hacker, N. F. & Warton, K. The untapped potential of ascites in ovarian cancer research and treatment. *British Journal of Cancer* **123**, 9-16, doi:10.1038/s41416-020-0875-x (2020).
188 Nanki, Y. *et al.* Patient-derived ovarian cancer organoids capture the genomic profiles of primary tumours applicable for drug sensitivity and resistance testing. *Scientific Reports* **10**, 12581, doi:10.1038/s41598-020-69488-9 (2020).
189 Zheng, L. *et al.* In vivo bioengineered ovarian tumors based on collagen, matrigel, alginate and agarose hydrogels: a comparative study. *Biomed Mater* **10**, 015016, doi:10.1088/1748-6041/10/1/015016 (2015).
190 Kopper, O. *et al.* An organoid platform for ovarian cancer captures intra- and interpatient heterogeneity. *Nature Medicine* **25**, 838-849, doi:10.1038/s41591-019-0422-6 (2019).
191 Myungjin Lee, J. *et al.* A three-dimensional microenvironment alters protein expression and chemosensitivity of epithelial ovarian cancer cells in vitro. *Laboratory Investigation* **93**, 528-542, doi:10.1038/labinvest.2013.41 (2013).

APPENDIX A: SOLUTIONS

CELL CULTURE

Table S1. 1 × DMEM/F12 Cell Culture Medium

Name	Amount
DMEM/F12 Powder (Gibco)	12.0 g
$NaHCO_3$	2.4 g
Milli-Q Water	Up to 1.0 L
Total Volume	1.0 L

- Titrate to pH 7.0
- Pass through 0.22 μm filter to sterilize

Table S2. Ultro Ser G Serum

Name	Amount
Ultro Ser G Powder (Pall Corp.)	1 vial
UltraPure Distilled Water (Gibco)	20.0 mL
Total Volume	20.0 mL

- Let stand 20 min at RT to dissolve powder; mix by pipetting

Table S3. 1 × DMEM/F12 Cell Culture Medium + 2% Ultro Ser G

Name	Amount
1 × DMEM/F12 Cell Culture Medium	980.0 mL
Ultro Ser G	20 mL
Total Volume	1.0 L

- Store at 4 °C

Table S4. Cupric Sulfate Pentahydrate

Name	Amount
Cupric Sulfate Pentahydrate	26.0 g
Milli-Q Water	Up to 1.0 L
Total Volume	1.0 L

Table S5. 10 × Phosphate-Buffered Saline (PBS; Stock Solution)

Name	Amount
NaCl	80.0 g
KCl	2.0 g
Na_2HPO_4	14.4 g
KH_2PO_4	2.4 g

Milli-Q Water	Up to 1.0 L
Total Volume	1.0 L

- Titrate to pH 7.

Table S6. 1 × PBS

Name	Amount
10 × PBS	100.0 mL
Milli-Q Water	900.0 mL
Total Volume	1.0 L

GENE SILENING

Table S7. 1 × siRNA Buffer

Name	Amount
5 × siRNA Buffer (Dharmacon)	100.0 µL
DEPC-treated Water	400.0 µL
Total Volume	500.0 µL

WESTERN BLOT

Table S8. Modified Radioimmunoprecipitation Assay (RIPA) Buffer

Name	Amount
50 mM Tris – pH 8.0	5.0 mL
150 mM NaCl	7.5 mL
SDS (0.1% [w/v])	500.0 µL
Sodium Deoxycholate (0.5% [w/v])	0.5 g
NP40 (1% [w/v])	1.0 mL
Milli-Q Water	Up to 100.0 mL
Total Volume	100.0 mL

- Protect from light and store at 4 °C

Table S9. 25 × Protease Inhibitor

Name	Amount
Protease Inhibitor Complete EDTA-free (Roche)	1 tablet
Milli-Q Water	2.0 mL
Total Volume	2.0 mL

- Vortex until dissolved
- Store at -20°C in 50 µL aliquots

Table S10. Protein Extraction Buffer

Name	Amount
Modified RIPA Buffer	960.0 µL
Milli-Q Water	40.0 µL
Total Volume	1.0 mL

Table S11. 4 × Tris-HCl/SDS, pH 6.8 (0.5M Tris-HCl Containing 0.4% SDS)

Name	Amount
Modified RIPA Buffer	960.0 µL
Milli-Q Water	40.0 µL
Total Volume	1.0 mL

- Titrate to pH 6.8 with 1N HCl
- Store at 4 °C

Table S12. 6 × SDS Sample Loading Buffer

Name	Amount
4 × Tris-HCl/SDS	6.5 mL
Glycerol	3.0 mL
SDS	1.0 g
β-mercaptoethanol	600.0 µL
Bromophenol Blue	1.2 mg
Total Volume	~10.0 mL

- Store 0.5 mL aliquots at -20 °C; warm to RT before use

Table S13. 10 × Running Buffer

Name	Amount
Tris Base	30.0 g
Glycerol	144.0 g
SDS	10.0 g
Milli-Q Water	Up to 1.0 L
Total Volume	1.0 L

Table S14. 1 × Running Buffer

Name	Amount
10 × Running Buffer	100.0 mL
Milli-Q Water	900.0 mL
Total Volume	1.0 L

Table S15. 1 × Transfer Buffer

Name	Amount
10 × Running Buffer	50.0 mL
Milli-Q Water	350.0 mL
Methanol	100.0 mL
Total Volume	500.0 mL

Table S16. Copper Phthalocyanine 3,4',4'',4'''-tetrasulfonic acid Tetrasodium Salt (CPTS)

Name	Amount
CPTS	50.0 mg
HCl	1.0 mL
Milli-Q Water	Up to 1.0 L
Total Volume	1.0 L

Table S17. 10 × Tris Buffered Saline (TBS)

Name	Amount
NaCl	80.0 g
KCl	2.0 g
1 M Tris – pH 7.5	250.0 mL
Milli-Q Water	Up to 1.0 L
Total Volume	1.0 L

Table S18. 1 × TBS-Tween20 (TBST)

Name	Amount
10 × TBS	100.0 mL
Tween-20	1.0 mL
Milli-Q Water	Up to 1.0 L
Total Volume	1.0 L

Table S19. Non-fat Milk Blocking Solution (5% [w/v])

Name	Amount
Non-fat Milk Powder (Carnation)	5.0 g
TBST	Up to 100.0 L
Total Volume	1.0 L

SL ASSAYS

Table S20. Paraformaldehyde Fixative (4% [w/v])

Name	Amount
Paraformaldehyde (VWR)	0.4 g
1 × PBS	10.0 mL
Total Volume	10.0 mL

Table S21. Hoechst 33342 (Stock Dilution – 1 mg/mL)

Name	Amount
Hoechst 33342 (ThermoFisher Scientific)	10.0 mg
1 × PBS	Up to 10.0 mL
Total Volume	10.0 mL

- Store at - 20°C, protected from light

Table S22. Hoechst 33342 (Stock Dilution – 300 ng/mL)

Name	Amount
10 N HCl	2.0 mL
Milli-Q Water	8.0 mL
Total Volume	1.0 L

- Store at - 20°C, protected from light

FLUORESCENT LABELING

Table S23. 1 × PBS + 0.5% Triton X-100

Name	Amount
Triton X-100	5.0 mL
1 × PBS	995.0 mL
Total Volume	1.0 L

Table S24. 1 × PBS + 0.1% Triton X-100

Name	Amount
Triton X-100	1.0 mL
1 × PBS	999.0 mL
Total Volume	1.0 L

Table S25. DAPI Stock Solution (50 µg/mL)

Name	Amount
DAPI (stock 5 mg/mL, Sigma-Aldrich)	10.0 µL
Milli-Q Water	990 µL
Total Volume	1.0 mL

- Store at - 20°C, protected from light

Table S26. DAPI Mounting Medium (0.5 µg/mL)

Name	Amount
DAPI (50 µg/mL stock solution)	10.0 µL
Vectashield mounting medium (Vector laboratories)	990 µL
Total Volume	1.0 mL

- Store at - 20°C, protected from light

APPENDIX B: SUPPORTING DATA TABLES

Table S27. SynLethDB Identifies Putative SL Interactors of *SKP1*

Gene Name[A]				
PLC1	*CDC53*	*SMC2*	*MUS81*	*HSP82*
MAD2	*MET22*	*HSC82*	*SLC22A1*	*SLC22A2*

[A]Published SL interactors of *SKP1* identified in SynLethDB[133].

Table S28. SynLethDB Identifies Putative SL Interactors of *CUL1*

Gene Name[A]				
CSK	*NAE1*	*RAB23*	*BRCA1*	*DCTN4*
TBL1XR1	*TAB2*			

[A]Published SL interactors of *CUL1* identified in SynLethDB[133].

Table S29. SynLethDB Identifies Putative SL Interactors of *RBX1*

Gene Name[A]				
ATM	*RAD23B*	*POLD4*	*IGF1*	*PARP2*
BRCA1	*NHP2*	*POLD1*	*EGFR*	*POLE*
CDK4	*IGHMBP2*	*MAPK12*	***CDK2***	*MT1X*
H4C1	***PARP1***	*GTF2H1*	*PPM1D*	*CDK6*
IGFBP3	*MTOR*	*POLM*	*RAD9A*	*CETN2*
MDM2	*H2AC8*	*POLR2A*	*RAD51*	*XRCC2*
PMS2	*DNTT*	*KDR*	*ERCC1*	*BID*
UNG	*SESN2*	*WRAP53*	*RELA*	*SSBP1*
USP1	*RPL13A*	*ZBTB32*	*RRM1*	*TNFRSF10B*

[A]Published SL interactors of *RBX1* identified in SynLethDB[133].

Table S30. BioGRID Identifies Putative SL Interactors of *SKP1* in *S. cerevisiae*

Gene Name[A]					
TTI2	*ARP8*	*YDR115W*	*HSP82*	*ULA1*	*MAD2*
ASA1	*HOM6*	*MTC2*	*RRI1*	*CDC53*	*MET22*
AAH1	*AFT1*	*GCN5*	*CDC55*	*PLC1*	*SMC2*
APQ12	*VID22*				

[A]Published SL interactors of *SKP1* (*i.e.*, *SKP1*) in *S. cerevisiae*, identified in BioGRID[129].

Table S31. BioGRID Identifies Putative SL Interactors of *CUL1* in *S. cerevisiae*

Gene Name[A]					
RPS19A	*CDC12*	***CDC28***	*NOG1*	*PSP2*	*YDR090C*
UAF30	*DNA2*	*NOP9*	*SEC62*	*YOX1*	*GRX3*
RAD50	*ERG9*	*CDC11*	*TIF6*	*AIM32*	*MTC5*
APM1	*PRI2*	*MAK11*	*PRE2*	*ATP18*	*YDR134C*
TMA46	*RPT1*	*ASK1*	*RRP15*	*PEX12*	*RAV2*
YAP1802	*RSC4*	*YJU2*	*LTE1*	*RIM9*	*PEX10*
CLA4	*GPI13*	*ABF1*	*YAR029W*	*RIM13*	*PMP3*
PET127	*BET5*	*RPC25*	*MUM2*	*UBP8*	*PEX3*
DCS1	*VTI1*	*EBP2*	*YBR238C*	*ZDS1*	*SEM1*
YNL067W-B	*ARC35*	*SDS22*	*SGF29*	*YMR279C*	*XRS2*
ISA1	*RFC4*	*LAS1*	*PEX5*	*YNL010W*	*RPS18A*
MTC2	*PFY1*	*RPF2*	*YPS7*	*HDA1*	*NHX1*
RPL40A	*NAB3*	*DRS1*	*PUF6*	*PMS1*	*TOM1*
SLM2	*TPI1*	*COF1*	*RAD51*	*MKT1*	*RPL27B*
RFC5	*CDC37*	*NOC3*	*CGR1*	*NST1*	*YEF1*
IPP1	*CAB5*	*RPL15A*	*YBP2*	*LRO1*	*YER053C-A*
YLR156W	*SPC19*	*RSC58*	*MRM2*	*NRM1*	*TRP2*
PEX2	*MSS4*	*CDC45*	*HXK2*	*PEX15*	*PRS2*
PKC1	*RRP45*	*SEC10*	*YGR054W*	*YOR012W*	*CHD1*
MAK16	*GPI11*	*NMT1*	*PEX4*	*WHI2*	*IES1*
SER1	*ESF1*	*PWP1*	*PRE9*	*VHS3*	*YFL052W*
YNR075C-A	*SNM1*	*NOP56*	*RTT102*	*RIM20*	*GCN20*
PAU12	*WBP1*	*DBP9*	*RPS27B*	*BUD7*	*UBP6*
NAS2	*MMS21*	*YHC1*	*UBA4*	*SGF11*	*RPL29*
VPS15	*SNU13*	*CWC24*	*MTC6*	*LCL1*	*YFR032C-B*
IRC25	*NTF2*	*RPP0*	*RPN10*	*SUR1*	*RIM8*
RPL9B	*PRE1*	*SEC39*	*RPL16A*	*MUK1*	*MMS2*
PKR1	*UTP7*	*RSC9*	*TMA108*	*RPL21B*	*RPL9A*
YHR218W	*PUP3*	*ERO1*	*PRY3*	*NIP100*	*VAM7*
SER2	*RSP5*	*NUP116*	*RAV1*	*SRO7*	*EDC1*
UBR2	*ACT1*	*ROT1*	*APS2*	*YPR172W*	*SIC1*
IES2	*YPI1*	*HAS1*	*YJR084W*	*VPS4*	*SAC7*
ERG3	*RPN11*	*NOP2*	*SSH4*	*HDA3*	*LAG2*
ISY1	*PRE4*	*POL1*	*CMC1*	*PEX22*	*YPK9*
CMD1	*SCL1*	*RPC31*	*PEX1*	*SLA1*	*RRI1*
CDC39	*RPT6*	*RIA1*	*SAC1*	*YBL086C*	*CDC55*
CDC24	*SRM1*	*RPC34*	*DOA1*	*RPL19A*	*ULA1*
EXO84	*UFD1*	*DBP6*	*YRA2*	*NHP6B*	*GLE2*
MAK5	*UTP8*	*PRE6*	*VPS51*	*CYC8*	*CDC4*
CCT8	*CBF2*	*BRX1*	*DBP7*	*HSL7*	*SKP1*
UTP5	*SDA1*	*NOP8*	*ESL2*	*UMP1*	*SGT1*
CAK1	*PUP2*	*NOB1*	*SMF3*	*RPS6B*	*DCN1*

RSC8	*RPN1*	*RPT5*	*SRN2*	*SLX1*	*BCK1*
RPN12	*BRL1*	*PUP1*	*RPL37A*	*APM3*	*SLT2*
SLD3	*QNS1*	*RPT4*	*ERF2*	*PHO89*	*HRT1*
DAM1	*RPF1*	*RPN8*	*MCP2*	*YCL001W-A*	*DBP10*
ZPR1	*RIX1*	*PRE10*	*IKI3*	*POF1*	*CDC34*
CRM1	*CYR1*	*NOP4*	*RPL6B*	*PAT1*	

[A]Published SL interactors of *CDC53* (*i.e.*, *CUL1*) in *S. cerevisiae*, identified in BioGRID[129].

Table S32. BioGRID Identifies Putative SL Interactors of *RBX1* in *S. cerevisiae*

Gene Name[A]					
ARP8	*CDC12*	*CDC34*	*CDC53*	*SEC15*	*MAD1*
RTT107	*CDC42*	*GRR1*	*ARP2*	*SEC18*	*MRE11*
ACT1	*SGS1*				

[A]Published SL interactors of *HRT1* (*i.e.*, *RBX1*) in *S. cerevisiae*, identified in BioGRID[129].

Table S33. List of Genes Contained within the siRNA DDR Library

Gene Name[A]					
RAD50	*POLE2*	*RUVBL2*	*PRKCG*	*FANCC*	*FEN1*
RAD18	*TDP2*	*GTF2H5*	*POLE*	*UBE2B*	*MDC1*
DDX11	*APEX1*	*TDG*	*TOPBP1*	*RAD54L*	*RPA1*
PMS1	*BRCA1*	*POLM*	*REV3L*	*HMGB2*	*GADD45A*
SMC3	*RAD52*	*FANCL*	*FANCD2*	*TRIP13*	*TYMS*
MAD2L2	*FANCM*	*SETMAR*	*PRKDC*	*RASSF7*	*PARP2*
PARP3	*NEIL2*	*REV1*	*SOD1*	*CSNK1D*	*MSH3*
HELQ	*RAD51D*	*CCNO*	*GTF2H2*	*YBX1*	*XRCC1*
TCEA1	*RTEL1*	*KAT2A*	*APTX*	*FAM175A*	*TRIM28*
IP6K3	*SIRT1*	*TREX1*	*WRN*	*CHEK2*	*NUDT1*
ATF2	*VCP*	*ALKBH2*	*GTF2H4*	*CETN2*	*ATP23*
IGHMBP2	*PMS2*	*CSNK1E*	*BRIP1*	*DCLRE1B*	*ERCC3*
XPC	*HUS1*	*RPS27L*	*DNA2*	*POLK*	*SHFM1*
POLI	*RAD17*	*TOP2A*	*PER1*	*POLN*	*HINFP*
MSH4	*XAB2*	*FANCG*	*ATR*	*RBBP8*	*XRCC2*
GTF2H1	*ERCC5*	*MUS81*	*UIMC1*	*HMGB1*	*RAD54B*
PAPD7	*BRCC3*	*POLG2*	*DCLRE1A*	*UVRAG*	*TREX2*
MBD4	*RNF168*	*PRPF19*	*MTOR*	*RAD23B*	*ATXN3*
TP73	*OGG1*	*LIG3*	*MEN1*	*MLH1*	*MRE11A*
SLX1A	*MUTYH*	*TDP1*	*POLH*	*GADD45G*	*EYA3*

NEIL3	*UBE2A*	*PRMT6*	*RNF8*	*TP53*	*RPA2*
MSH6	*FANCE*	*EME2*	*APLF*	*TP53BP1*	*MNAT1*
RECQL5	*NEIL1*	*NHEJ1*	*XRCC4*	*DLGAP5*	*EXO1*
ERCC6	*LIG*	*RPA3*	*CHAF1A*	*SPO11*	*DNMT1*
KAT5	*RECQL*	*RECQL4*	*RDM1*	*MLH3*	*CIB1*
DCLRE1C	*FANCB*	*PALB2*	*FAN1*	*CNOT7*	*CDKN2D*
RRM2B	*GEN1*	*RAD9A*	*UPF1*	*NBN*	*DMC1*
XPA	*RAD23A*	*POLD1*	*MGMT*	*FANCF*	*PARG*
MMS19	*NABP2*	*EME1*	*POLQ*	*RAD51C*	*MSH5*
SMC6	*CCNH*	*SETX*	*FANCI*	*UBE2V2*	*SMUG1*
ABL1	*MPLKIP*	*PNKP*	*BLM*	*APEX2*	*BRCA2*
USP1	*EYA1*	*XRCC3*	*NPM1*	*ASF1A*	*H2AFX*
BTG2	*MPG*	*TNP1*	*MSH2*	*RAD51*	*RAD1*
DDB1	*ERCC8*	*PARP1*	*FAAP24*	*RPAIN*	*POLA1*
PCNA	*BAZ1B*	*ALKBH1*	*POLB*	*NTHL1*	*DDB2*
ERCC2	*TADA3*	*ATRX*	*UBE2V1*	*POLL*	*GTF2H3*
ALKBH3	*LIG4*	*ATM*	*SMC1A*	*CDK7*	*FANCA*
RAD21	*RAD51B*	*UNG*	*CHEK1*	*ATRIP*	*DUT*
XRCC6	*CLK2*	*POLG*	*BRE*	*XRCC5*	*RPA4*
NABP1	*UBE2N*	*ERCC4*	*ERCC1*	*RRM2*	

Table S34. RNAi-based Screen of the DDR Identifies Putative SL interactors of *CUL1*

Gene Name[A]	SL Ratio[B]	Gene Name[A]	SL Ratio[B]	Gene Name[A]	SL Ratio[B]
RAD23B	5.182953	*MSH6*	3.587243	*EME2*	3.232183
POLH	4.045353	*TDP1*	3.507496	*TP73*	3.196667
TRIP13	3.927521	*FANCE*	3.322406	*MNAT1*	3.1427
DCLRE1C	3.745805	*MUTYH*	3.268464	*TREX2*	3.077734
TP53BP1	3.682847	*ERCC3*	3.263614	*ATP23*	2.96509
XRCC4	3.612315	*RAD17*	3.234136	*LIG3*	2.946603
APLF	2.933293	*RNF8*	2.651743	*RAD52*	2.514826
XRCC2	2.926788	*NUDT1*	2.634104	*POLG2*	2.464896
DMC1	2.833758	*UBE2A*	2.628193	*NEIL3*	2.383372
XPC	2.820606	*SLX1A*	2.580936	*EYA3*	2.332293
KAT5	2.819763	*SMC6*	2.571875	*REV3L*	2.321855

GADD45G	2.661965	*OGG1*	2.549705	*RECQL5*	2.308198
SHFM1	2.30203	*PRMT6*	2.09498	*BRCC3*	1.990566
TP53	2.237539	*NBN*	2.074166	*PKRDC*	1.973977
MLH1	2.220101	*ATRX*	2.068102	*NHEJ1*	1.971138
POLN	2.204369	*ABL1*	2.034884	*DUT*	1.920528
CHEK2	2.172637	*NEIL1*	2.030602	*DCLRE1B*	1.897793
MRE11A	2.113911	*FAM175A*	2.118004	*CHAF1A*	1.888234
FANCD2	1.886294	*POLM*	1.798075	*CLK2*	1.713701
RNF168	1.882937	*CCNH*	1.782763	*TADA3*	1.704754
MBD4	1.870413	*FANCA*	1.763908	*PARG*	1.646132
ATR*	1.842439	*POLL*	1.76125	*DCLRE1A*	1.631529
POLQ	1.836854	*EXO1*	1.73128	*PER1*	1.563788
UVRAG	1.804482	*POLI*	1.728441	*TYMS*	1.562881
POLB	1.560497	*ATM*	1.497811	*GTF2H3*	1.403707
DLGAP5	1.554267	*ATXN3*	1.488246	*GADD45A*	1.401766
RRM2B	1.548579	*LIG4*	1.479863	*ALKBH3*	1.390931
RAD23A	1.52553	*HMGB2*	1.433908	*UPF1*	1.372852
NABP2	1.509322	*RAD51B*	1.422784	*PARP1*	1.372398
MEN1	1.498635	*RBBP8*	1.421438	*RAD21*	1.352003
MSH5	1.349373	*PALB2*	1.298516	*FANCM*	1.286312
RAD51C	1.322076	*XPA*	1.291148	*FANCL*	1.258379
DDB2	1.318337	*NEIL2*	1.290834	*FANCF*	1.251328

[A]DDR genes identified as putative SL interactors of *CUL1*.
[B]SL ratio for each DDR gene, where SL ratios > 1.25 are considered a putative SL interactor.

Table S35. RNAi-based Screen of the DDR Identifies Putative SL interactors of *SKP1*

Gene Name[A]	SL Ratio[B]	Gene Name[A]	SL Ratio[B]	Gene Name[A]	SL Ratio[B]
XRCC5	32.07166124	*ALKBH1*	7.534201954	*MDC1*	4.454442328
ATRIP	18.93811075	*RUVBL2*	5.369144885	*KAT2A*	4.421580588
CLK2	16.00651466	*GEN1*	5.231771878	*PRKCG*	4.290409779

POLE2	8.658397723	*BRE*	4.680781759	*RPS27L*	4.215801837
RAD54L	8.566653111	*VCP*	4.597656106	*CETN2*	3.966549621
POLA1	7.702554745	*SETMAR*	4.570847615	*DDB2*	3.934638354
RDM1	3.877035831	*GADD45G*	3.59258301	*GTF2H4*	2.815219452
IP6K3	3.870475803	*SLX1A*	3.381142546	*DNA2*	2.794577685
UBE2V1	3.737785016	*RAD51B*	3.377198697	*POLD1*	2.697068404
ALKBH2	3.728674588	*BAZ1B*	3.2247557	*UNG*	2.661889251
CDK7	3.64495114	*UBE2B*	3.165189101	*FANCC*	2.644210771
ATRX	3.641693811	*NUDT1*	2.863426354	*MGMT*	2.638436482
NTHL1	2.613308516	*TNP1*	2.362028851	*CHEK2*	2.171899158
ATM	2.460369164	*FANCD2*	2.328721647	*BTG2*	2.162052117
FEN1	2.455210914	*POLM*	2.250610004	*FANCG*	2.159590783
DCLRE1A	2.435431094	*RAD23A*	2.234264859	*LIG*	2.156897867
SIRT1	2.411367862	*PALB2*	2.228013029	*RNF8*	2.128010842
TP53	2.409659336	*WRN*	2.20984268	*MBD4*	2.120187273
GTF2H5	2.110672166	*MPG*	1.985667752	*RAD9A*	1.916530945
CCNH	2.079030576	*ALKBH3*	1.964169381	*RAD51*	1.905537459
XRCC1	2.076689025	*NBN*	1.954397394	*FANCF*	1.899674267
FAM175A	2.064473977	*RPA2*	1.953284462	*EXO1*	1.899562619
RAD50	2.036730378	*XPC*	1.94282707	*NEIL3*	1.876753906
MSH3	1.986634464	*NEIL2*	1.91764483	*RECQL*	1.837684344
MSH5	1.829933139	*EME2*	1.710933666	*MSH4*	1.662871086
HMGB1	1.775298261	*TOPBP1*	1.704573182	*DUT*	1.645924063
FANCB	1.759086846	*SHFM1*	1.690313858	*MMS19*	1.638892882
TDG	1.758616189	*XAB2*	1.685807239	*XRCC2*	1.63199655
TRIP13	1.745142069	*XRCC6*	1.685667752	*PARG*	1.629129828
KAT5	1.723906481	*FAAP24*	1.682285142	*NABP2*	1.628091017
CNOT7	1.611205212	*FANCL*	1.503350686	*APEX1*	1.412867019
ERCC2	1.606514658	*FANCA*	1.503290065	*RPA4*	1.394601749
RAD51C	1.586510826	*YBX1*	1.500250002	*POLB*	1.376125695

RTEL1	1.581803649	*DLGAP5*	1.497703283	*RPAIN*	1.359194551
RAD18	1.565566195	*PARP2*	1.493867854	*RAD17*	1.354275574
MLH3	1.503736348	*HELQ*	1.465487847	*RPA1*	1.342027573
TREX1	1.336936281	*ERCC5*	1.318640791	*CSNK1D*	1.279477549
FANCE	1.333408328	*XPA*	1.316507284	*RNF168*	1.272232726
DDX11	1.326307972	*RECQL4*	1.299674267	*SMUG1*	1.252871593
EYA3	1.325889108	*GTF2H1*	1.288379072		

[A]DDR genes identified as putative SL interactors of *SKP1*.
[B]SL ratio for DDR each gene, where SL ratios > 1.25 are considered a putative SL interactor.

Table S36. RNAi-based Screen of the DDR Identifies Putative SL interactors of *RBX1*

Gene Name[A]	SL Ratio[B]	Gene Name[A]	SL Ratio[B]	Gene Name[A]	SL Ratio[B]
BAZ1B	5.97406665	*RPA2*	2.72806166	*FANCE*	2.59594653
GADD45G	4.89521345	*EME2*	2.71756335	*DCLRE1A*	2.42833423
CETN2	3.44704614	*CHEK2*	2.69634725	*DUT*	2.39766615
XPC	3.05912487	*HMGB1*	2.68960174	*NEIL2*	2.39092347
RAD54L	3.0034946	*RNF168*	2.64938076	*UBE2B*	2.33834892
RAD23A	2.98166208	*KAT2A*	2.62712744	*FEN1*	2.32775857
POLA1	2.28010949	*TREX2*	2.03967227	*GTF2H3*	1.89578264
POLH	2.26092486	*TOPBP1*	2.01113069	*USP1*	1.87543892
MDC1	2.20677942	*LIG4*	1.97775002	*MBD4*	1.84250395
RPAIN	2.18889538	*ATRIP*	1.91635644	*MSH3*	1.81170115
PRPF19	2.12646684	*PARG*	1.91389642	*DMC1*	1.80428882
PRKCG	2.06677177	*MSH4*	1.90508962	*WRN*	1.77958951
MEN1	1.76771597	*TP73*	1.60454219	*DDB2*	1.5402457
FANCD2	1.71872101	*NTHL1*	1.59334633	*IP6K3*	1.53967373
GTF2H4	1.66672196	*NEIL3*	1.58720349	*POLM*	1.50989745
DLGAP5	1.66617384	*XAB2*	1.58508632	*TP53*	1.50832908
DCLRE1B	1.65056556	*PRKDC*	1.56334376	*TCEA1*	1.48492977
MMS19	1.63985592	*SLX1A*	1.55716915	*LIG3*	1.47458274

TADA3	1.40973348	*POLL*	1.34336551	*RAD17*	1.29476353
RAD51C	1.38495517	*PARP3*	1.33916663	*RPA4*	1.2741296
FANCA	1.38493858	*POLK*	1.33842957	*TRIP13*	1.27084181
RTEL1	1.38188624	*RNF8*	1.33149806	*HELQ*	1.26108174
ATR	1.37948439	*POLQ*	1.32064696	*SETMAR*	1.3132032
APEX1	1.34475334				

[A]DDR genes identified as putative SL interactors of *RBX1*.
[B]SL ratio for each DDR gene, where SL ratios > 1.25 are considered a putative SL interactor.

Table S37. Direct SL Tests Identify *CHEK2* as a Putative SL Interactor of *RBX1*

Cell Line	Silencing Condition	N[A]	p-value[B]	Significance[C]
NT-Control	siControl	6	NA	NA
	siCHEK2-1		NA	NA
	siCHEK2-2		NA	NA
	siCHEK2-Pool		NA	NA
RBX1$^{+/-}$-1	siControl	6	NA	NA
	siCHEK2-1		0.2039	ns
	siCHEK2-2		0.1945	ns
	siCHEK2-Pool		0.0046	**
RBX1$^{+/-}$-2	siControl	6	NA	NA
	siCHEK2-1		0.4874	ns
	siCHEK2-2		0.2796	ns
	siCHEK2-Pool		0.0376	*

[A]6 Techical replicates (n) per biological replicate (N).
[B]p-values calculated from paired *t* tests comparing the mean number of NT-Control and *RBX1*$^{+/-}$ clones following *CHEK2* silencing.
[C]Significance level (ns = not significant; * p-value < 0.05; ** p-value < 0.01).

Table S38. Direct SL Tests Identify *PARG* as a Putative SL Interactor of *RBX1*

Cell Line	Silencing Condition	N[A]	p-value[B]	Significance[C]
NT-Control	siControl	6	NA	NA
	siPARG-2		NA	NA
	siPARG-3		NA	NA
	siPARG-Pool		NA	NA
RBX1$^{+/-}$-1	siControl	6	NA	NA
	siPARG-2		0.0164	*
	siPARG-3		0.0362	*
	siPARG-Pool		0.0001	***
RBX1$^{+/-}$-2	siControl	6	NA	NA
	siPARG-2		0.3603	ns
	siPARG-3		0.8955	ns
	siPARG-Pool		0.0014	**

[A]6 Techical replicates (n) per biological replicate (N).
[B]p-values calculated from paired *t* tests comparing the mean number of NT-Control and *RBX1*$^{+/-}$ clones following *PARG* silencing.
[C]Significance level (ns = not significant; * p-value < 0.05; ** p-value < 0.01; *** p-value < 0.001).

Table S39. Direct SL Tests Identify *PARP1* as a Putative SL Interactor of *RBX1*

Cell Line	Silencing Condition	N[A]	p-value[B]	Significance[C]
NT-Control	siControl	6	NA	NA
	siPARP1-1		NA	NA
	siPARP1-2		NA	NA
	siPARP1-Pool		NA	NA
RBX1$^{+/-}$-1	siControl	6	NA	NA
	siPARP1-1		0.3383	ns
	siPARP1-2		0.0403	*
	siPARP1-Pool		0.0534	ns
RBX1$^{+/-}$-2	siControl	6	NA	NA
	siPARP1-1		0.2958	ns
	siPARP1-2		0.0761	ns
	siPARP1-Pool		0.1454	ns

[A]6 Techical replicates (n) per biological replicate (N).
[B]p-values calculated from paired *t* tests comparing the mean number of NT-Control and *RBX1*$^{+/-}$ clones following *PARP1* silencing.
[C]Significance level (ns = not significant; * p-value < 0.05).

Table S40. Olaparib Induces Decreases in the Number *RBX1*$^{+/-}$ Clones

Cell Line	Condition	N[A]	p-value[B]	Significance[C]
NT-Control	DMSO	3	NA	NA
	Olaparib		NA	NA
RBX1$^{+/-}$-1	DMSO	3	NA	NA
	Olaparib		0.0647	ns
RBX1$^{+/-}$-2	DMSO	3	NA	NA
	Olaparib		0.0302	*

[A]6 Techical replicates (n) per biological replicate (N).
[B]p-values calculated from paired *t* tests comparing the mean number of NT-Control and *RBX1*$^{+/-}$ clones following treatment with Olaparib.
[C]Significance level (ns = not significant; * p-value < 0.05).

Table S41. Olaparib Induces Increases in γ-H2AX in *RBX1*$^{+/-}$ Clones

Cell Line	Condition	N[A]	p-value[B]	Significance[C]
NT-Control	DMSO	1	NA	NA
	Olaparib		<0.0001	****
RBX1$^{+/-}$-1	DMSO	1	NA	NA
	Olaparib		<0.0001	****
RBX1$^{+/-}$-2	DMSO	1	NA	NA
	Olaparib		0.0003	***

[A]≥100 nuclei analyzed per condition (n) per biological replicate (N).
[B]p-values calculated from KS tests comparing the distribution of γ-H2AX foci within NT-Control and *RBX1*$^{+/-}$ clones following treatment with DMSO and Olaparib.
[C]Significance level (ns = not significant; *** p-value < 0.001; **** p-value < 0.0001).

Table S42. SNS-032 Induces Decreases in the Number *RBX1*$^{+/-}$ Clones

Cell Line	Condition	N[A]	p-value[B]	Significance[C]
NT-Control	DMSO	3	NA	NA
	SNS-032		NA	NA
RBX1$^{+/-}$-1	DMSO	3	NA	NA
	SNS-032		0.0069	**
RBX1$^{+/-}$-2	DMSO	3	NA	NA
	SNS-032		0.0063	**

[A]6 Techical replicates (n) per biological replicate (N).
[B]p-values calculated from paired *t* tests comparing the mean number of NT-Control and *RBX1*$^{+/-}$ clones following treatment with SNS-032.
[C]Significance level (ns = not significant; ** p-value < 0.01).

Table S43. SNS-032 Induces Increases in γ-H2AX in *RBX1*$^{+/-}$ Clones

Cell Line	Condition	N[A]	p-value[B]	Significance[C]
NT-Control	DMSO	1	NA	NA
	Olaparib		0.09577	ns
RBX1$^{+/-}$-1	DMSO	1	NA	NA
	Olaparib		<0.0001	****
RBX1$^{+/-}$-2	DMSO	1	NA	NA
	Olaparib		<0.0001	****

[A]≥100 nuclei analyzed per condition (n) per biological replicate (N).
[B]p-values calculated from KS tests comparing the distribution of γ-H2AX foci within NT-Control and *RBX1*$^{+/-}$ clones following treatment with DMSO and SNS-032.
[C]Significance level (ns = not significant; **** p-value < 0.0001).